

UC Santa Barbara

UC Santa Barbara Electronic Theses and Dissertations

Title

Structural Underpinnings of Magnetic and Electronic Behavior in Transition Metal Oxides and Chalcogenides

Permalink

<https://escholarship.org/uc/item/1sm1s9q1>

Author

Schueller, Emily

Publication Date

2020

Peer reviewed|Thesis/dissertation

University of California
Santa Barbara

Structural Underpinnings of Magnetic and Electronic Behavior in Transition Metal Oxides and Chalcogenides

A dissertation submitted in partial satisfaction
of the requirements for the degree

Doctor of Philosophy

in

Materials

by

Emily Christine Schueller

Committee in charge:

Professor Ram Seshadri, Chair
Professor Stephen D. Wilson
Professor Michael Chabinyc
Professor Ania C. Bleszynski Jayich

September 2020

The Dissertation of Emily Christine Schueller is approved.

Professor Stephen D. Wilson

Professor Michael Chabinyc

Professor Ania C. Bleszynski Jayich

Professor Ram Seshadri, Committee Chair

July 2020

Structural Underpinnings of Magnetic and Electronic Behavior in Transition Metal
Oxides and Chalcogenides

Copyright © 2020

by

Emily Christine Schueller

To my family

Acknowledgements

I would like to thank my advisor, Ram Seshadri, for his advice, ideas, and support. I would also like to thank the rest of my committee, especially Stephen Wilson, for their open doors and wisdom. I am grateful to the support staff of the MRL and CNSI, especially Amanda Strom for keeping the facilities running and Fuzzy Rogers for help with the computing cluster.

I would like to thank the entire Seshadri group for their laughs, advice, and moral support. In particular, Emily Levin for being a mentor, friend, and roommate, and Leo Lamontagne and Joya Cooley for being the best officemates (and Molleigh Preefer as an honorary office mate)! Geneva Laurita and Doug Fabini were wonderful sources of advice on perovskites and PDF analysis. My collaborators on the DMREF: James Rondinelli, who gave advice on all things group theory, and Kyle Miller and Julia Zuo, who have helped me constantly with both science and life. I especially need to thank Joshua Bocarsly and Daniil Kitchaev, who taught me everything I know about magnetism, DFT, and writing good abstracts. Transitioning to a new research area can be hard, but they were patient and understanding (and responded to slack messages at all hours).

I would like to thank my roommates and friends, particularly Kan Tagami and Akhil Mauze for being neverending sources of entertainment and venting sessions. I am grateful for all of the volunteers at BUNS, and my amazing bunny-sitters Jackie and Lee, who made it possible for me to travel to conferences and beamtimes without worry. Finally, I cannot express enough my love and gratitude for my family, Albert, Laura, and Rachel, who have acted as my biggest cheerleaders and have been my rock during this entire process.

Curriculum Vitæ

Emily Christine Schueller

Education

Sep 2016 – Jul 2020 Ph.D. in Materials (expected)
University of California, Santa Barbara
Advisor: Professor Ram Seshadri

Aug 2012 – May 2016 B.S. in Chemical Engineering
University of Southern California

Publications

13. Schueller, E. C., Miller, K. D., Zhang, W., Zuo, J. L., Rondinelli, J. M., Wilson, S. D., and Seshadri, R. "Structural Signatures of the Insulator-to-Metal Transition in $\text{BaCo}_{1-x}\text{Ni}_x\text{S}_2$," *Submitted*.
12. Schueller, E. C., Kitchaev, D. A., Zuo, J. L., Bocarsly, J. D., Cooley, J. A., Van der Ven, A., Wilson, S. D., and Seshadri, R. (2020) "Structural Evolution and Skyrmionic Phase Diagram of the Lacunar Spinel GaMo_4Se_8 ," *Phys. Rev. Materials*, 4: 064402 *Editors' suggestion*
11. Sengupta, D., Sandoval-Pauker, C., Schueller, E. C., Encerrado-Manriquez, A., Metta-Magana, A., Lee, W-Y., Seshadri, R., and Fortier, S. (2020) "Isolation of a Bimetallic Cobalt(III) Nitride and Examination of Its Hydrogen Atom Abstraction Chemistry and Reactivity Towards H_2 ," *J. Am. Chem. Soc.*, 142 (18): 8233–8242
10. Cooley, J. A., Bocarsly, J. D., Schueller, E. C., Levin, E. E., Rodriguez, E. E., Huq, A., Lapidus, S. H., Wilson, S. D., and Seshadri, R. (2020) "Evolution of Noncollinear Magnetism in Magnetocaloric MnPtGa ," *Phys. Rev. Materials*, 4: 044405.
9. Kitchaev, D. A., Schueller, E. C., and Van der Ven, A. (2020) "Mapping Skyrmion Stability in Uniaxial Lacunar Spinel Magnets from First-Principles," *Phys. Rev. B*, 101: 054409. *Editors' suggestion*
8. Schueller, E. C., Zuo, J. L., Bocarsly, J. D., Kitchaev, D. A., Wilson, S. D., and Seshadri, R. (2019) "Modeling the Structural Distortion and Magnetic Ground State of the Polar Lacunar Spinel GaV_4Se_8 ," *Phys. Rev. B*, 100: 045131.
7. Spanopoulos, I., Ke, W., Stoumpos, C. C., Schueller, E. C., Kontsevoi, O. Y., Seshadri, R., and Kanatzidis, M. G. (2018) "Unraveling the Chemical Nature of the 3D "Hollow" Hybrid Halide Perovskites," *J. Am. Chem. Soc.*, 140 (17): 5728–5742.
6. Schueller, E. C., Laurita, G., Fabini, D. H., Stoumpos, C. C., Kanatzidis, M. G., and Seshadri, R. (2018) "Crystal Structure Evolution and Notable Thermal Expansion in Hybrid Perovskites Formamidinium Tin Iodide and Formamidinium Lead Bromide," *Inorg. Chem.*, 57 (2): 695–701.

5. Hundley, J. M., Eckel, Z. C., Schueller, E. C., Cante, K., Biesboer, S. M., Yahata, B. D., Schaedler, T. A. (2017) "Geometric Characterization of Additively Manufactured Polymer Derived Ceramics," *Addit. Manuf.*, 18: 95–102.
4. Evans, H. A., Schueller, E. C., Smock, S. R., Wu, G., Seshadri, R., and Wudl, F. (2017) "Perovskite-Related Hybrid Noble Metal Iodides: Formamidinium Platinum Iodide [(FA)₂Pt^{IV}I₆] and Mixed-Valence Methylammonium Gold Iodide [(MA)₂Au^IAu^{III}I₆]," *Inorg. Chim. Acta.*, 468: 280–284.
3. McCarthy, C. L., Cottingham, P., Abuyen, K., Schueller, E. C., Culver, S. P., and Brutchey, R. L. (2016) "Earth Abundant CuSbS₂ Thin Films Solution Processed from Thiol-Amine Mixtures," *J. Mater. Chem.*, 4: 6230–6233.
2. McCarthy, C. L., Downes, C. A., Schueller, E. C., Abuyen, K., and Brutchey, R. L. (2016) "Method for the Solution Deposition of Phase-Pure CoSe₂ as an Efficient Hydrogen Evolution Reaction Electrocatalyst," *ACS Energy Lett.*, 1: 607–611.
1. McCarthy, C. L., Webber, D. H., Schueller, E. C. and Brutchey, R. L. (2015) "Solution-Phase Conversion of Bulk Metal Oxides to Metal Chalcogenides Using a Simple Thiol-Amine Solvent Mixture," *Angew. Chem. Int. Ed.*, 54: 8378–8381.

Abstract

Structural Underpinnings of Magnetic and Electronic Behavior in Transition Metal Oxides and Chalcogenides

by

Emily Christine Schueller

Developing relationships between crystal structure and magnetic and electronic properties can clarify the origins of functional properties in materials with a complex array of interactions, including correlated electron behavior, magnetic ordering, and structural instabilities. Insight into the factors that underly materials properties can be used to both predict new functional materials as well as develop understanding of fundamental solid state physics phenomena. Through a combination of computational techniques like density functional theory and machine learning, as well as experimental techniques such as X-ray and neutron scattering, magnetic and physical properties measurements, and single crystal growth, it is possible to gain a detailed understanding of inorganic oxide and chalcogenide materials for use in a wide array of electronic and magnetic applications.

Crystal structure distortions in magnetic materials can drive the formation of chiral spin textures by breaking centrosymmetry and enabling the Dzyaloshinskii-Moriya interaction. A special type of chiral spin texture, known as a skyrmion lattice, is made up of vortices of magnetic spin that behave like particles and can be manipulated through an applied voltage, making them promising for computer memory applications. Understanding how crystal structure and magnetic behavior couple in skyrmion host materials can help us predict new skyrmion hosts with skyrmions stable over wider temper-

ature and magnetic field ranges. Symmetry-breaking can also contribute to insulator-metal transitions, a phenomenon where the electronic behavior of a material transitions from insulating to metallic, typically as a response to an external stimulus like temperature, pressure, or composition. In many insulator-metal transition materials, structural transitions like Jahn-Teller distortions or dimer formation localize electrons, leading to a change in electronic behavior.

Chapters 2 and 3 of this dissertation focus on the lacunar spinel family of materials, with a unique crystal structure consisting of tetrahedral clusters of transition metal atoms. We study two members of the family, GaV_4Se_8 , a known skyrmion host, and GaMo_4Se_8 , which we report as a novel skyrmion host. Through density functional theory and experiment, it is shown that in both materials small changes to the symmetry of a tetrahedral cluster have significant impacts on the magnetic behavior. Chapter 4 examines how local structure displacements of S atoms in $\text{BaCo}_{1-x}\text{Ni}_x\text{S}_2$ can be thought of as dynamic Jahn-Teller distortions and are related to the composition-driven insulator-metal transition in this solid solution. Chapter 5 reports on a combined machine learning and DFT pipeline to predict new trirutile materials as well as understand what factors determine whether a given $AB_2(\text{O/F})_6$ material will crystallize in the trirutile structure in order to develop insight into the mechanisms of crystal structure formation in ternary materials. Appendix A examines the crystal structure evolution of two hybrid perovskite materials to understand the origins of high photovoltaic performance in this material family.

Contents

Acknowledgments	v
Curriculum Vitae	vi
Abstract	viii
List of Figures	xiii
List of Tables	xvi
1 Introduction	1
1.1 Structure-property relationships in oxides and chalcogenides	1
1.2 Magnetism in the lacunar spinels	4
1.3 Insulator-to-metal transition in $\text{BaCo}_{1-x}\text{Ni}_x\text{S}_2$	7
1.4 Machine learning for crystal structure prediction	9
2 Modeling the structural distortion and magnetic ground state of GaV_4Se_8	13
2.1 Introduction	14
2.2 Methods	16
2.3 Results and Discussion	18
2.4 Conclusion	29
3 Structural evolution and skyrmionic phase diagram of the lacunar spinel GaMo_4Se_8	30

3.1	Introduction	31
3.2	Methods	33
3.3	Results	36
3.4	Discussion	48
3.5	Conclusion	50
4	Structural Signatures of the Insulator-to-Metal Transition in $\text{BaCo}_{1-x}\text{Ni}_x\text{S}_2$	51
4.1	Introduction	52
4.2	Methods	54
4.3	Results and Discussion	57
4.4	Conclusion	73
5	Factors Driving Crystallization in the Trirutile Structure	75
5.1	Introduction	76
5.2	Methods	78
5.3	Results	81
5.4	Conclusion	92
6	Summary and Outlook	94
6.1	Explaining the behavior of the Ta- and Nb-containing lacunar spinels	96
6.2	Extending study of the BaMS_2 system to other M -site atoms	97
6.3	Characterization of predicted trirutile materials	98
A	Crystal Structure Evolution and Notable Thermal Expansion in FASnI_3 and FaPbBr_3	100
A.1	Introduction	101
A.2	Experimental Methods	103
A.3	Results and Discussion	104
B	Structural evolution and skyrmionic phase diagram of the lacunar spinel GaMo_4Se_8	117
C	Factors Driving Crystallization in the Trirutile Structure	123

List of Figures

1.1	The prototypical crystal structure of the lacunar spinels	5
1.2	The layered crystal structure of the $BaMS_2$ family	7
2.1	The crystal structure of GaV_4Se_8 at 100 K	19
2.2	Distortion modes for the transition from T_d into C_{3v}	19
2.3	Magnetic and molecular orbital data for GaV_4Se_8	20
2.4	The PBE energy landscape for GaV_4Se_8 versus tetrahedral distortion . . .	23
2.5	GaV_4Se_8 energy landscape with varying U_{eff}	25
2.6	Spin-polarized band structure and densities of state for GaV_4Se_8	27
2.7	ACFDT-RPA produces a ground state consistent with experiment	28
3.1	XRD data shows $GaMo_4Se_8$ transitions into two space groups at low temperature	36
3.2	Asymmetric peaks suggest strain is present in $GaMo_4Se_8$	38
3.3	DFT and experiment point to $R3m$ as the ground state	40
3.4	Magnetic measurements reveal multiple magnetic phase transitions . . .	41
3.5	SANS and magnetometry confirm a skyrmion phase in $GaMo_4Se_8$	42
3.6	Modeling indicates the $Imm2$ phase is a uniaxial ferromagnet while the $R3m$ phase hosts a complex magnetic phase diagram	44
4.1	From magnetic and resistivity measurements, the insulator-metal transition occurs around $x=0.21$	58
4.2	Synchrotron diffraction indicates the average structure transition occurs between $x=0$ and $x=0.1$	59

4.3	From Rietveld refinements, the average structure gets less distorted as $x \rightarrow 1$	60
4.4	PDF data shows significant distortions of the $M - S$ bond length	61
4.5	PDF results show the low- x compounds have more significant local distortions	63
4.6	Reverse Monte Carlo modeling reveals a preference for basal S edge displacements	65
4.7	The lack of constraints from RMC modeling allows larger distortions of the square pyramids	66
4.8	A molecular orbital diagram for BaCoS_2 indicates a Jahn-Teller instability towards xy -plane symmetry breaking	68
4.9	Phonon calculations reveal a propensity for edge displacements of basal S atoms	70
4.10	DOS calculations show the Jahn-Teller symmetry breaking leads to opening of a band gap	71
5.1	The most common structure types in $AB_2(\text{O/F})_6$ composition space	82
5.2	The process flow for predicting new trirutile materials	83
5.3	Ionic radii perform reasonably well at clustering $AB_2(\text{O/F})_6$ material families	85
5.4	The most important features contain geometric and bonding information	87
5.5	A simplified decision tree for the formation of the trirutile structure	89
5.6	XRD data reveals CrSb_2O_6 and TiTa_2O_6 form in a disordered rutile structure	91
A.1	DSC and XRD data show multiple phase transitions for FASnI_3 and FAPbBr_3 on cooling	107
A.2	Temperature evolution of diffraction data for FASnI_3 and FAPbBr_3	108
A.3	Crystal structure evolution with temperature of FASnI_3 and FAPbBr_3	110
A.4	Atomic displacement parameters for FASnI_3 and FAPbBr_3 hint at local disorder	111
A.5	FASnI_3 and FAPbBr_3 have large coefficients of volumetric thermal expansion	113
A.6	Dielectric measurements on FAPbBr_3 indicate a glassy freeze-out of cation motion at low temperatures	115

B.1	dM/dT vs field data at various temperatures	118
B.2	AC χ' and χ'' data at various temperatures	118
B.3	Magnetization vs temperature data at various applied fields	119
B.4	Symmetry and orientation of $R3m$ and $Imm2$ cells	119
B.5	Magnetic cluster expansion fitting error for the $R3m$ and $Imm2$ phases of GaMo_4Se_8	120
C.1	Correlation matrix for 10 most important features	126

List of Tables

2.1	Comparison of PBE and ACFDT-RPA energies for different magnetic and structural configurations. ΔE is referenced to the lowest energy in the sequence of calculations.	26
3.1	Effective micromagnetic parameters for GaMo_4Se_8	45
4.1	XRF results show the observed composition for the solid solution is close to the nominal composition for all samples.	59
5.1	DFT-based stability calculations for predicted trirutiles. ΔE refers to the energy of the trirutile relative to its constituent binary oxides.	90
A.1	Crystallographic Data for FASnI_3	109
A.2	Crystallographic Data for FAPbBr_3	109
B.1	Magnetic Hamiltonian for the $R3m$ phase of GaMo_4Se_8	121
B.2	Magnetic Hamiltonian for the $Imm2$ phase of GaMo_4Se_8	122

Chapter 1

Introduction

1.1 Structure-property relationships in oxides and chalcogenides

The coupling between crystal structure and magnetic and electronic properties of materials is well known in transition metal oxide and chalcogenide materials. In the simplest form of structure-property coupling, the dimensionality of a crystal structure drives the dimensionality of magnetism and electronic properties, leading to properties like 1D magnetic ordering or anisotropy between in-plane and out-of-plane conductivity. More subtly, symmetry-breaking is at the heart of many fundamental phenomena in solid state physics, including the formation of exotic magnetic phases and insulator-to-metal transitions. For example, the Dzyaloshinskii-Moriya interaction (DMI), which is correlated with spin-orbit coupling and responsible for the formation of canted spin phases, is only non-zero in materials without a center of inversion; namely, in crystal structures with chiral or polar point groups.

Skyrmions are a special type of canted spin phase comprised of topologically protected spin vortices which are typically 10 nm to 100 nm in diameter. These vortices can be moved through a material with an applied voltage, making them attractive for racetrack memory and other spintronic applications [2]. However, a challenge in the technological application of skyrmion devices is that in most known bulk skyrmion hosts, the stability range of skyrmions extends only over small ranges of temperature and applied magnetic field [3]. The physics underlying skyrmion formation in bulk materials is complex and highly material dependent. The skyrmion phase often competes with other magnetic phases such as helices or cycloids, and the formation of skyrmions depends on a delicate balance between magnetic exchange, DMI, and magnetocrystalline anisotropy energies, which are sensitive to small changes in the symmetry and chemistry of materials [4]. Therefore, it is necessary to perform careful experimental characterization in combination with computational modeling in order to fully understand how chemistry and crystal symmetry affect the formation and stability of skyrmion phases. A detailed understanding of skyrmion formation is crucial to design new skyrmion host materials with improved stability.

Another interesting phenomenon in solid-state physics is the insulator-to-metal transition (IMT). This transition can be induced by a variety of external stimuli such as temperature, pressure, or composition. In some materials, resistivity values can change by several orders of magnitude over a small temperature range [5], which makes IMT materials promising candidates for electronic switching applications. Furthermore, from a more fundamental standpoint, materials at the border between insulator and metal often have interesting magnetic and electronic properties. This is especially true in the so-called anomalous metal regime, which is thought to have physics similar to that of 2D superconducting materials [6].

Insulator-metal transitions are often strongly coupled to the underlying crystal structure of a material; specifically, the typically higher symmetry metallic phase often hosts a structural instability that drives the transition into the insulating state. One such type of instability is a Jahn-Teller distortion where symmetry breaking in the crystal field leads to electron localization, as seen in the perovskite manganites [7, 8]. Another instability associated with insulator-to-metal transitions is a dimerization transition, often observed in the rutile family [9]. For example, in VO_2 the covalent metal-metal bonding on vanadium dimers at low temperatures localizes electrons on the bond, leading to an insulating state [10]. In compositionally driven insulator-to-metal transitions which involve the doping of holes or electrons into a semiconducting system, the ability of holes or electrons to percolate through a material and induce an electronic transition depends on how the dopant atoms incorporate into the crystal structure and whether they tend to cluster or cause local distortions [11]. In some insulator-metal transition materials, like doped LaMnO_3 , rather than an average structure transition, the transition is associated with dynamic symmetry breaking [12], requiring more sophisticated techniques than simple diffraction to gain a complete understanding of the underlying mechanisms.

Understanding how distortions in crystalline materials impact their properties is key for designing better-performing functional materials. However, in many transition metal oxides and chalcogenides, this is a difficult task due to the complex interactions involved, including correlated electrons, magnetism, and average and local structural instabilities. Understanding the coupling of structural effects with correlated electron physics and magnetic transitions requires a detailed experimental investigation of crystallography, magnetic and electronic properties, in addition to fundamental band structure calculations. In order to examine the effect of crystal structure on properties, we

choose three material families as case studies. The first is the lacunar spinel family, a family of chalcogenides which are characterized by a unique molecule-like crystal structure and host complex magnetic and electronic behavior including low temperature skyrmion phases and pressure-induced insulator-to-metal and superconducting transitions. The second is the $\text{BaCo}_{1-x}\text{Ni}_x\text{S}_2$ solid solution, with a 2D-like layered structure in which substitution of 22% of Co by Ni results in an insulator-to-metal transition. The final family is the trirutile family with formula $AB_2(\text{O/F})_6$. The trirutiles crystallize in an ordered supercell of the rutile structure and many members display 1D antiferromagnetic behavior.

1.2 Magnetism in the lacunar spinels

The lacunar spinel family, with chemical formula AB_4Q_8 , has a cubic $F\bar{4}3m$ crystal structure characterized by tetrahedral clusters of transition metal (B -site) atoms. The A -site is typically Ga or Ge, the B -site is an early transition metal, and the Q -site is a chalcogen like S or Se. The crystal structure as well as the molecular orbital diagram for a cluster is shown in Figure 1.1. Covalent metal-metal bonds induce “molecular”-like behavior of the clusters, which creates interesting magnetic and electronic properties including significant correlated electron behavior. Conductivity in the lacunar spinels occurs through hopping from cluster to cluster, demonstrated experimentally by a Mott variable-range-hopping-like temperature dependence of resistivity. In lacunar spinels with Ta or Nb on the B -site, an insulator-to-metal as well as a superconducting transition is induced by pressure [13]. The low temperature magnetic behavior of the Ta and Nb lacunar spinels is still debated, although a leading hypothesis is the formation of a spin singlet state at low temperature [14].

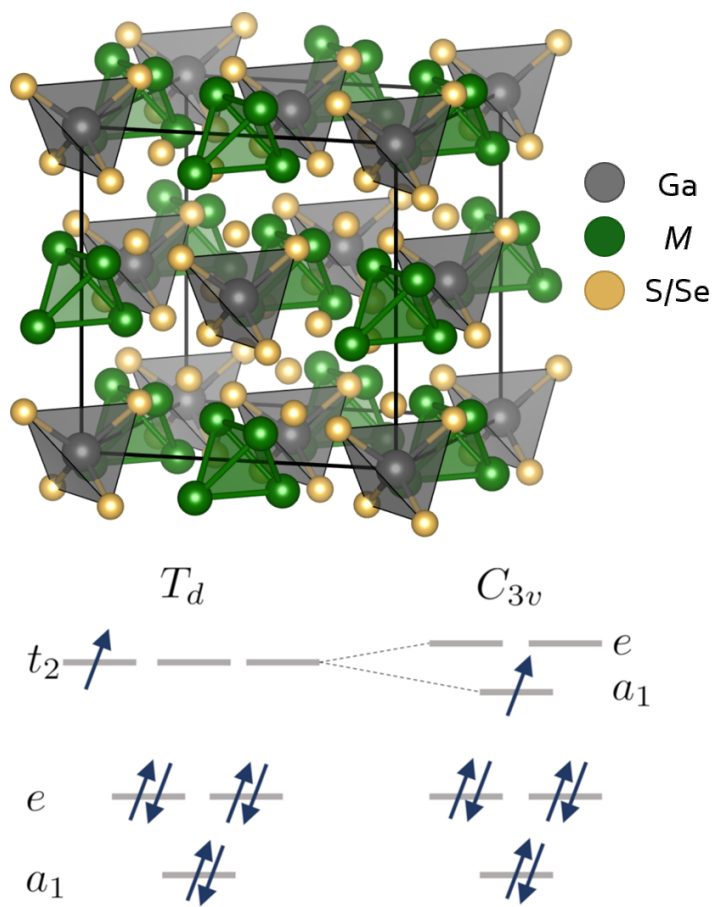


Figure 1.1: The lacunar spinel crystal structure is characterized by tetrahedral clusters of transition metal atoms. The molecular orbital (MO) diagram for the high temperature crystal structure exhibits an instability towards a Jahn-Teller distortion. A characteristic MO diagram for the distorted low temperature structure of the V and Mo containing lacunar spinels is shown.

The V- and Mo-containing lacunar spinels ($\text{Ga}(\text{V}/\text{Mo})_4(\text{S}/\text{Se})_8$) exhibit multiferroic behavior, with a Jahn-Teller distortion to a polar $R3m$ structure between $T=40$ K and $T=50$ K, and magnetic ordering between $T=15$ K and $T=30$ K. GaV_4S_8 and GaV_4Se_8 have complex magnetic phase diagrams including cycloidal and skyrmion phases, and reports show skyrmion stability ranging over 15 K and 100 mT [15, 16]. The Jahn-Teller instability, with 1 (V) or 5 (Mo) electrons in the t_2 orbital of the tetrahedral cluster, leads to a transition into the polar $R3m$ space group at 40 K to 50 K, depending on the material. A characteristic change in the molecular orbital diagram through the Jahn-Teller transition in the V compounds is shown in Figure 1.1. The Jahn-Teller distortion drives the magnetic ordering, which tends to occur around 20 K below the structural transition, as the formation of canted spin phases is enabled by the polar nature of the low temperature phase. The presence of magnetic moment on molecular rather than atomic orbitals leads to strong coupling between the symmetry of the cluster and the magnetic behavior of these materials. We study the crystal structure and magnetism of GaV_4Se_8 and GaMo_4Se_8 in Chapters 2 and 3 to understand the relationship between distortions of the tetrahedral clusters and magnetic behavior.

One technique that can be used to probe the presence of a skyrmion phase is magnetoentropic mapping. The Maxwell relation

$$\left(\frac{\partial M}{\partial T}\right)_H = \left(\frac{\partial S}{\partial H}\right)_T$$

can be used to obtain a quantity that is difficult to probe directly (magnetic entropy) from a quantity that is straightforward to acquire through magnetometry measurements (magnetization). By performing temperature-dependent magnetization measurements at multiple applied magnetic fields (H), one can overlay $(\frac{\partial M}{\partial T})_H$ on a field vs temperature plot (also known as a magnetoentropic map) in order to look for field-

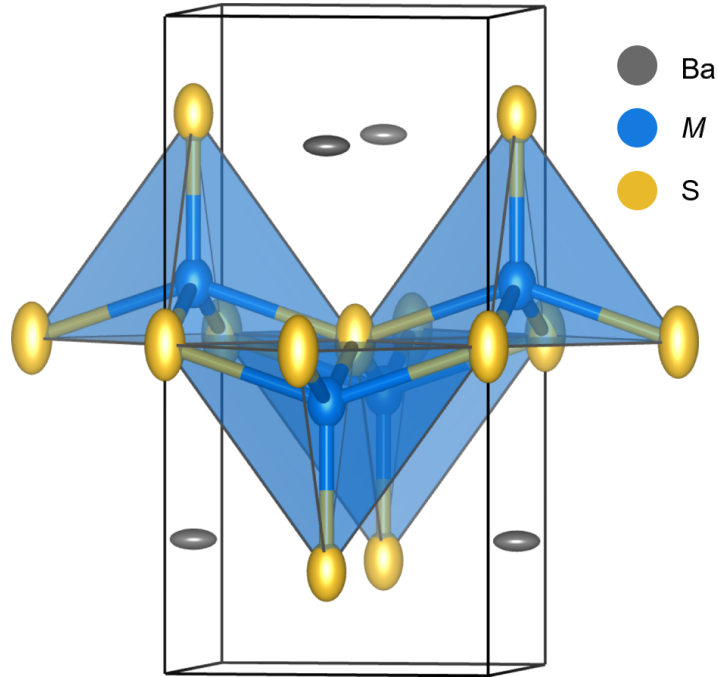


Figure 1.2: BaNiS₂ has a layered crystal structure with slightly distorted square pyramidal coordination of the Ni. BaCoS₂ exhibits a small monoclinic distortion in the plane of the layers.

driven magnetic transitions associated with a change in magnetic entropy. Because skyrmions are theoretically and experimentally known to be a high entropy magnetic phase, the transition into a skyrmion phase is often associated with a positive entropy anomaly in a magnetoentropic map. With this technique, in conjunction with small angle neutron scattering and DFT-based modeling, it is possible to determine the presence and field/temperature boundaries of a skyrmion phase in a new material.

1.3 Insulator-to-metal transition in BaCo_{1-x}Ni_xS₂

The solid solution BaCo_{1-x}Ni_xS₂ undergoes a compositionally-driven insulator-to-metal transition when approximately 22% of the Co is substituted with Ni ($x_c=0.22$) [17]. While the substitution of Ni for Co can be thought of as electron doping, the

electronic picture is more complicated because multiple orbitals are involved at the Fermi level and BaCoS_2 is not a typical band insulator [18]. The crystal structure is layered with distorted M -S square pyramids alternating with layers of Ba, as shown in Figure 1.2. All members of the solid solution have a tetragonal $P4_2/nmm$ space group except the BaCoS_2 end member which has a slight monoclinic distortion to $P2/c$. However, this average structure distortion is not associated with the electronic transition, which occurs at a higher percentage of Ni. Both end members of the solid solution have interesting magnetic and electronic behavior. BaCoS_2 is an antiferromagnetic charge-transfer insulator with strongly correlated electrons. BaNiS_2 is a paramagnetic metal with reported topological surface states [19]. The replacement of Co with Ni suppresses the Neel temperature and the moment of the antiferromagnetic phase until the IMT composition, although some reports suggest a small composition window with an antiferromagnetic metallic state. The intermediate members also form non-stoichiometric sulfur vacancy compounds that exhibit unusual insulator-to-metal transitions upon cooling, highlighting the competing interactions present in this family [20]. While the average structure does not show a change across the insulator-to-metal transition, no reports had been made on the local structure evolution. In order to look for structural origins of the IMT, we turn to pair distribution function analysis across the solid solution.

The pair distribution function (PDF) technique is a method for studying the local structure of materials. PDF data can be obtained by taking the Fourier transform of total scattering data which yields a histogram of atom-atom distances in a material. The PDF technique was originally developed for the study of amorphous or glassy materials, such as silica [21], but has been extended to materials which appear crystalline from diffraction [22]. For these materials, PDF data can be used to study local struc-

ture distortions that are dynamic or lack long-range order and therefore cannot be seen with traditional diffraction techniques. Local distortions are important for determining properties in many types of electronic materials. For example, local structure distortions can be related to the high performance of the hybrid perovskites as photovoltaic absorbers, which are known for their defect tolerance. In these materials, it has been shown that the lone pair of electrons on the Pb^{2+} or Sn^{2+} ions leads to local offcentering within the octahedra in the inorganic sublattice [23]. One hypothesis is that the offcentering creates dynamic polarizability in the material, allowing for better screening of charge carriers, which leads to longer carrier lifetimes even in the presence of crystalline defects. The structural evolution of some hybrid perovskites is explored in Appendix A. In IMT materials, symmetry breaking due to dynamic Jahn-Teller distortions has been shown to lead to an insulating state in LaMnO_3 [12]. The study of local structure can allow us to explain properties that are not readily apparent from average structure studies.

1.4 Machine learning for crystal structure prediction

Because of the close relationship between crystal structure and properties, it has long been a goal to predict crystal structures of inorganic materials based only on composition. While compounds in organic chemistry often follow strict structural rules, inorganic materials have a wide variety of arrangements and predicting them *ab initio* is difficult, especially considering the complex interactions between crystal structure and electron correlations, magnetism, and other competing energetics. However, advances in computational technology have made this problem more tractable. Density functional theory (DFT), a quantum mechanical simulation tool, can be used to compare

the ground state energy of potential crystal structures for a given composition, as well as perform calculations of phonon spectra to look for structural instabilities. However, this is a computationally intensive process and differences in DFT functionals for correlation and exchange energy calculations can change the relative stability of various polymorphs. More recently, there has been exploration of machine learning methods for crystal structure prediction [24]. Machine learning provides some advantages over DFT-based methods; namely, it is much less computationally intensive and can be used to quickly classify hundreds of materials, and the use of features in machine learning allows one to glean insights about the underlying chemistry driving crystal structure formation.

A typical approach to machine learning for crystal structure prediction can be described as follows. A training data set of known materials is tabulated from one of the crystallographic databases such as the ICSD. Depending on the scope of the machine learning model, this data set can be as large as all ternary oxides [25], or more focused on specific material families. An important step in machine learning is cleaning and processing training data, since the final model is only as good as the data it contains. This involves steps like removing duplicates and undesirable compounds, as well as dealing with polymorphs in which multiple crystal structures are reported for the same compound. Depending on the goal of the project, the “target” column can be binary, where a 1 is assigned to the target crystal structure, and a 0 is set for all others. For more complicated models, in which the algorithm is choosing the most likely structure from multiple structural families, generation of the target column may be more difficult and require connectivity analysis to determine the grouping of structures into structural families.

Once a cleaned and processed training set is acquired, the next step is featurizing

the data. For crystal structure prediction, data based on crystal structure cannot be included, so the features are limited to composition based features such as atomic radii of the elements in the material. A helpful software tool for featurizing datasets in python is matminer [26], which pulls features from multiple databases such as the Magpie (A Materials-Agnostic Platform for Informatics and Exploration) database and the pymatgen [27] database. To pare down the feature set to a more manageable size, several methods are available. A popular method is principal component analysis (PCA) which decomposes the feature matrix into linear combinations that preserve the most information (variance) while reducing the dimensionality of the dataset. This method is efficient but has a disadvantage of removing feature names, making the final results of the model difficult to interpret. Another method is tree-based feature reduction, often employed in recursive feature elimination. Tree-based feature reduction uses decision trees to determine the features that are most important by looking at how removal of individual features affects the model's performance. Recursive feature elimination iteratively removes the least important features with a decision tree until the desired number of features is achieved. The advantage of tree-based methods is that feature names are kept, so it is possible to look at how various features are associated with different structural families— for example, large electronegativity differences may be associated with ionic crystal structures— as well as gain understanding into the most important features for certain crystal structure formation.

With a pruned, featurized data set, different classifier algorithms can be compared using cross validation, where the training data is split into smaller sets for training and testing the model. Some best practices for fitting and evaluating machine learning algorithms are enumerated by Wang and coworkers [28]. Once the model is optimized, if the performance on the test data is similar to the performance on the training data,

the model is likely to perform consistently on unknown data as long as the unknown data shares similar characteristics to the training data. The model can then be used to predict the crystal structure of new materials and can also be analyzed to understand what features are most important in driving crystal structure formation.

The trirutile family of materials with composition $AB_2(O/F)_6$, has a structure related to the rutile structure, with chains of edge-sharing octahedra along the c -direction. While many rutiles have an instability towards dimerization of neighboring atoms in the c -direction, leading to insulating behavior, the trirutiles are mostly insulating even without dimerization due to electron localization induced by the disruption of chains from alternating A and B atoms. However, many trirutile oxides exhibit unusual 1D antiferromagnetic behavior. Additionally, the $AB_2(O/F)_6$ composition space has many competing structural families, so it is interesting to study crystal structure formation in this space in order to understand why some compounds form the trirutile structure rather than other structures. In Chapter 5, we apply the machine learning methods described earlier to both understand the factors driving crystallization in the trirutile structure type as well as predict potential new trirutile candidates.

Chapter 2

Modeling the structural distortion and magnetic ground state of the polar lacunar spinel GaV_4Se_8

The lacunar spinel GaV_4Se_8 is a material whose properties are dominated by tetrahedral clusters of V atoms. The compound is known to undergo a polar distortion to a ground state structure in the $R3m$ space group, and orders ferromagnetically with a relatively small magnetic moment. We develop an understanding into the relationship between crystal structure and magnetic order in this material, and the influence of electron correlations in establishing the observed ground state using first-principles density functional theory (DFT) electronic structure calculations. Because electrons are delocalized within V_4 clusters but localized between them, the usual approaches to simulate electron correlations — such as the use of the Hubbard U in DFT + U schemes

The contents of this chapter have substantially appeared in Reference [29]. Reproduced with permission from: E. C. Schueller, J. L. Zuo, J. D. Bocarsly, D. A. Kitchaev, S. D. Wilson, and R. Seshadri, Modeling the Structural Distortion and Magnetic Ground State of the Polar Lacunar Spinel GaV_4Se_8 *Phys. Rev. B* 100 (2019) 045131. Copyright 2019 American Physical Society

— do not adequately recreate the experimental ground state. We find instead that the experimental ground state of GaV₄Se₈ is well-represented by the random-phase approximation to the correlation energy. Additionally, we find that magnetism and crystal structure are strongly coupled in this material, and only certain arrangements of magnetic moment within a V₄ cluster can stabilize the observed structural distortion. In combination with the anisotropic, polar nature of the material, the strength of magnetostructural coupling indicates that application of strain could be used to tune the magnetic properties of GaV₄Se₈.

2.1 Introduction

GaV₄Se₈ is a member of the lacunar spinel family which has garnered much attention in recent years.[15, 16, 30–32] The lacunar spinel structure is related to the typical AB₂O₄ spinel structure but with ordered vacancies on the A-site that induce a breathing mode distortion in the material, reducing the symmetry from $Fd\bar{3}m$ to $F\bar{4}3m$. Most significantly, the pyrochlore lattice of corner-connected tetrahedra of B-site atoms in the spinel becomes a lattice of isolated tetrahedra in the lacunar spinel. The properties of lacunar spinel materials are dominated by these clusters of transition metal atoms. For example, most exhibit a variable range hopping-type conduction, indicating electrons must hop between clusters rather than being delocalized through the material.[33] GaV₄Se₈ in particular has a small band gap at low temperature of about 0.1 eV.[31] Some members of the family, such as GaNb₄Se₈ and GaTa₄Se₈, undergo superconducting and insulator-to-metal transitions under pressure.[13, 34]

GaV₄Se₈ undergoes a polar Jahn-Teller distortion along the $\langle 111 \rangle$ axis from $F\bar{4}3m$ to $R3m$ upon cooling through 41 K.[31, 35] Below this temperature, at approximately

17.5 K, GaV₄Se₈ magnetically orders with an ordered moment of around $1 \mu_B$ per cluster of four V atoms, in agreement with molecular orbital theory arguments.[31] In the magnetically ordered regime, GaV₄Se₈ hosts a rich magnetic phase diagram, with a cycloidal ground state, a skyrmion region near the ordering temperature, and a field-polarized phase at high fields.[15, 16] Because of strong crystalline anisotropy along the polar $\langle 111 \rangle$ axis, the stability of phases strongly depends on the angle at which the magnetic field is applied relative to the $\langle 111 \rangle$ axis. The combination of the polar symmetry and magnetic order makes GaV₄Se₈ a multiferroic material, which could be promising for various computing and memory applications.[30]

Because magnetism, crystal structure, and electronic structure are strongly coupled in GaV₄Se₈, it can be challenging to interpret computational results. Magnetic measurements reveal a moment of $1 \mu_B$ per tetrahedral cluster, but there are many ways this could arise, and the precise manner in which the total moment is distributed across the cluster is unclear. Furthermore, the partial delocalization of electrons in the V₄ tetrahedra is strongly dependent on electronic correlations, which are not readily modeled within density functional theory (DFT). The impact of electron correlation effects can be approximated in DFT using on-site Coulomb (U) and exchange (J) interactions which are applied to orbitals with correlated electrons, such as the d-orbitals of V. This approach is now commonly known as DFT+ U , [36] and is frequently employed using a single parameter $U_{eff} = U - J$. [37] However, as we find here, GaV₄Se₈ has additional complexity because electrons can be delocalized across the four V atoms of a cluster yet remain localized to one cluster. In other words, the application of U_{eff} on individual V atoms does not capture the correct electronic ground state. The adiabatic connection fluctuation-dissipation theorem implementation of the random phase approximation (ACFDT-RPA) is a way to account for electron correlations and non-local effects in a

more rigorous manner.[38] Total energy calculations with this method combine the exact exchange energy from the Hartree-Fock approximation with the correlation energy from ACFDT-RPA to provide accurate ground state predictions even for complicated materials with competing structural and magnetic ground states.[39, 40]

To help lay down the basis for the computational modeling, we first prepare and measure the magnetic properties of GaV₄Se₈ single crystals. We then examine the energy landscape of GaV₄Se₈ using density functional theory calculations (with varying U_{eff} values) as well as ACFDT-RPA total energy calculations to understand the relative stability of different magnetic and structural ground states. We show that magnetism and crystal distortion are strongly coupled, and the Jahn-Teller distortion can only be stabilized with a specific arrangements of moments on the V₄-cluster. Additionally, we find that the use of ACFDT-RPA is required to recover the ground state which recreates the semiconducting behavior, elongating Jahn-Teller distortion, and net magnetic moment observed experimentally.

2.2 Methods

2.2.1 Experimental

Phase pure GaV₄Se₈ powder was obtained by reaction of Ga pieces and ground V and Se powders with an approximately 50% excess of elemental Ga. The elements were reacted in an evacuated fused silica tube with a heating ramp rate of 50° C/hour to 950° C, held for 24 h and furnace cooled. To obtain single crystals, vapor transport was performed using approximately 500 mg of the formed powder mixed with 30 mg of PtCl₂ as a transport agent in an evacuated fused silica tube with a diame-

ter of 6 mm and a length close to 20 cm. The tube was held with the powder end at 960° C and the growth end at 920° C for two weeks to obtain 1-3 mg black, cuboidal, lustrous single crystals. Single crystal X-ray diffraction was performed at 100 K with a Bruker KAPPA APEX II diffractometer equipped with an APEX II CCD detector using a TRIUMPH monochromator with a Mo K α X-ray source ($\lambda = 0.71073 \text{ \AA}$). Structure refinement was carried out using the Jana crystallographic computing system.[41] Crystal structures were visualized using the VESTA software suite.[42] Magnetic measurements were performed on a Quantum Design MPMS 3, with the sample mounted by attaching a crystal to a plastic drinking straw using KaptonTM tape. The cuboidal shape of the crystals permitted the (100) axis of the crystal to be approximately aligned with the applied magnetic field using an optical microscope.

2.2.2 Computational

All electronic structure calculations were performed using the Vienna Ab Initio Simulation Package (VASP)[43] with the VASP recommended projector-augmented-wave pseudopotentials[44, 45] within the Perdew-Burke-Ernzerhof (PBE) generalized gradient approximation (GGA).[46] PBE+ U calculations were performed using the U_{eff} approach applied to the d-orbitals of V.[37] Relaxations along distortion modes were performed using selective dynamics with the conjugate gradient algorithm for ionic relaxations. For relaxations a Γ -centered K -point grid of $4 \times 4 \times 4$ was employed. For these, a three step system was carried out in which the cell volume and ions were relaxed first, then just the ions, with Gaussian smearing with a sigma of 0.1. After the structure was relaxed, a static energy calculation was performed with the tetrahedron method with Blöchl corrections for more accurate total energy values. For band structure and density of states calculations a K -point grid of $8 \times 8 \times 8$ was used. For

the ACFDT-RPA simulations,[38] a K -point grid of $2 \times 2 \times 2$ was used with 16 frequencies sampled (at which point the correlation energy converged within 0.1 meV/atom). For all calculations an energy cutoff of 500 eV, around 1.75 times the maximum default cutoff energy, was determined to be optimal. For the lowest and highest energy ACFDT-RPA magnetic configurations, total energy calculations were repeated with unit cell volumes changed by $\pm 2\%$ to confirm that the equilibrium ACFDT-RPA cell volume was close to the PBE cell volume. In order to generate structures along distortion modes, an $R3m$ structure with mode decomposition information was created with ISODISTORT[47] which contained amplitudes of distortion modes used to generate the structure from the high symmetry $F\bar{4}3m$ structure. A python script was used to systematically vary the amplitudes of chosen distortion modes (A_1 and E) and generate new structures for calculation with VASP. Calculation results were parsed and visualized with the python package pymatgen.[27] Band structure visualization employed the sumo package.[48]

2.3 Results and Discussion

GaV₄Se₈ has a molecules-in-crystal structure with isolated tetrahedral clusters of transition metal atoms, as shown in Fig. 2.1, a structure fit from high resolution single crystal X-ray diffraction (XRD) measurements taken at 100 K. From molecular orbital theory, it is expected that in the high temperature phase, the cluster has T_d symmetry with one electron in the t_2 orbital, making it unstable to a Jahn-Teller distortion. In GaV₄Se₈, this distortion occurs around 41 K along the $\langle 111 \rangle$ direction, lowering the structural symmetry to $R3m$.[31] This makes one V atom on the cluster (V1, shown in blue in Fig. 2.2) inequivalent from the other three (V2, shown in green in Fig. 2.2).

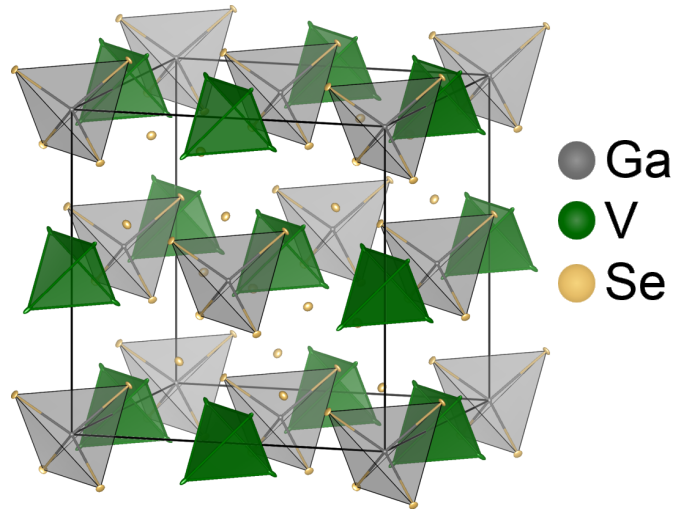
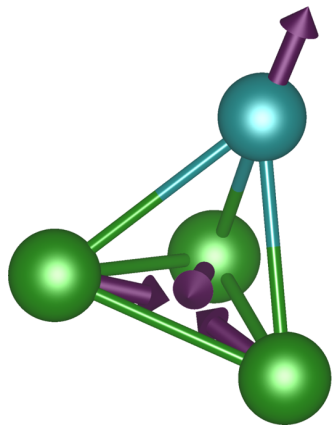


Figure 2.1: The crystal structure of GaV₄Se₈ at 100 K is best fit to the expected $F\bar{4}3m$ space group from single crystal XRD. Highly anisotropic V ADPs (shown at 99%) along the axis of the low temperature Jahn-Teller distortion indicate possible local distortions of the material above the global phase transition temperature of 41 K.

(a) $\Gamma_4: V A_1$



(b) $\Gamma_4: V E$

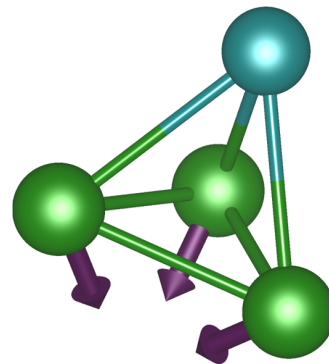


Figure 2.2: The A_1 (a) and E (b) modes that distort the high symmetry (T_d) V tetrahedra into their low symmetry (C_{3v}) clusters. The V1 atom is shown in blue and the V2 atoms are shown in green.

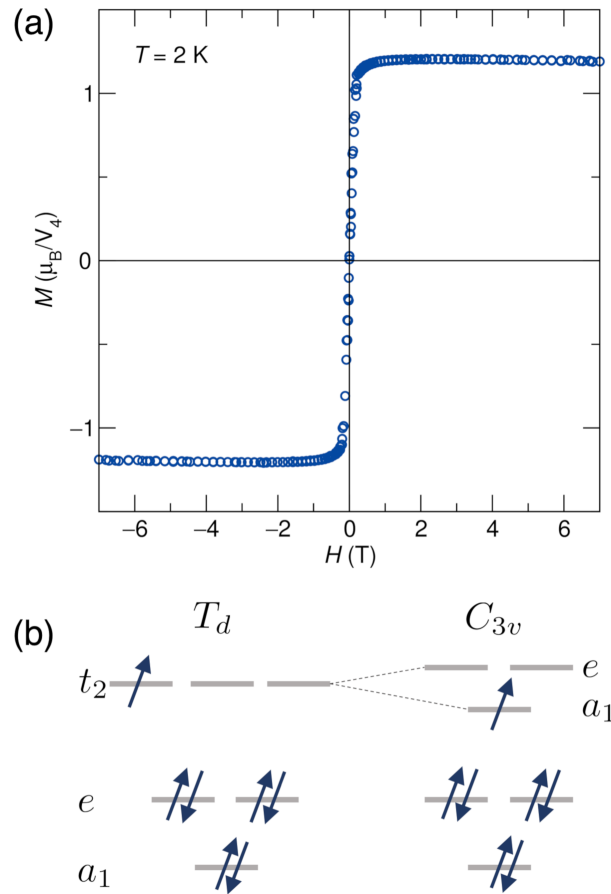


Figure 2.3: (a) Field-dependent magnetization data of a GaV₄Se₈ single crystal at 2 K shows the saturation magnetization is approximately $1.1 \mu_B$. (b) The molecular orbital diagram of the V_4 cluster without and with the Jahn-Teller distortion (space groups changing from $F\bar{4}3m$ to $R\bar{3}m$) with a net moment of $1 \mu_B$ per V_4 cluster.

Even in the high temperature, nominally cubic phase, the single crystal XRD refinement on 100 K data indicates V atomic displacement parameters which are highly anisotropic and point along the $\langle 111 \rangle$ directions, indicating local Jahn-Teller distortions are likely present above the global phase transition temperature.[49, 50] The measured saturation magnetization of GaV₄Se₈ is $1.1 \mu_B$ per V₄ cluster as shown in Fig. 2.3(a). Following the Jahn-Teller distortion, the cluster has C_{3v} symmetry, splitting the degenerate t_2 into a half-filled a_1 orbital and an empty e orbital, as shown in Fig. 2.3(b).[35] Molecular orbital theory yields a moment of $1 \mu_B$ per V₄, matching what is measured in experiment.

In order to more fully understand the unusual structural and magnetic properties GaV₄Se₈, we wished to probe the underlying physics governing the magnetic and structural ground state, as well as investigate the distribution of moment across the pseudo-tetrahedral cluster of V atoms which is difficult to study experimentally. To do this, we performed density functional theory calculations in VASP using the PBE functional. We began with a typical magnetic initialization of $3 \mu_B$ per V atom, but found that this resulted in a relaxed structure with a moment of around $5 \mu_B$ per cluster, far higher than the experimental and molecular orbital theory predicted values. Because in the $R\bar{3}m$ structure, one V is inequivalent from the other 3 in the cluster, there are several possible collinear arrangements of moments that are compatible with the space group symmetry. We focus on three possible magnetic configurations: the previously mentioned high moment configuration, which we will call HFM, a ferrimagnetic configuration where the inequivalent V1 is spin up and the three V2 are spin down, which we will call FI1 if it is accompanied by a compressive structural distortion and FI2 if the accompanying distortion is elongative, and a low moment configuration where the moment on each V is initialized to $0.5 \mu_B$, which we will call LFM. We find that the crystal distortion

is strongly coupled to the magnetic configuration, and the reported low temperature experimental structure is *not* the most stable structure for all of the magnetic configurations. Because all of these variables are highly correlated, a systematic approach is required to obtain a full picture of the energy landscape.

Starting from the high symmetry $F\bar{4}3m$ structure, group theory can be used to generate linearly independent sets of vectors (distortion modes) that the atoms follow from their high symmetry positions to their positions in the lower symmetry $R3m$ structure. The full transformation from the $F\bar{4}3m$ to $R3m$ unit cell for GaV₄Se₈ has ten linearly independent displacive modes, but we focus on the two that affect the motion of the V atoms, A_1 and E , because the V atoms control the magnetism and contribute the most to the band structure around the Fermi energy. These modes, illustrated in Fig.2.2 (a) and (b) respectively, distort the shape of the tetrahedron and translate it within the unit cell. When the amplitudes of both modes are 0, this generates a perfect tetrahedron, corresponding to the undistorted, cubic phase. The amplitudes of these two modes are systematically varied to generate structures with an array of different shapes and positions of the V cluster within the unit cell.

These structures are simulated with VASP to understand the coupling between the shape of the tetrahedron and the energies of various magnetic configurations. In order to isolate these modes we fix the positions of the V atoms within the structure and relax other ion positions as well as lattice parameters and cell shape. However, in doing so we remove the translation effect of the A_1 and E modes, and therefore their independence. To reduce the dimensionality of the analysis, we combine the effect of the two modes into a tetrahedral distortion parameter which is a difference of bond

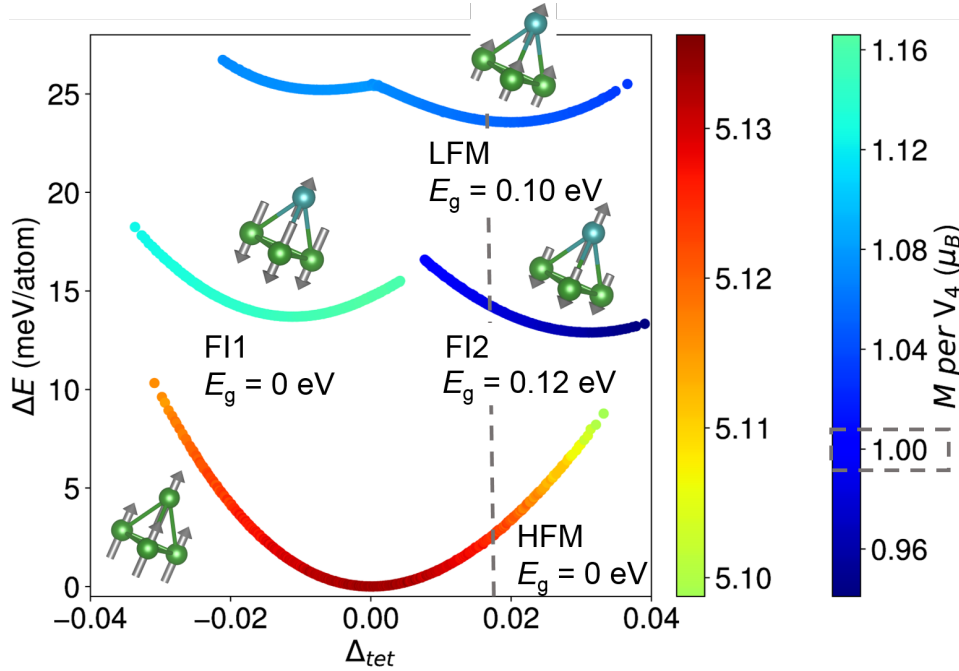


Figure 2.4: The calculated energy landscape within PBE for GaV₄Se₈ versus tetrahedral distortion with $U = 0 \text{ eV}$. The arrows on the tetrahedra are representative magnetic structures, which are accompanied by text labels, for each parabola and the colors of the atoms represent their structural equivalence. The colors of the parabolas are the net moment for each structure. The dashed grey lines represent experimentally observed values of Δ_{tet} and net moment. The ground state structure (HFM) within PBE has a far higher net magnetic moment than the experimentally observed value.

lengths between V1 and V2 and between V2 and V2:

$$\Delta_{tet} = \frac{d_{[V1-V2]} - d_{[V2-V2]}}{d_{[V1-V2]} + d_{[V2-V2]}}$$

Within PBE and without any effort to correct for electron correlation, we find the energy landscapes shown in Fig. 2.4. The high moment configuration (HFM, $5 \mu_B/V_4$) is found to be the most stable for all distortions of the tetrahedral cluster. Structurally, this magnetic configuration has an energetic minimum at no tetrahedral distortion, with the unit cell relaxing to the high temperature $F\bar{4}3m$ structure. Additionally, it has a metallic band structure, unlike the experimental semiconducting behavior, which

is unsurprising given the small degree of structural distortion. Therefore, we see that the ground state calculated by PBE alone does not reproduce the electronic, crystal structure, or magnetic behavior observed in experiment.

The two higher energy parabolas (around 10 meV/atom higher in Fig. 2.4) represent magnetic structures with ferrimagnetic configurations on the cluster (FI1 and FI2). On the right side, there is a ferrimagnetic state with a strong moment on V1 and weak opposing moments on V2 (FI2). This magnetic configuration couples with an elongative Jahn-Teller distortion where the V1 atom is far from V2 and V2 are close to each other (as in the experimental structure). On the left side, the Jahn-Teller distortion is compressive with V1 close to the V2 and V2 pushed farther from each other. The ferrimagnetic state created, FI1, has a weaker moment on V1 and stronger opposing moments on V2. The FI2 configuration on the right side (elongative Jahn-Teller) has a small band gap, while the left side (FI1) configuration is gapless. Finally, the highest energy parabolas are low moment ferromagnetic configurations with a $1 \mu_B$ moment essentially delocalized across each cluster. The minimum on the right side (LFM) is again gapped. This high energy configuration agrees most closely with the experimental crystal distortion, net magnetic moment, and band gap. Therefore, without accounting for electron correlations, we obtain a metallic ground state with a nearly cubic structure and a large moment.

Since V is a $3d$ atom, it is not surprising that it may be necessary to account for electron correlations; for example, in the form of a Hubbard U , which promotes electron localization on specific V d-orbitals, to correctly represent the ground state of a V-containing compound. We repeated the systematic generation of an energy landscape for increasing values of U_{eff} within PBE. Energy landscapes for $U_{eff} = 0.9$ eV and $U_{eff} = 3$ eV are shown in Fig. 2.5. While a value for U_{eff} of 3 eV stabilizes a gapped

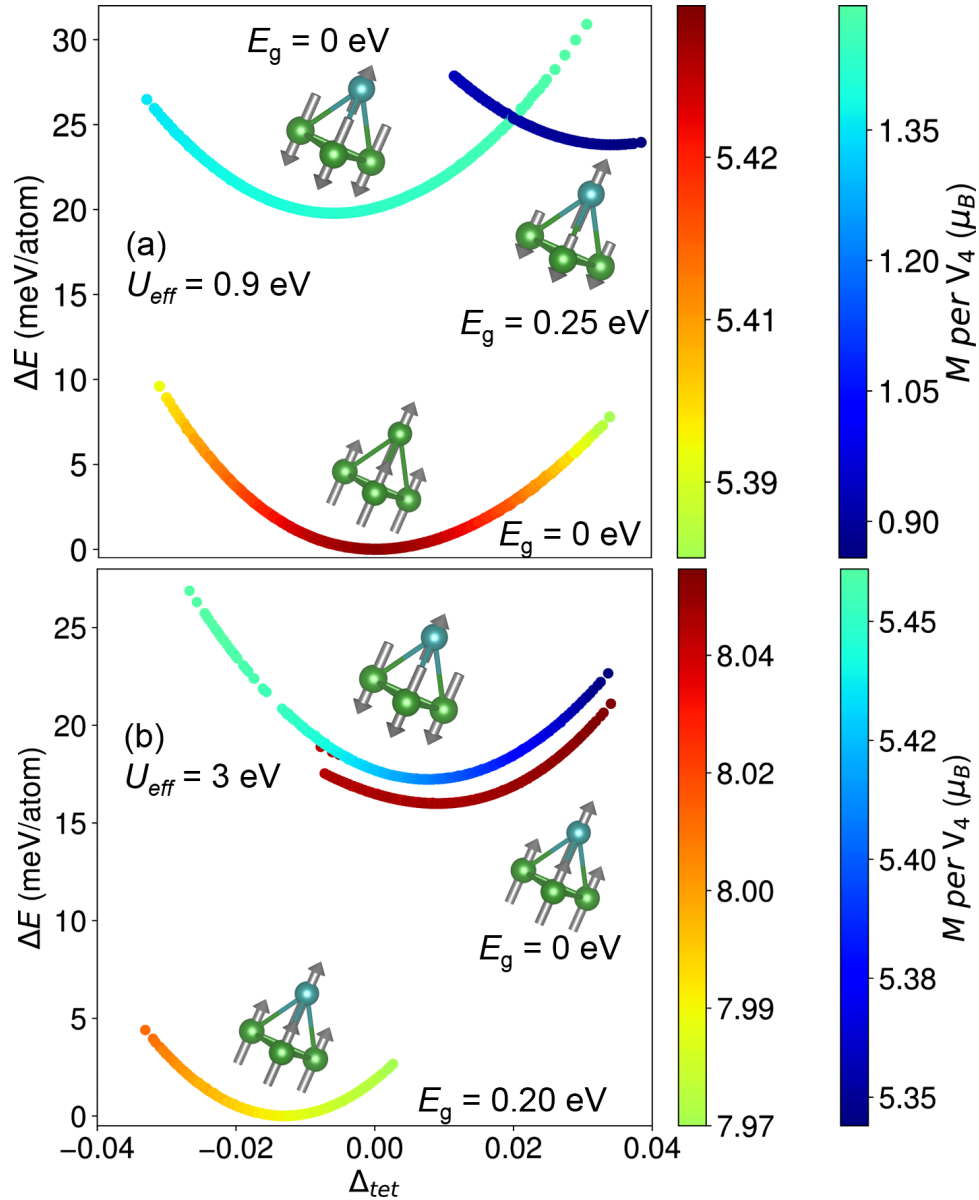


Figure 2.5: The calculated energy landscape for GaV₄Se₈ versus tetrahedral distortion at (a) $U_{eff} = 0.9$ eV and (b) $U_{eff} = 3$ eV. The arrows on the tetrahedra are representative magnetic structures for each parabola and the colors of the atoms represent their structural equivalence. The colors of the parabolas indicate the net moment for each structure. Increasing values of U destabilize configurations with low net moments relative to high net moment configurations, as expected due to increasing localization of electrons on the V atoms.

Table 2.1: Comparison of PBE and ACFDT-RPA energies for different magnetic and structural configurations. ΔE is referenced to the lowest energy in the sequence of calculations.

state	exchange (eV)	correlation (eV)	total (eV)	ΔE (meV atom ⁻¹)	total (eV)	ΔE (meV atom ⁻¹)
	ACFDT-RPA				PBE	
high (HFM)	-164.26	-173.86	-338.12	24.49	-76.41	0
elong. ferri (FI2)	-161.31	-176.98	-338.29	11.21	-76.25	12.99
comp. ferri (FI1)	-161.07	-177.31	-338.38	4.18	-76.24	13.56
low (LFM)	-158.05	-180.38	-338.44	0	-76.10	23.97

ground state, the Jahn-Teller distortion occurs in the opposite direction (compressing rather than elongating along the $\langle 111 \rangle$ axis) to what is observed in experiment, and the net moment is $8 \mu_B/V_4$, which is far higher than the experimentally observed value. Additionally, the increase of U_{eff} destabilizes other magnetic configurations relative to the high moment configuration, presumably since these other configurations have lower moments, indicating the spins are more delocalized across the cluster. Therefore, PBE+ U_{eff} does not adequately capture the behavior of this cluster compound. We speculate that the reason for the failure of the Hubbard U correction is that the true electronic configuration of the V₄ cluster is best described by a molecular orbital picture, with the low-spin ferromagnetic state controlled by $d-d$ hopping rather than conventional double exchange. Following the description given by Streltsov and Khomskii,[51] this mechanism requires the redistribution of electrons away from localized d-orbitals, and into molecular orbitals formed by covalent metal-metal bonds. The addition of an on-site Hubbard U suppresses this redistribution and thus leads to worse results than pure PBE.

A more sophisticated approach to account for electron correlations is ACFDT-RPA,[38] which enabled total energy calculations using exact exchange energies from Hartree-Fock with correlation corrections. This method has been successfully employed to obtain the correct experimental ground state in other materials with competing ground

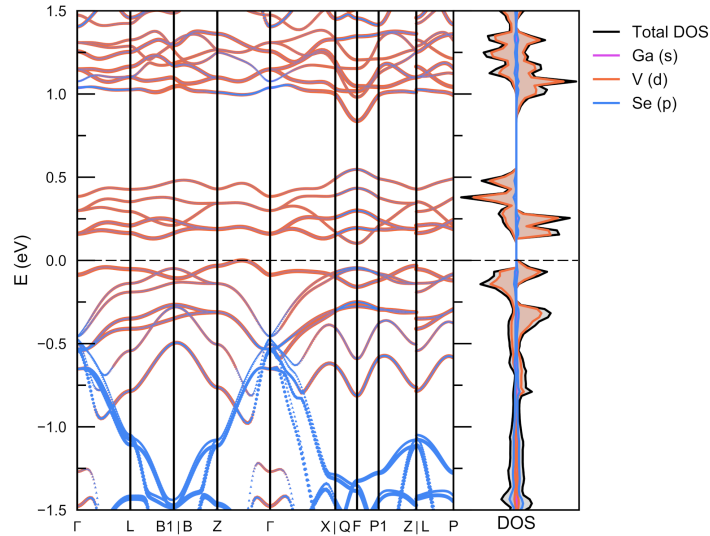


Figure 2.6: Spin-polarized band structure and densities of state from PBE calculations for what is established by ACFDT-RPA as the ground state, with a low net magnetic moment, ferromagnetic distribution of moment across a cluster, and an elongative Jahn-Teller distortion. The structural and magnetic energetics of this calculation correspond to the LFM minimum in Fig. 2.4.

states, including correlated magnetic materials.[39, 40] The Kohn-Sham orbitals from the PBE ($U = 0$ eV) low moment ferromagnetic (LFM) and ferrimagnetic (FI1 and FI2) minima along with the high moment (HFM) PBE ground state were selected as a starting point for ACFDT-RPA calculations. Table 2.1 shows a comparison of the ACFDT-RPA and PBE total energies for the four magnetic configurations (called LFM, FI1, FI2, and HFM respectively), as well as a breakdown into exchange and correlation energies for the ACFDT-RPA calculations. ACFDT-RPA stabilizes the LFM configuration, which has a net moment, crystal structure, and band gap similar that are close to the experimental values. As seen in Table 2.1, the HFM configuration is significantly more stable for the exchange energy, but correlation stabilizes the LFM configuration. The inability of PBE, even with a Hubbard U correction, to find the correct ground state is due to inadequate treatment of correlation energies in materials where the electronic structure is more adequately described with molecular orbitals rather than atomic orbitals.

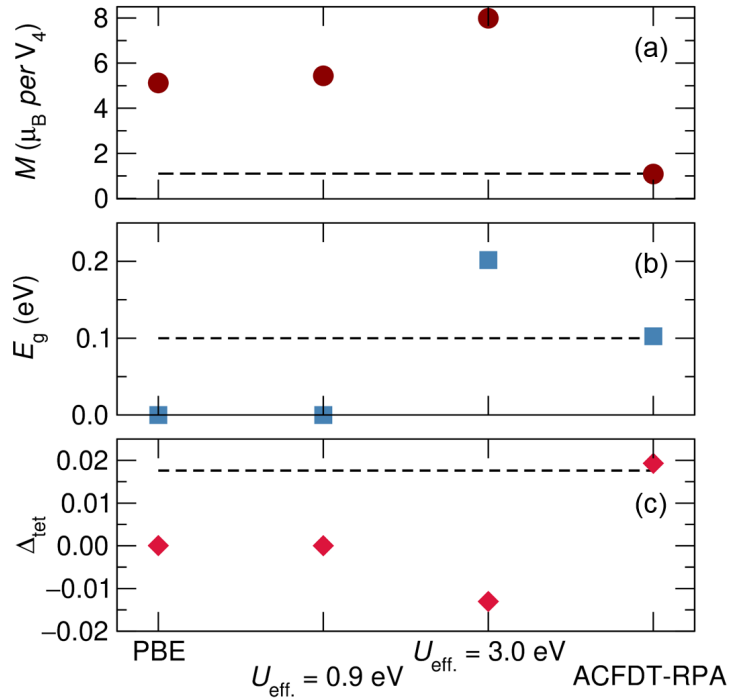


Figure 2.7: Ground state net magnetic moment (a), band gap (b), and tetrahedral distortion (c) for DFT calculations performed with varying levels of electron correlation corrections. The ground state established by ACFDT-RPA shows the greatest agreement with the experimental values (shown as dashed lines) for the magnetic, electronic, and crystal structure properties as compared to the ground states from PBE and PBE+ U_{eff} .

Since ACFDT-RPA establishes the lowest-energy state as the one corresponding to a low-moment, ferromagnetic distribution of moment across a cluster with an elongative Jahn-Teller structure, the corresponding spin-polarized PBE band structure and densities of state are displayed in Fig. 2.6. A gap close to 0.1 eV is seen, which is similar to what has been reported from the low-temperature hopping conductivity measurements.[31] The valence and conduction states have largely V d-orbital character, and the molecular nature of the lacunar spinel crystal structure ensures relatively narrow dispersion of the bands.

Figure 2.7 highlights the effectiveness of the ACFDT-RPA approach to modeling electron correlation effects compared with traditional PBE and PBE with U_{eff} approaches.

Particularly, ACFDT-RPA succeeds in reproducing experimentally observed magnetic and electronic properties as well as crystal structure distortion. The ground state from the ACFDT-RPA method is the only one which has an elongative Jahn-Teller distortion (shown as a positive value of Δ_{tet}) and a net magnetic moment close to the $1 \mu_B$ per V₄ expected from group theory and verified in experiment.

2.4 Conclusion

In GaV₄Se₈, the magnetic behavior is described by a hierarchy of magnetic interactions: the size of the atomic moments, the nature of intra-cluster and inter-cluster interactions, and additionally, the coupling between structural distortions and magnetic configurations. While the inter-cluster magnetic interactions have been probed experimentally, [16, 30, 31] intra-cluster interactions are harder to resolve. In a system where magnetism and crystal structure are strongly coupled, group theory can be a powerful tool to systematically explore the energy landscape. In combination with DFT, group theory allows us to consistently elucidate the couplings between structural and magnetic degrees of freedom in this system. Only certain magnetic configurations can support a Jahn-Teller distortion in GaV₄Se₈, and different configurations stabilize different distortions of the crystal structure, indicating strong magnetostructural coupling. This relationship, in addition to the crystal anisotropy from the polar space group, suggests that the application of strain will allow for the manipulation of magnetism in GaV₄Se₈. Additionally, in compounds with clusters of atoms, magnetism and electron correlation effects must be carefully considered. In such systems, more sophisticated approaches than DFT+*U*, such as ACFDT-RPA, may be required to obtain the correct energy landscape.

Chapter 3

Structural evolution and skyrmionic phase diagram of the lacunar spinel

GaMo_4Se_8

In the AB_4Q_8 lacunar spinels, the electronic structure is described on the basis of inter- and intra-cluster interactions of tetrahedral B_4 clusters, and tuning these can lead to myriad fascinating electronic and magnetic ground states. In this work, we employ magnetic measurements, synchrotron X-ray and neutron scattering, and first-principles electronic structure calculations to examine the coupling between structural and magnetic phase evolution in GaMo_4Se_8 , including the emergence of a skyrmionic regime in the magnetic phase diagram. We show that the competition between two distinct Jahn-Teller distortions of the room temperature cubic $F\bar{4}3m$ structure leads to the co-existence of the ground state $R\bar{3}m$ phase and a metastable $Imm2$ phase. The magnetic

The contents of this chapter have substantially appeared in Reference [52]. Reproduced with permission from: E. C. Schueller, D. A. Kitchev, J. L. Zuo, J. D. Bocarsly, J. A. Cooley, A. Van der Ven, S. D. Wilson and R. Seshadri, Structural Evolution and Skyrmionic Phase Diagram of the Lacunar Spinel GaMo_4Se_8 , *Phys. Rev. Materials* 4 (2020) 064402. Copyright 2020 American Physical Society

properties of these two phases are computationally shown to be very different, with the *Imm2* phase exhibiting uniaxial ferromagnetism and the *R3m* phase hosting a complex magnetic phase diagram including equilibrium Néel-type skyrmions stable from nearly $T = 28$ K down to $T = 2$ K, the lowest measured temperature. The large change in magnetic behavior induced by a small structural distortion reveals that GaMo₄Se₈ is an exciting candidate material for tuning unconventional magnetic properties *via* mechanical means.

3.1 Introduction

In recent years, there has been an increasing recognition that in some transition metal compounds, metal–metal bonding can often interact with electron correlation resulting in unconventional magnetic and electronic behavior, as well as unusually strong coupling between magnetic, electronic, and structural degrees of freedom [9, 29, 51, 53]. An important class of materials where this becomes evident are the lacunar spinels, which are characterized by tetrahedral clusters of transition metal atoms [54]. Two members of the lacunar spinel family, GaV₄S₈ and GaV₄Se₈, have garnered significant attention in recent years as multiferroic materials as well as Néel-type skyrmion hosts [15, 16, 30]. At low temperatures, these materials crystallize in the polar *R3m* space group [35] and support complex magnetic phase diagrams with an ordered moment of $1 \mu_B/V_4$ cluster. The related Mo-containing compounds, GaMo₄S₈ and GaMo₄Se₈, have been less studied, although they are reported to have a similar low temperature crystal structure, but with a compressive rather than elongative distortion along the cubic [111] direction [35, 55, 56].

Bulk magnetic measurements have revealed similar metamagnetic behavior be-

tween the Mo and the V-containing compounds [57, 58], while computational analysis of lacunar spinel ferromagnets suggests that all materials with this structure type are likely to host skyrmions across wide temperature ranges [59]. However, because Mo is a heavier element than V, the Mo-based compounds exhibit increased spin-orbit coupling, leading to more pronounced magnetic anomalies over greater regions of magnetic field and temperature. Additionally, spin-orbit coupling can affect the electronic properties through splitting of degenerate molecular orbitals, as seen in GaTa₄Se₈ [60]. A recent report on GaMo₄S₈ indicates that this material harbors complex modulated magnetic phases and that the increased spin-orbit coupling in the material leads to unusual “waving” effects on the magnetic ordering vectors [61].

In this work, we perform a detailed theoretical and experimental study of GaMo₄Se₈ in order to characterize the coupling between the crystal structure evolution and magnetic properties. We discover that at the structural phase transition, GaMo₄Se₈ can transform into two polar space groups, the reported rhombohedral $R\bar{3}m$ phase, which is the ground state, and an orthorhombic $Imm2$ phase, which is metastable. On the basis of computational and experimental data, we show that the $R\bar{3}m$ phase of GaMo₄Se₈ hosts a rich magnetic phase diagram with long wavelength magnetic order, including cycloids and Néel-type skyrmions, with periodicities on the order of 16 nm. In contrast, the competing $Imm2$ phase is suggested from first-principles calculations to be a strongly uniaxial ferromagnet. The dramatic change in magnetic behavior associated with a subtle change in crystal structure highlights the strong coupling between crystal structure and magnetism in GaMo₄Se₈, and suggests an avenue for tuning skyrmion and other exotic magnetic phases *via* strain.

3.2 Methods

3.2.1 Computational Methods

All electronic structure calculations were performed using the Vienna Ab-Initio Simulation Package (VASP) [43] with projector-augmented-wave pseudopotentials [44, 45] within the Perdew–Burke–Ernzerhof generalized gradient approximation [46]. We do not employ an atom-centered Hubbard– U correction as our previous analysis of the related GaV₄Se₈ system showed that this leads to an incorrect high-moment magnetic configuration by penalizing metal–metal bonding [29]. Structural distortions from the high temperature cubic structure to the low temperature orthorhombic and rhombohedral structures were generated using ISODISTORT [47]. Structural stability calculations used a Gamma-centered k -point grid of $8 \times 8 \times 8$ and an energy cutoff of 500 eV with a collinear magnetic configuration of $1 \mu_B/\text{Mo}_4$. Computational results were parsed and visualized with the python package pymatgen [27]. Noncollinear magnetic calculations accounting for spin–orbit coupling followed the methodology described by Kitchaev *et al.* [59]. All calculations were performed statically, on the basis of the experimentally determined crystal structures, and converged to 10^{-6} eV in total energy. To reduce noise associated with k -point discretization error, all spin-configuration energies were referenced to the energy of a c -axis ferromagnet computed within the same supercell. Noncollinear magnetic configurations were initialized by evenly distributing the magnetic moment of each Mo₄ tetrahedron on the four Mo atoms, i.e. as a locally ferromagnetic configuration of $0.25 \mu_B$ per Mo. The magnetic moment of each tetrahedron was then obtained from the DFT data by summing the individual magnetic moments projected onto the four Mo atoms.

The magnetic cluster expansion Hamiltonian [59, 62–64] used to construct the

magnetic phase diagram was derived by considering single-spin and nearest-neighbor pair interactions, as shown in Supplementary Figure S4 [65]. The interaction strengths were parametrized on the basis of collinear and spin-wave enumerations up to a supercell size of 4, as well as several sets of spin configurations iteratively generated to independently constrain the terms in the Hamiltonian.[66] Note that due to the very small energy scale of magnetocrystalline anisotropy, we fit the single-site anisotropy coefficients independently of the pair interactions, by fitting to the energy of rotating the ground-state collinear spin configurations within the primitive cell of the structure, so as to eliminate all noise arising from changes in the k -point grid [59]. The resulting parametrization leads to an error below $5 \mu\text{eV}/\text{Mo}_4$ for the magnetocrystalline anisotropy, and below $1 \text{ meV}/\text{Mo}_4$ across all non-collinear spin configurations, as shown in Supplementary Figure S5 [65]. The full Hamiltonians and fitted interaction parameters for the $R3m$ and $Imm2$ phases are given in Supplementary Tables 1 and 2 [65].

3.2.2 Experimental Methods

GaMo_4Se_8 powder was obtained by reaction of Ga pieces and ground Mo and Se powders with an approximately 50% excess of elemental Ga. The elements were reacted in an evacuated fused silica tube in 1 g batches with a heating ramp rate of $8^\circ \text{C}/\text{min}$ to 1010°C , held for 20 hours, and quenched [67].

High resolution synchrotron powder X-ray diffraction was performed at the Advanced Photon Source at Argonne National Laboratory at the 11-BM beamline. Approximately 30 mg of powder was loaded into a kapton capillary and placed into a cryostat. Temperature-dependent scans with a 10 minute exposure time were taken from $T = 10 \text{ K}$ to $T = 250 \text{ K}$. Rietveld refinements were performed using the Topas analysis

package [68]. Low-temperature structure solution was performed by first fitting the reported rhombohedral structure and then indexing the remaining structural peaks using the EXPO2014 software. The symmetry of the unit cell generated by EXPO was compared to various subgroups of the high temperature $F\bar{4}3m$ structure using the ISODISTORT software package [47]. A structure for the corresponding orthorhombic $Imm2$ space group was generated using ISODISTORT and Rietveld refinements of both the rhombohedral and orthorhombic phases were performed using TOPAS Academic [68]. Due to hkl -dependent strain, the Stephens peak shape was used in conjunction with Gaussian size broadening to fit the highly anisotropic peak shapes. Crystal structures were visualized using the VESTA software suite [42].

Small angle neutron scattering measurements were performed at the National Institute of Standards and Technology (NIST) NG-7 neutron beamline. Approximately 100 mg of powder was cold-pressed into a 5 mm pellet and placed into a cryostat. Exposures were taken over 8 h durations at various applied magnetic fields with the field applied parallel to the neutron beam. Three scans were taken below the magnetic ordering temperature and a 3 h background scan was performed with no applied field above the magnetic ordering temperature. The data integration and background subtraction was performed in the IGOR Pro software [69].

Bulk magnetic measurements were performed on a Quantum Design MPMS 3 SQUID Vibrating Sample Magnetometer, with approximately 30 mg of powder loaded into a plastic container and mounted in a brass holder. DC magnetization *vs.* field scans were performed on increasing field and AC susceptibility *vs.* field measurements were performed on decreasing field. For magnetoentropic mapping measurements, temperature-dependent magnetization measurements from 2 K to 40 K were performed with applied magnetic fields varying from 0 Oe to 4000 Oe in increments of 75 Oe. Derivatives and

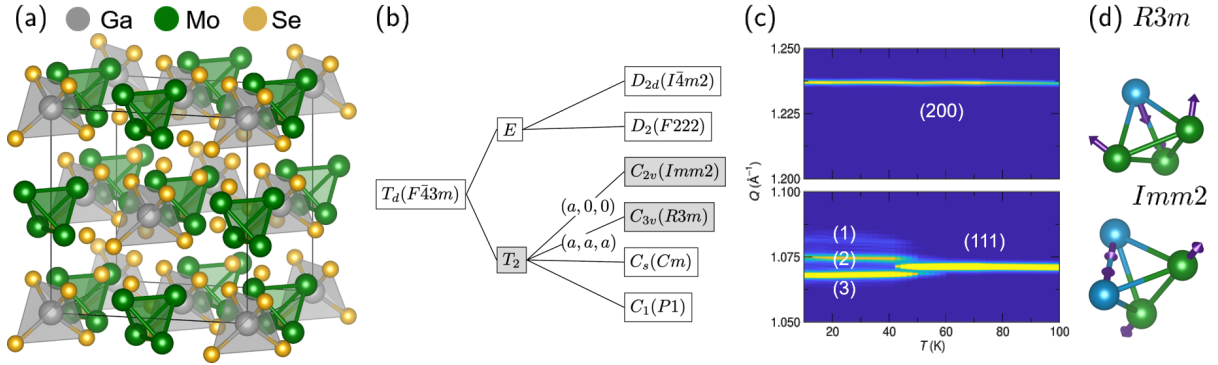


Figure 3.1: (a) The cubic $F\bar{4}3m$ crystal structure of GaMo_4Se_8 , characterized by tetrahedral clusters of Mo atoms. (b) All subgroups of $F\bar{4}3m$ which keep the primitive unit cell volume the same. $R3m$ and $Imm2$ both follow the T_2 irrep but through different order parameter directions. (c) The evolution of peaks upon cooling in synchrotron XRD data. At 50 K the (111) cubic peak splits into 3 while the (200) cubic peak stays undistorted. Because the middle peak of the (111) split shifts relative to the peak in the cubic phase while the (200) peak does not shift, it is not possible to explain the low temperature structure by a combination of the cubic phase and a single low temperature phase. (d) The distortion of the Mo_4 tetrahedron as it goes into the $R3m$ and $Imm2$ space groups. Both are polar, but the $Imm2$ cluster has lower symmetry, with three unique bond lengths, compared to two in the $R3m$ cluster.

ΔS_m calculations were performed using python code available from Bocarsly *et al.* [3].

3.3 Results

The room temperature crystal structure of GaMo_4Se_8 is highlighted in Figure 3.1(a), characterized by tetrahedral clusters of Mo atoms which behave like molecular units with a spin of $1 \mu_B$ per Mo_4 cluster. Through experimental and computational techniques, we find that GaMo_4Se_8 follows qualitatively similar behavior to GaV_4Se_8 , with complex magnetic order arising from a Jahn–Teller distortion of the high–temperature $F\bar{4}3m$ structure. However, in addition to the $R3m$ ground state, GaMo_4Se_8 forms a competing metastable $Imm2$ phase, defined by an orthorhombic Jahn–Teller distortion and distinctly different magnetic properties. We first characterize the formation

and coexistence of these two structures, and then establish how the character of the low-temperature distortion controls the magnetic phase diagram of each phase.

Figure 3.1(c) shows high-resolution synchrotron powder diffraction data as a function of temperature. At $T = 50$ K, the (111) cubic peak splits into 3 peaks, with the two outer peaks corresponding to an $R3m$ distortion. Previous X-ray diffraction studies of the structural phase transition of GaMo₄Se₈ have rationalized the presence of extra peaks below the transition temperature ($T = 51$ K) as the coexistence of the high temperature cubic $F\bar{4}3m$ phase and the rhombohedral $R3m$ phase [55]. However, with high-resolution measurements employed here, we find that the low-temperature data cannot be fit by a combination of the $R3m$ phase and the $F\bar{4}3m$ phase. The middle peak shown in the lower panel of Figure 3.1(c), which was previously assumed to be a continuation of the cubic ($F\bar{4}3m$) phase, shifts significantly at the phase transition, while the higher Q peak [cubic (200)] shown in the top panel does not split or shift at the phase transition. Because there is only one lattice parameter in the cubic phase, it cannot support a shift of one peak but not another, meaning that there must be another explanation for the additional peaks.

We performed a search for a lower symmetry subgroup of $R3m$ (such as a monoclinic $C2/m$ phase) that could explain the additional peaks, but found none that did not add extraneous peaks, not present in the data. We indexed the peaks that could not be explained by the $R3m$ unit cell and found they corresponded to an orthorhombic, polar $Imm2$ phase. $Imm2$, while a subgroup of the parent $F\bar{4}3m$ structure, is not a subgroup of the $R3m$ space group. The transition pathways from the $F\bar{4}3m$ phase to the $R3m$ and $Imm2$ phases are associated with two different order parameter directions, but with the same irreducible representation (T_2) as shown in Figure 3.1(c), indicating the two subgroups are symmetrically similar. This similarity can be seen in the diffrac-

tion data; both low temperature space groups have diffraction patterns characterized by splitting of the same cubic peaks, but the new peaks are distinct in number and position between the two phases. The difference between the two structures is most obvious in the distortion of the Mo_4 tetrahedron through the phase transition, indicated by the arrows in Figure 3.1(d), which leads to 2 sets of Mo–Mo bond lengths in the $R3m$ phase and 3 sets in the $Imm2$ phase.

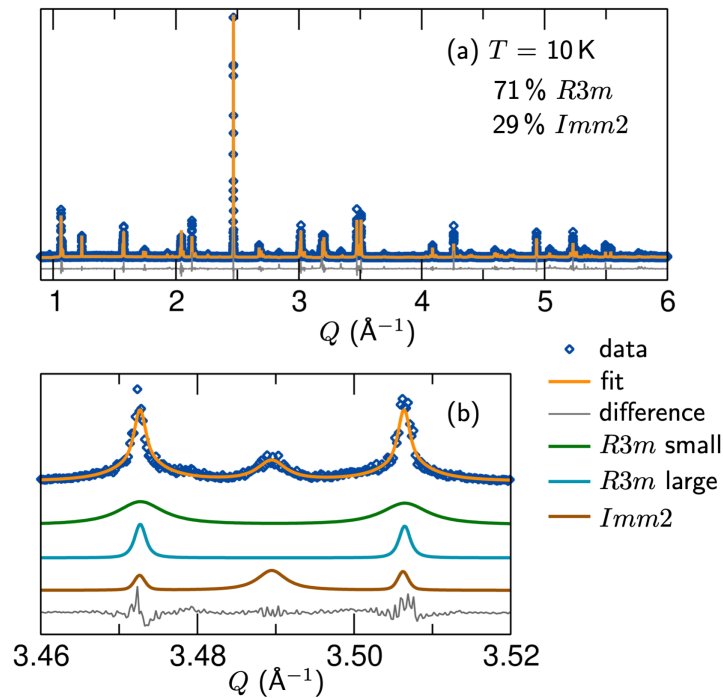


Figure 3.2: (a) At 10 K, there is about 70% of the rhombohedral phase and 30% of the orthorhombic phase. (b) The complex peak shapes can be fit with two $R3m$ phases with different particle sizes, and an $Imm2$ phase with hkl -dependent strain broadening.

It is clear from the diffraction data that the $R3m$ and $Imm2$ phases form simultaneously and coexist in the powder. However, the structures are noticeably strained, as evidenced by the broad line shapes, and have a large amount of peak overlap due to their similarity, which introduces uncertainty in the determination of relative weight percentages of the two phases. As seen in Figure 3.2(a), our best fit to the data at

$T = 10$ K yields about 30% of the orthorhombic phase and 70% of the rhombohedral phase. In order to fit the unusual peak shapes, we use two phases for the $R3m$ structure, one with small particles (strong effects of size broadening) and one with large particles, both with strain effects. The $Imm2$ phase is fit with hkl -dependent strain broadening using the Stephens peak-shape. This combination of phases to describe a single peak is shown in Figure 3.2(b). At $T = 50$ K, the diffraction data is best fit by a combination of the cubic phase and both the $R3m$ and $Imm2$ phases, indicating both phases form simultaneously at the phase transition temperature and there is no phase region with only one of the two low temperature structures. A similar phase transition from a high symmetry structure into two subgroups has been reported in the oxide spinels MgCr_2O_4 and ZnCr_2O_4 and was attributed to internal strain creating a metastable and stable phase [70].

To probe the energy landscape for these two phases, we turn to density functional theory (DFT) calculations. We find that while the $R3m$ phase is the ground state structure, its formation may be kinetically suppressed relative to the $Imm2$ phase. Using ISODISTORT, we generated distorted structures along the path from the $F\bar{4}3m$ phase to the $R3m$ phase and the $Imm2$ phase. These calculations show that the orthorhombic structure is less stable than the rhombohedral structure by about 20 meV/ Mo_4 cluster, as shown in Figure 3.3(a). However, the transition pathway leading to the $R3m$ phase proceeds over an energy barrier, while the formation of the $Imm2$ phase has a smaller barrier. Furthermore, we observe experimentally that the percentage of the $R3m$ phase increases with decreasing temperature, as can be seen in Figure 3.3(b). Thus, both computation and experiments indicate that the $R3m$ arrangement is the likely ground state. Nonetheless, it is possible that due to the low temperature of the phase transition ($T = 51$ K), the material could get trapped in the orthorhombic structure and lack

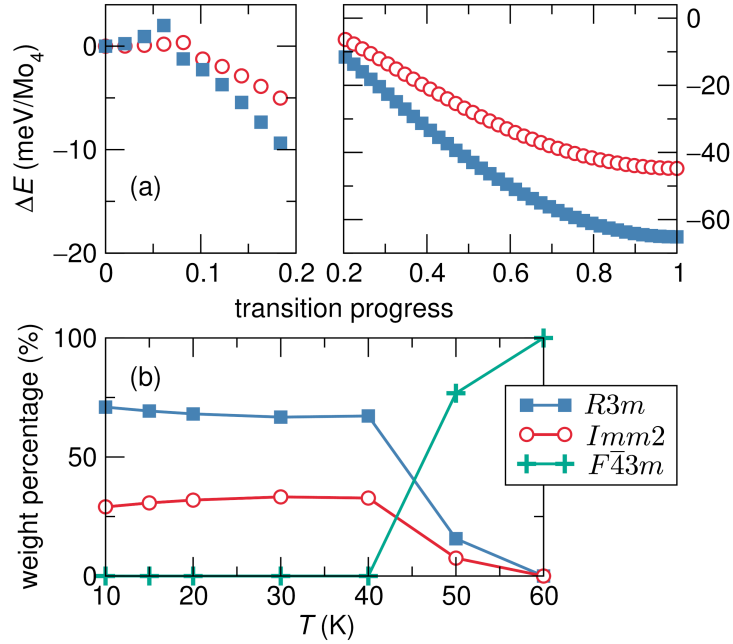


Figure 3.3: (a) DFT energies along the transition pathways from the cubic phase to the rhombohedral and orthorhombic phases. The $R3m$ structure has lower energy, making it the ground state structure, but it has a higher formation energy barrier, highlighted in the left panel. The energy difference is 20 meV/Mo₄ cluster. (b) The phase evolution of GaMo_4Se_8 . Upon cooling, the percentage of the $R3m$ phase slightly increases, indicating it is likely the ground state crystal structure.

the energy to convert to the rhombohedral structure. It is also likely that strain effects impact the energy landscape of the two phases and could stabilize the $Imm2$ phase.

Analogous to other lacunar spinels, the magnetic behavior of GaMo_4Se_8 is closely tied to its crystal structure. Temperature-dependent magnetization data reveals largely ferromagnetic ordering with an ordering temperature of approximately $T = 27.5$ K, in agreement with previous reports [58]. GaMo_4Se_8 has a saturation magnetization of close to $1 \mu_B/\text{Mo}_4$ cluster, as shown in Figure 3.4(a), in agreement with literature [58] and molecular orbital theory. However, field-dependent magnetization measurements show the presence of multiple magnetic phase transitions at all temperatures below the ordering temperature down to $T = 2$ K, as shown in Figure 3.4(b). Resolving the nature of these phase transitions is complicated by the fact that by analogy to V-based lacunar

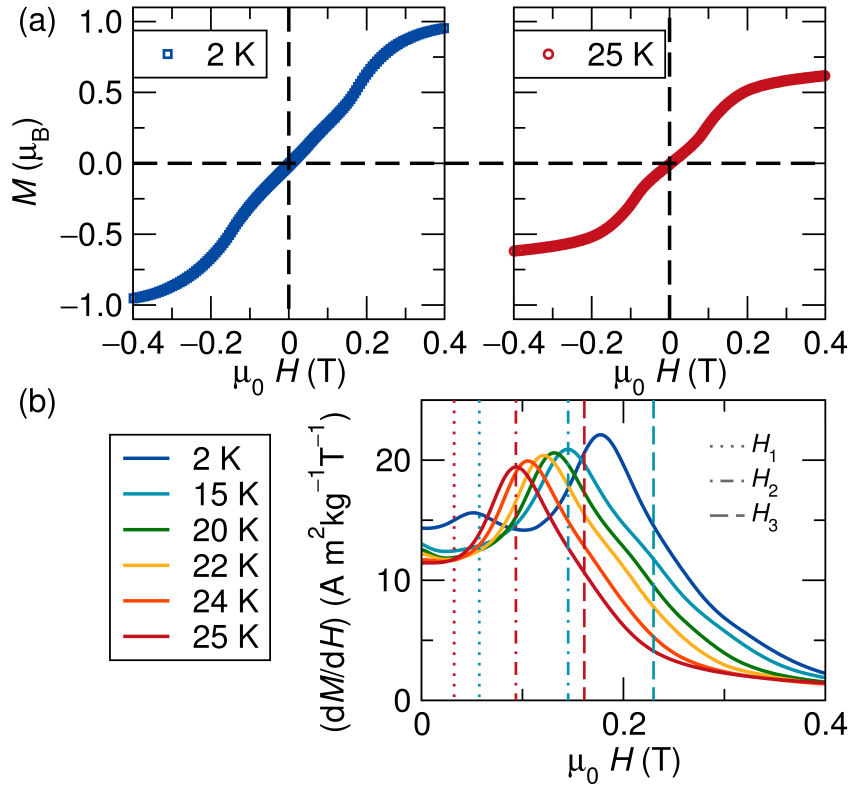


Figure 3.4: (a) At $T = 2\text{ K}$, the saturation magnetization is $1 \mu_B/\text{Mo}_4$ cluster, in agreement with DFT and molecular orbital theory. Multiple magnetic phase transitions are evident in field-dependent magnetization measurements. (b) Phase transitions are shown more clearly in the derivative of magnetization with respect to field. These transitions persist down to $T = 2\text{ K}$, the lowest temperature measured.

spinels, it is likely that the magnetic phase diagram of GaMo_4Se_8 depends strongly on the direction at which the magnetic field is oriented relative to the polar axis of the crystal. As all of our data is collected on a powder sample under uniaxial applied magnetic field, different grains can have different magnetic phases, complicating the interpretation of bulk magnetization data. Nonetheless, by combining a variety of experimental and computational signatures of magnetic phase stability, we are able to understand the observed magnetic phase transitions and confirm the existence of a skyrmion phase.

A recently presented experimental technique for resolving magnetic phase diagrams

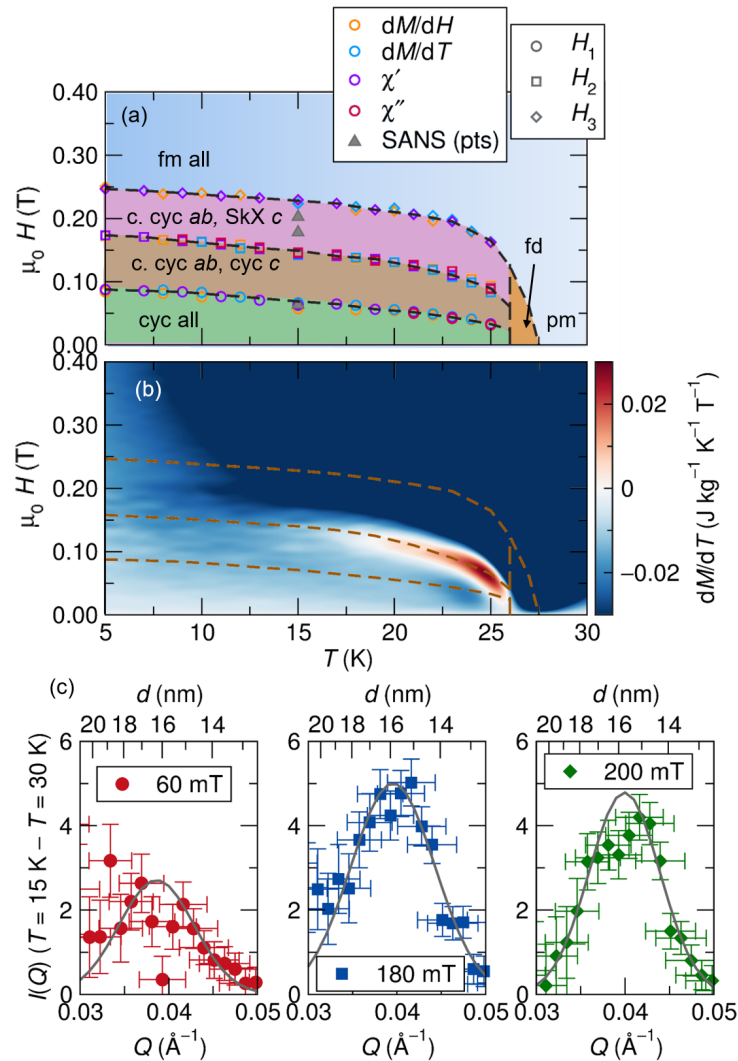


Figure 3.5: (a) Using multiple bulk magnetization measurement techniques, we suggest a field vs. temperature phase diagram for GaMo_4Se_8 . Based on theoretical calculations and the phase diagrams for the related V -compounds, we posit that the low field transition is a transition from cycloidal into canted cycloid or ferromagnetic ordering in grains (denoted *ab*) where the field is mostly perpendicular to the polar axis. Upon increasing field, grains (denoted *c*) where the field is mostly aligned with the polar axis transition into a skyrmion phase and then become field polarized. Near the Curie temperature there is a fluctuation-disordered (fd) phase. (b) The transition into the proposed skyrmion phase in *c*-oriented grains is associated with an increase in magnetic entropy, shown as a red feature near the Curie temperature that broadens upon cooling. (c) SANS data shows the presence of approximately 16 nm magnetic periodicity at multiple applied fields at $T = 15$ K. The red points are in the cycloidal phase and the blue and green are in the skyrmion phase. The gray lines are Gaussian fits to guide the eye.

is magnetoentropic mapping. This technique [3], relies on the Maxwell relation that $(\partial M/\partial T)_H = (\partial S/\partial H)_T$ to identify field driven magnetic phase transitions that are associated with a change in magnetic entropy. In particular, skyrmions form as a high entropy phase, so that the formation of skyrmions is typically associated with a positive entropy anomaly [3, 71, 72]. On a map of $(\partial S/\partial H)_T$, shown in Figure 3.5(b), generated from temperature-dependent-magnetization measurements at various applied fields, shown in Supplementary Figure S3 [65], we can see a red positive entropy anomaly that starts near the Curie temperature and broadens upon cooling. Overlaying this data with peaks in DC susceptibilities $(\partial M/\partial T)$, shown in Supplementary Figure S1 [65], and $(\partial M/\partial H)$ vs. H curves, shown in Figure 3.4(b), as well as AC susceptibility measurements, shown in Supplementary Figure S2 [65], we observe these signatures are in agreement with the transitions from the entropy map. From these measurements we can generate the phase diagram shown in Figure 3.5(a) which suggests that the high-entropy region corresponds to a skyrmion phase with behavior similar to that seen in GaV₄Se₈. The vertical portion of the entropy anomaly near the Curie temperature has been observed in other skyrmion host materials [3] and has been posited to be a Brazovskii transition into a short-range-ordered or fluctuation-disordered (fd) magnetic phase.

Susceptibility data reveals two additional transitions not visible in the magnetoentropic map, indicating the presence of phase transitions not associated with a large change in magnetic entropy. To unambiguously resolve these phase transitions, as well as to disentangle the contributions of the $R3m$ and $Imm2$ phases in the powder, we turn to computational modeling. Our computational analysis relies on a magnetic cluster expansion Hamiltonian parameterized using density functional theory (DFT), which has been recently demonstrated to yield reliable magnetic phase diagrams for the lacu-

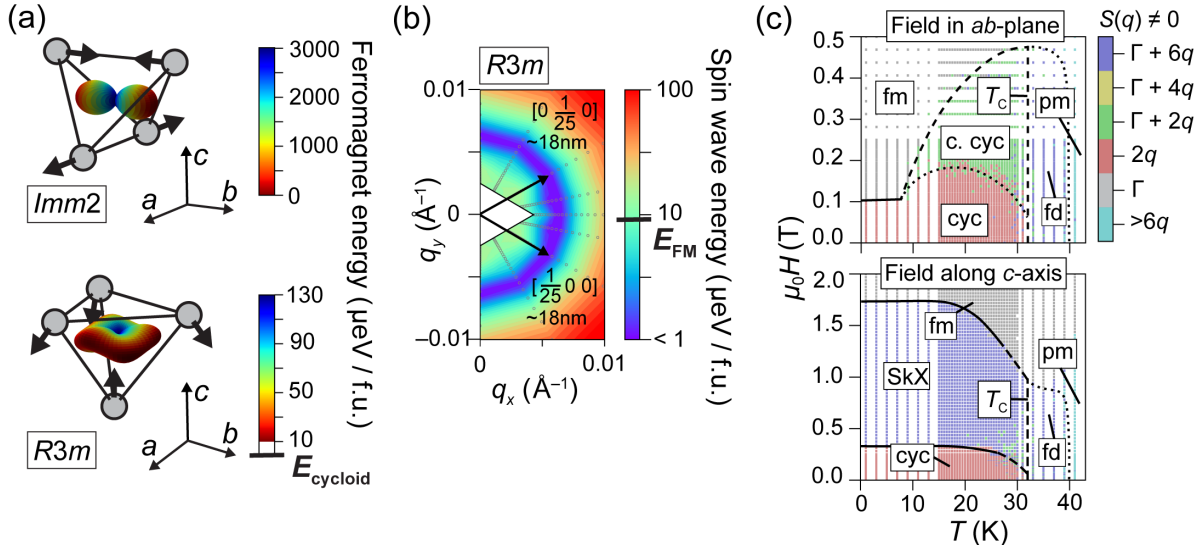


Figure 3.6: (a) Computed magnetocrystalline anisotropy in the $Imm2$ and $R3m$ phases of GaMo_4Se_8 . Grey circles denote Mo atoms, and black arrows illustrate the direction of the Jahn-Teller distortion required to form each phase. The plotted color and distance from the tetrahedron center denote the energy of a ferromagnetic spin configuration oriented along the corresponding crystallographic direction. (b) Energy of spin wave configurations in the (ab) -plane of the $R3m$ phase as a function of their q -vector, revealing the family of cycloid ground states with a predicted wavelength of $\approx 18\text{ nm}$. (c) Computed magnetic phase diagram of the $R3m$ phase for fields oriented along the c -axis or the (ab) -plane. Color denotes the magnetic structure factor $S(q)$, while phase boundaries are drawn to best capture discontinuities in structure factor, susceptibility, heat capacity, and magnetization. Phase labels correspond to cycloid (cyc), canted cycloid (c. cyc), skyrmion (SkX), ferromagnet (fm), fluctuation disordered (fd), and paramagnet (pm) regions. Solid and dashed lines denote first and second order phase transitions respectively, while dotted lines denote a transition that is continuous within the resolution of our data. Figure c.o. Daniil Kitcheaev.

nar spinels [59]. We are thus able to independently resolve the anisotropic magnetic phase diagrams expected in the $R3m$ and $Imm2$ phases and rationalize the observed magnetic behavior of the biphasic powder.

First, we demonstrate that the zero-field, low-temperature ground state magnetic configuration of the $R3m$ phase is a cycloid with a predicted wavelength of 18 nm, while the $Imm2$ phase is a uniaxial ferromagnet. Figure 3.6(a) maps out the energy of the ferromagnetic state in both phases relative to the energy of the ground state

	A (10 ⁻¹³ J/m)	D_{xy} (10 ⁻⁴ J/m ²)	D_{yx}	K_u (10 ⁴ J/m ³)
<i>R3m</i>	3.48	-2.35	2.35	7.34
<i>Imm2</i>	4.15	-5.00	-0.682	-182

Table 3.1: Effective micromagnetic interaction parameters in the low-temperature limit for the *R3m* and *Imm2* phases of GaMo₄Se₈. See main text and Supplementary Figure S4 [65] for a definition of variables and coordinate systems.

magnetic phase. The *Imm2* phase strongly favors magnetization along the *b*-axis, parallel to the shortest Mo–Mo bond. The *R3m* phase exhibits a predominantly easy-plane anisotropy, normal to the compressive distortion of the Mo₄ tetrahedron, with a three-fold modulation favoring spin orientation towards the corners of the tetrahedron. While the Dzyaloshinskii–Moriya interaction (DMI) in the two phases is comparable in magnitude and favors cycloidal spin textures in the (*ab*)-planes [4], the large magnetocrystalline anisotropy of the *Imm2* phase suppresses any spin configuration deviating from the *b*-axis, forcing a ferromagnetic ground state. This behavior is in contrast to easy-axis skyrmion hosts such as GaV₄S₈, where the anisotropy is sufficiently weak to shift the skyrmion phase boundaries but not suppress them entirely [59]. In the *R3m* phase, the DMI overcomes the anisotropy energy and leads to the formation of equilibrium spin cycloids at the low energy wavevectors shown in Figure 3.6(b). The cycloids can form in any direction in the (*ab*)-plane, which is the plane perpendicular to the polar (*c*) axis of the *R3m* structure.

The low-temperature magnetic behavior of the *R3m* and *Imm2* phases can be summarized using a conventional micromagnetic free energy density functional with micromagnetic parameters given in Table 3.1, which is directly comparable to that of other skyrmion-host materials[15, 73]:

$$E = A \sum_{ij} m_{i,j}^2 + \sum_{ijkn} D_{kn} \varepsilon_{ijk} m_i m_{j,n} + K_u m_u^2$$

Here, m is a magnetization unit vector, A is the exchange stiffness, D_{kn} is the Dzyaloshinskii coupling, and K_u is the uniaxial anisotropy constant defined with respect to the c -axis of the $R3m$ phase, and the b -axis of the $Imm2$ phase. The indices $ijkn$ iterate over Cartesian directions (x, y, z) , and ε_{ijk} is the Levi-Civita symbol. The notation $m_{i,j}$ denotes a partial derivative $\partial m_i / \partial r_j$. The orientation of the $R3m$ and $Imm2$ crystals with respect to the Cartesian axes is given in Supplementary Figure S4 [65]. A detailed description of this functional can be found in the literature [4, 74].

Having established the low-temperature, zero-field magnetic behavior of the two phases comprising our GaMo₄Se₈ sample, we proceed to construct the full field vs. temperature phase diagram of the material. We focus on the $R3m$ phase, as shown in Figure 3.6(c), because the $Imm2$ phase remains a uniaxial ferromagnet at all fields within our experimental range and does not contribute to the observed phase transitions. For fields oriented along the (ab) -plane, the phase diagram is defined by a transition from the cycloidal ground state to a field-polarized ferromagnetic state near $\mu_0 H = 0.1$ T. Below $\approx T_C/3$, this phase transition is first order, while at higher temperatures it proceeds as a second order transition through a canted cycloid intermediate. When the field is oriented along the c -axis, the low-field cycloid undergoes a first-order transition into a skyrmion lattice phase at around $\mu_0 H = 0.3$ T, which appears to remain stable to very high fields, up to $\mu_0 H = 1.7$ T. Magnetic order persists up to $T_C = 32$ K, with a fluctuation-disordered Brazovskii region appearing immediately above T_C . While some quantitative discrepancies exist between this computational phase diagram and the experimental data, in particular in the range of fields for which skyrmions appear to be stable, the overall trends in phase behavior are informative for determining

which phase transitions are being observed in our powder data.

The trends in phase behavior observed in the computational model confirm that the the high-entropy region observed in the magnetoentropic map likely corresponds to a skyrmion phase in $R3m$ grains with the c -axis nearly parallel to the applied field. Furthermore, we propose that the low field transition seen in the susceptibility data is from a cycloidal to a ferromagnetic state in $R3m$ grains where the magnetic field is mostly aligned perpendicular to the polar axis. The high field transition is most likely a transition from the skyrmion lattice to a ferromagnetic state in $R3m$ grains in which the magnetic field is mostly aligned along the polar (c) axis. Finally, the $Imm2$ phase contributes a ferromagnetic background, with no additional magnetic phase transitions. The similar magnitude of the exchange energy between the $Imm2$ and $R3m$ phases, approximated as A in Table 3.1, suggests that their magnetic ordering temperatures should be quite similar, which explains why two magnetic ordering transitions are not seen in the experimental data.

To verify the presence of long-wavelength magnetic order in GaMo₄Se₈, we performed powder SANS measurements at 15 K in the regions we predict to correspond to cycloid and skyrmion stability. The points at which SANS data was taken are indicated on our proposed phase diagram in Figure 3.5(a) with triangle markers. Due to the small moment of $1 \mu_B/\text{Mo}_4$ cluster and different grains in different magnetic phases, the signal is quite low. Nonetheless, after subtracting background data taken at $T = 30$ K (above the Curie temperature), we see one to two peaks in the SANS signal at all applied fields, shown in Figure 3.5(c), corresponding to a real-space magnetic periodicity of around 16 nm, in acceptable agreement with our theoretical calculations for cycloid/skyrmion periodicity (18 nm).

3.4 Discussion

We have established that GaMo₄Se₈ undergoes a complex structural phase transition due to a relatively flat energy landscape in which multiple low temperature space groups have similar energies, as well as a competition between phases favored thermodynamically and kinetically. While the GaV₄(S/Se)₈ compounds exhibit only the $R\bar{3}m$ structure at low temperature, GaMo₄Se₈ undergoes a structural transition from the high temperature $F\bar{4}3m$ phase into two coexisting polar space groups, rhombohedral $R\bar{3}m$, which is the ground state, and orthorhombic $Imm2$, which is metastable. In the lacunar spinel family, GeV₄S₈ undergoes a Jahn-Teller distortion into an $Imm2$ structure, likely because it has one extra electron in the t_2 orbital relative to GaV₄S₈, stabilizing a different splitting of the t_2 orbital [75]. We speculate that in GaMo₄Se₈, the increased filling of the t_2 orbital relative to the V-compounds, along with enhanced spin-orbit coupling, creates an energy landscape with the $Imm2$ and $R\bar{3}m$ structures much closer in energy than in other members of the family.

The competition between the stable and metastable crystal structures of GaMo₄Se₈ could be used to tune the multiferroic properties of GaMo₄Se₈, for instance by straining the material in such a way to stabilize one of the crystal structures. Our computational studies shows that the slight differences between the $Imm2$ and $R\bar{3}m$ structures have a dramatic impact on the magnetic properties due to a large change in magnetocrystalline anisotropy. Thus, any strain which alters the relative stability of the two phases will in turn have a strong impact on magnetic behavior. Specifically, stabilization of the $Imm2$ phase leads to uniaxial ferromagnetism, while favoring the $R\bar{3}m$ phase leads to long-wavelength magnetic order with a cycloidal ground state and Néel-type skyrmions. The strong emergent magnetostructural coupling in GaMo₄Se₈ provides a route towards the mechanical control of exotic magnetism.

It is worth noting that extra diffraction peaks similar to those of the *Imm2* phase in GaMo₄Se₈ were also observed in the low temperature diffraction patterns of the sulfide equivalent, GaMo₄S₈ and attributed to coexistence of the cubic phase [56]. Thus, it is possible that GaMo₄S₈ could also have coexisting rhombohedral and orthorhombic low temperature structures, and exhibit similarly strong emergent magnetostructural coupling. Given the recent exciting magnetic discoveries in GaMo₄S₈[61], the discovery of an *Imm2* phase in GaMo₄Se₈ merits a re-examination of the crystal structure evolution of GaMo₄S₈ with synchrotron resolution.

Finally, we have shown that the *R3m* phase of GaMo₄Se₈ has a magnetic phase diagram with long-wavelength magnetic phases stable over a wide temperature and field range. GaMo₄Se₈ has a higher Curie temperature than the V-compounds or GaMo₄S₈ at $T_C = 27.5$ K, with cycloids and Néel-type skyrmions stable down to the lowest temperatures measured ($T = 2$ K). With a field applied along the polar axis, cycloids are stable from $\mu_0 H = 0$ T to around $\mu_0 H = 0.15$ T and skyrmions are stable up to $\mu_0 H = 0.25$ T at $T = 5$ K. SANS data show a magnetic periodicity of around 16 nm, in good agreement with our computational analysis (18 nm). Overall, the qualitative form of the phase diagram is in good agreement between our experimental results, computational analysis, and previous reports in the literature for materials of similar symmetry[59, 76–78]. However, there are deviations from experiment in the exact range of fields for which skyrmions are stable. The discrepancy in the cycloid to skyrmion transition is of a similar magnitude to the error in the Curie temperature and cycloid to in-plane ferromagnet transition, and is most likely a result of errors in the underlying DFT representation of GaMo₄Se₈ magnetism, as well as deviations in the g -factor from our assumed value of 2. The much larger discrepancy in the upper bound on skyrmion stability versus applied field is more likely a result of stray fields, which we neglect in our simulations.

Finally, while we do not observe the complexity in magnetic ordering vector reported in GaMo₄S₈ [61], this difference may be a consequence of the sensitivity of data we are able to obtain from a powder sample as compared to a single crystal.

3.5 Conclusion

A combined experimental and computational investigation of the low-temperature structural and magnetic phase behavior of the GaMo₄Se₈ lacunar spinel has been carried out. We show that this material undergoes a Jahn–Teller distortion at $T = 51$ K into two co-existing structures – a metastable $Imm2$ configuration and the ground state $R3m$ phase. These two phases both order magnetically at $T_C = 27.5$ K, but exhibit dramatically different magnetic behavior due to differences in their magnetocrystalline anisotropy. While the $Imm2$ phase is found from computation to be a uniaxial ferromagnet, the $R3m$ phase favors a 16 nm cycloid ground state, and a Néel–skyrmion lattice under applied field. We conclude that the coexistence of these two phases with dramatically different magnetic properties makes GaMo₄Se₈ a promising material for realizing mechanical control over exotic magnetism, as small energy differences separating the $Imm2$ and $R3m$ phases translate into a very large change in magnetic behavior.

Chapter 4

Structural Signatures of the Insulator-to-Metal Transition in $\text{BaCo}_{1-x}\text{Ni}_x\text{S}_2$

The solid solution $\text{BaCo}_{1-x}\text{Ni}_x\text{S}_2$ exhibits an insulator-to-metal transition close to $x = 0.21$. Questions of whether this transition is coupled with structural changes remain open. Here we follow the structural evolution as a function of the Ni content x using synchrotron powder X-ray diffraction and pair distribution function analyses, to reveal significant basal sulfide anion displacements occurring preferentially along the CoS_5 pyramidal edges comprising the edge-connected bond network in $\text{BaCo}_{1-x}\text{Ni}_x\text{S}_2$. These displacements decrease in magnitude as x increases and are nearly quenched in $x = 1$ BaNiS_2 . Density functional theory-based electronic structure calculations on $x = 0$ BaCoS_2 suggest that these displacements arise as a dynamic first-order Jahn-

At the time of publication, the contents of this chapter were submitted to *Phys.Rev.Materials* as E. C. Schueller, K. D. Miller, W. Zhang, J. L. Zuo, J. M. Rondinelli, S. D. Wilson and R. Seshadri, Structural Signatures of the Insulator-to-Metal Transition in $\text{BaCo}_{1-x}\text{Ni}_x\text{S}_2$.

Teller effect owing to partial occupancy of nominally degenerate Co^{2+} d_{xz} and d_{yz} orbitals, leading to local structural symmetry breaking in the xy -plane of the Co-rich phases. The Jahn-Teller instability is associated with opening of a band gap that is further strengthened by electronic correlation. The Jahn-Teller effect is reduced upon increased electron filling as $x \rightarrow 1$, indicating local structure and band filling cooperatively result in the observed insulator-to-metal transition.

4.1 Introduction

The solid solution between BaCoS_2 and BaNiS_2 displays a compositionally driven insulator-to-metal transition when approximately 21% of the Co is replaced with Ni [79, 80]. The metallic end member, BaNiS_2 , is a Pauli paramagnet with the tetragonal ($P4/nmm$) structure, exhibiting Ba layers alternating with layers of NiS_5 square pyramids [81]. BaNiS_2 has recently been reported to be a compensated semimetal with topological band crossings [19]. In the $P4/nmm$ space group, the NiS_5 square pyramids are distorted such that the apical Ni-S bond lengths are slightly longer than the basal Ni-S lengths. The insulating end member BaCoS_2 displays antiferromagnetic order just above room temperature with a high spin Co^{2+} configuration [82]. BaCoS_2 has been reported to be a charge-transfer insulator with strong electron correlations [18, 83]. In BaCoS_2 , there is a small monoclinic ($P2/c$) distortion to the compound in the plane of the layers, creating two unique bond lengths between the Co and the basal S [81]. However, unlike many known materials displaying insulator-to-metal transitions (for example, the dimerization of VO_2 [9, 10, 84, 85]), the electronic transition in $\text{BaCo}_{1-x}\text{Ni}_x\text{S}_2$ has not been related to changes in the average or local structure. The monoclinic-to-tetragonal transition occurs for $0 \leq x \leq 0.1$, while the electronic

transition does not occur until $x \approx 0.21$ [17, 81]. The insulator-to-metal transition is associated with the disappearance of magnetic order, although a small antiferromagnetic metal phase region has been reported [86]. This has led to speculation that the transition in $\text{BaCo}_{1-x}\text{Ni}_x\text{S}_2$ is purely electronic in origin [86, 87].

Here we study six compositions across the solid solution $\text{BaCo}_{1-x}\text{Ni}_x\text{S}_2$, corresponding to 3 insulating and 3 metallic phases, to understand the average and local structure evolution across the insulator-to-metal transition and the coupling with electronic and magnetic behavior. We employ high resolution synchrotron powder X-ray diffraction as well as X-ray pair distribution function data to probe both the average and local structure in each sample. Disordered local displacements from the average structure are observed, specifically on the basal S site, agreeing with previous reports of large atomic displacement parameters on that site in BaCoS_2 [81, 88]. Through reverse Monte Carlo (RMC) modeling of the average and local structure data, we find disordered basal S displacements along the edges of the square pyramids produce the best fit, and that the magnitude of the local displacements decreases significantly with Ni substitution.

An understanding of the origin of the local displacements on the basis of a first-order Jahn-Teller instability in BaCoS_2 (d^7) is obtained from density functional theory (DFT) calculations; the displacements appear to arise from an electronic degeneracy of the d_{xz} and d_{yz} orbitals that are fractionally occupied. These orbitals are fully occupied in BaNiS_2 (d^8), which explains the observed decrease in local distortions with increasing Ni. Although the average structure transition to $P2/c$ in BaCoS_2 slightly relieves the Jahn-Teller instability, calculations of the phonon dispersions indicate coherent soft mode instabilities in BaCoS_2 resulting in a $Pba2$ supercell with displacements of basal S atoms similar to those observed in the RMC modeling. These simulations suggest

that the room temperature structure of BaCoS_2 and the other insulating members in the solid solution series with Ni may be a disordered version of this orthorhombic structure, analogous to the dynamically disordered Jahn-Teller distortions across the insulator-to-metal transition in Ca-doped LaMnO_3 [12].

4.2 Methods

4.2.1 Computational Methods

First-principles spin-polarized density-functional theory (DFT) calculations on the BaCoS_2 end member were performed using the Vienna *Ab initio* Simulation Package (VASP) [43] with projector-augmented-wave pseudopotentials [44, 45] within the Perdew–Burke–Ernzerhof generalized gradient approximation (PBE) [46] for band structure calculations and the version revised for solids (PBEsol) [89] for structural calculations (such as phonon dispersions). For all calculations, we use a 600 eV plane wave cutoff and treat the core and valence electrons with the following electronic configurations: $5s^25p^66s^2$ (Ba), $3d^84s^1$ (Co), and $3s^23p^4$ (S). For consistency, we use a $Z = 8$ supercell for all structures and sample the Brillouin zone with a $3 \times 3 \times 3$ Γ -centered k -point mesh, corresponding to 864 k -points per reciprocal atom.

All calculations were initialized with a collinear antiferromagnetic spin order, consistent with the experimental ground state [82] using $3 \mu_B$ on each Co site. We also use a Hubbard U correction following the Dudarev *et al.* approach [37] with $U_{\text{eff}} = 2$ eV on the correlated Co $3d$ manifold. This strength of static Coulomb interactions is sufficient to open a small band gap in the orthorhombic $Pba2$ structure and is slightly smaller than that reported previously [90]; however, we were unable to stabilize the 90.43°

monoclinic angle observed in the $P2/c$ average structure. We used the Phonopy package with a $2 \times 2 \times 1$ supercell for pre- and post-processing of the dynamical matrix [91]. We parsed and visualized our computational results with the Python package pymatgen [27].

For electronic band structure and density-of-states calculations, we used structures obtained from Rietveld refinement of synchrotron data taken at $T = 300$ K for BaCoS_2 . Although the average structure experimentally is best represented by $P2/c$, it is possible to fit the data with the $Pba2$ model. Both of these symmetries are derived as small distortions to an ideal $P4/nmm$ structure, which we use as a reference structure for analysis of the lattice dynamics and orbital filling. VASP structure files for the three Rietveld refined structures and the ideal tetragonal structure are provided in the supporting information [1].

4.2.2 Experimental Methods

$\text{BaCo}_{1-x}\text{Ni}_x\text{S}_2$ powder was obtained by solid state reaction of BaS (Sigma Aldrich, 99.9%), Co, Ni, and S powders. The Co powder was reduced under flowing 5% H_2 in Ar at 800 °C for 12 hours to remove surface oxides. Stoichiometric amounts totaling around 500 mg of the starting materials were ground with an agate mortar and pestle and pressed into a 6 mm pellet under 950 MPa of pressure. For Co-containing members, the pellets were placed in Al_2O_3 crucibles to prevent reaction with the fused silica tubes. The samples were sealed in fused silica tubes under vacuum with 0.25 atm partial pressure of Ar to suppress S volatilization. BaNiS_2 was heated at 820°C and BaCoS_2 was heated at 970°C, and the intermediate compositions were reacted at temperatures linearly interpolated between the end members. All compounds were reacted for 1.5 days and then quenched in water. For the Co-containing compounds, the silica

tube and alumina crucible had to be quenched separately in a 2-step process to achieve a fast enough quench to avoid decomposition. All compounds were screened by laboratory Cu-K α X-ray diffraction (XRD) to check for impurities. Only minor BaSO_4 or BaS impurities could be identified in each compound.

High resolution synchrotron powder X-ray diffraction was performed at the Advanced Photon Source at Argonne National Laboratory at the 11-BM beamline. Approximately 30 mg of powder was loaded into a kapton capillary and measured for 1 hour at room temperature. Rietveld refinements were performed using the Topas analysis package [68]. Crystal structures were visualized using the VESTA software suite [42].

Pair distribution function measurements were performed at the Advanced Photon Source at Argonne National Laboratory at the 11-ID-B beamline. Approximately 30 mg of powder was loaded into a kapton capillary and measured for 1 hour at room temperature. The data were integrated using calibration with a CeO_2 standard *via* Fit2D [92] and Fourier transformations into real space were performed using PDFgetX3 [93]. Small box modeling at various r -ranges was performed using PDFgui [94] and large box modeling of both the diffraction and pair distribution function data was performed with RMCprofile [95]. RMCprofile results were analyzed with the python package pymatgen [27]. The order parameter of the square pyramidal coordination environments within the supercell were calculated using the pymatgen local environment package with the local structure order parameter function [27].

Bulk magnetic measurements were performed on a Quantum Design MPMS 3 SQUID Vibrating Sample Magnetometer, with approximately 30 mg of powder loaded into a plastic container and mounted in a brass holder. Temperature-dependent magnetization measurements from $T = 2\text{ K}$ to $T = 350\text{ K}$ were performed upon warming under

zero-field-cooled and field-cooled conditions with an applied field of $H = 200$ Oe. Resistivity measurements were performed on bar pellets which were sintered using the aforementioned reaction conditions. The measurements were performed in a Quantum Design PPMS using a press-contact setup for a 4-point measurement with standardized contact spacing. Measurements were taken on warming from $T = 2$ K to $T = 300$ K at a 0.5 K/min sweep rate to avoid temperature hysteresis.

X-ray fluorescence measurements were performed on a Rigaku ZSX Primus IV spectrometer on pressed pellets of the powder material to confirm Co/Ni ratios in samples across the solid solution.

4.3 Results and Discussion

We prepared 6 polycrystalline samples across the series $\text{BaCo}_{1-x}\text{Ni}_x\text{S}_2$ ($x = 0, 0.1, 0.15, 0.25, 0.5, 1$), 3 insulators ($x < 0.21$) and 3 metals. Temperature-dependent resistivity on sintered pellets, shown in [Figure 4.1\(a\)](#), confirms the presence of an insulator-to-metal transition between $x=0.15$ and $x=0.25$. Temperature-dependent magnetization with an applied field of $H = 200$ Oe, shown in [Figure 4.1\(b\)](#) demonstrates suppression of the Néel temperature with increasing Ni in the insulating members and Pauli paramagnetic behavior in the metallic members, consistent with previous reports [79]. Muon spin resonance studies have suggested the transition proceeds through an intermediate antiferromagnetic metal phase [86], but we did not explore compositions in this region. The slight inconsistencies in magnetic susceptibility are likely due to trace cobalt oxide impurities. For the intermediate members, X-ray fluorescence (XRF) was used to confirm the ratio of Co/Ni was consistent with the nominal composition. Our XRF results indicate the ratio of metals in the products are very similar to the nominal

compositions (Table 4.1), so we use the nominal compositions throughout.

Table 4.1: XRF results show the observed composition for the solid solution is close to the nominal composition for all samples.

Nominal Ni (x)	Ni (mol frac)	Co (mol frac)
0.1	0.099	0.901
0.15	0.153	0.847
0.25	0.252	0.748
0.5	0.485	0.515

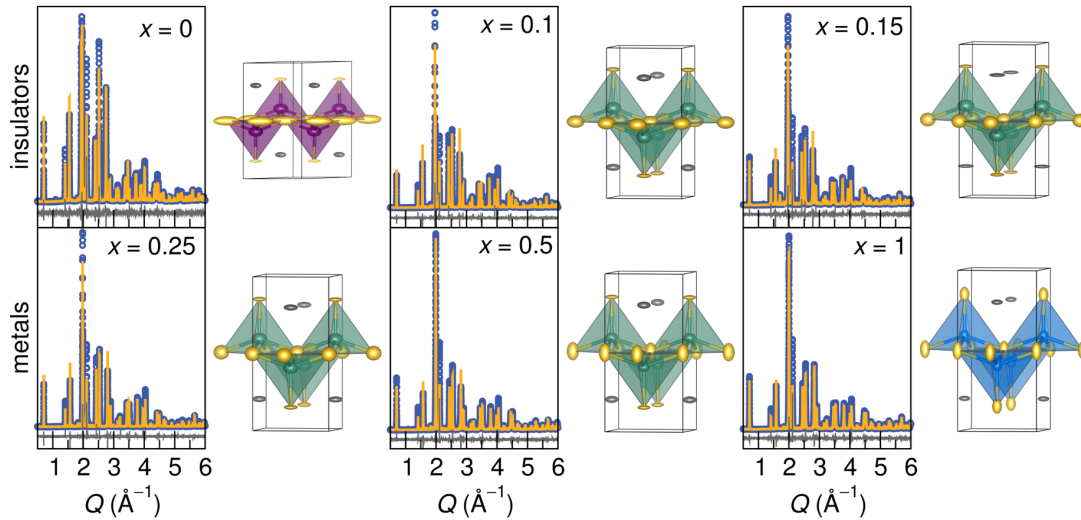


Figure 4.2: Synchrotron diffraction fits and their associated crystal structures across the solid solution from BaCoS_2 to BaNiS_2 show large basal S atomic displacement parameters (ADPs), indicating a high level of disorder on that site. Additionally, slight peak height discrepancies in the fits indicate our average structure $P2/c$ model cannot fully capture the complexities of the crystal structure. The ADPs are shown as 99% probability ellipsoids. Crystallographic tables can be found in Supplemental Information Table I [1].

The $\text{BaCo}_{1-x}\text{Ni}_x\text{S}_2$ crystal structure is characterized by layers of Ba atoms alternating with layers of M -S ($M = \text{Co, Ni}$) square pyramids. In all Ni-containing members of the series, the average structure is tetragonal ($P4/nmm$), with the apical M -S bond length distinct from the 4 basal M -S bonds. In the BaCoS_2 end member, the tetragonal structure undergoes a small distortion into a monoclinic ($P2/c$) space group, splitting the 4 basal M -S bond lengths into 2 sets of 2 equivalent bonds. As shown in Fig-

Figure 4.2, the basal S atomic displacement parameters (ADPs) are elevated across the solid solution, especially in the low- x members, indicating large site disorder.

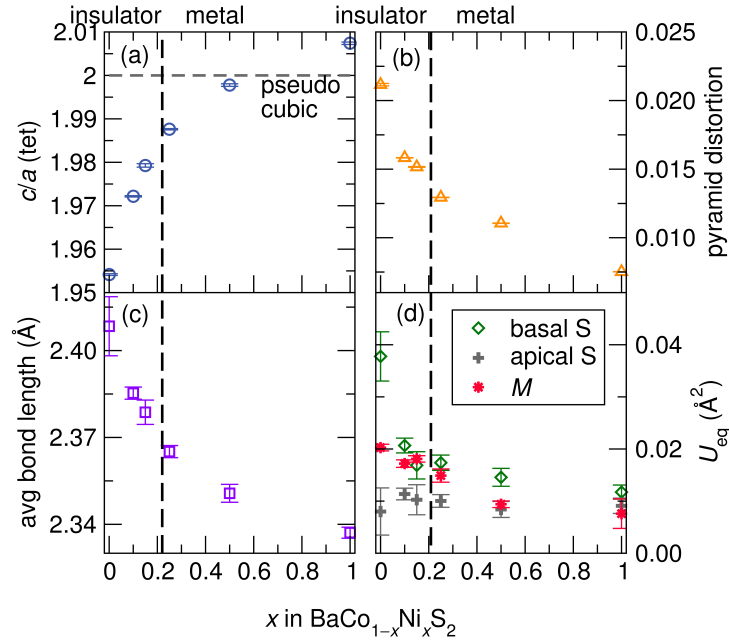


Figure 4.3: (a) The c/a ratio approaches the pseudo-cubic value of 2 as $x \rightarrow 1$ in $\text{BaCo}_{1-x}\text{Ni}_x\text{S}_2$. (b) The distortion of the square pyramid, related to the difference between the apical and the basal $M-S$ bond length, decreases with increasing Ni content. (c) The average $M-S$ bond length decreases with increasing x . (d) Basal S and Co ADPs decrease across the solid solution, indicating less distortions on those sites with increasing Ni. The apical S ADPs are relatively composition independent.

The difficulty in achieving high quality fits to the diffraction data with the $P2/c$ structural model in addition to the large and highly anisotropic sulfide ADPs suggests large local distortions are occurring which are disordered at room temperature. Figure 4.3 shows changes in the average structure across the solid solution. As the amount of Ni increases, both the unit cell and the $M-S$ square pyramids become less distorted, approaching a pseudo-cubic structure near $x = 0.5$. The ADPs, shown in Figure 4.3(d), are larger for the basal S and Co on the Co-rich side compared to the apical S and they decrease upon increasing Ni concentration, suggesting local distortions decrease across the solid solution. The apical S ADPs are relatively constant across the solid solution,

suggesting that site is relatively unperturbed by the differences in electronic structure between Co^{2+} and Ni^{2+} . Anomalously large ADPs on the basal S site have been noted in the literature [88], but an explanation has not yet been proposed.

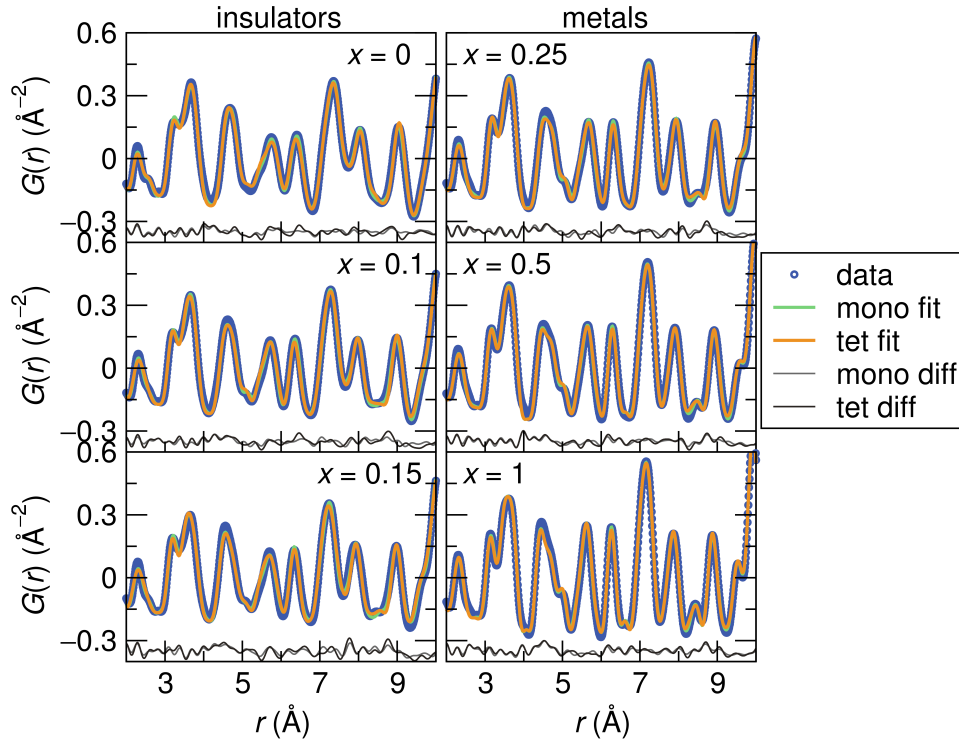


Figure 4.4: PDF data fit to $r = 10 \text{ \AA}$ with a monoclinic and tetragonal space group. In the Co-rich phases, there is a distinct asymmetry on the first peak (corresponding to M -S bonds within the square pyramid) that is difficult to fit even with the monoclinic space group, suggesting distortions of the square pyramids not compatible with $P2/c$ symmetry. At mid- r ranges, the monoclinic fit outperforms the tetragonal fit, especially in the Co-rich phases, indicating solid-solution compositions exhibiting an average tetragonal symmetry also have local distortions.

In order to look for local disorder across the series, which may explain the composition-dependent ADPs, we next perform room temperature powder X-ray pair distribution function (PDF) analyses. PDF data is obtained *via* a Fourier transform of total scattering data which provides a histogram of atom-atom distances in a material, making it useful to uncover local spatial or dynamic distortions. From an examination of the PDF data in the Co-rich members (Figure 4.4), we find an asymmetry of the lowest- r

peak around $r=2.4\text{ \AA}$, which corresponds to M -S bonds within a square pyramid. The asymmetry becomes less prominent with increasing Ni content. The high- r tail of this peak corresponds with longer bond lengths than were found in the average structure, suggesting that locally the square pyramids are distorting but not in an ordered fashion. This significant asymmetry is poorly fit even with monoclinic $P2/c$ symmetry (the average structure of BaCoS_2), indicating that the local S displacements in the M -S square pyramids are incompatible with $P2/c$ symmetry.

For the mid- r ranges from about $r = 5\text{ \AA}$ to $r = 10\text{ \AA}$, we find that the monoclinic structure gives a better fit than the tetragonal structure. This improvement is stronger in samples with higher Co-content, even in samples where the average structure is tetragonal. In order to better understand these trends, we performed additional fits up to $r = 30\text{ \AA}$ with both space groups. We attempted to capture the unit-cell level square pyramidal distortions by limiting the fit range to $r = 5\text{ \AA}$, but there were too many parameters in the monoclinic structure to obtain a statistically significant fit without highly correlated variables. Furthermore, the lowest- r distortions ($<5\text{ \AA}$) did not appear to be compatible with $P2/c$ symmetry and gave unphysical basal S ADPs.

By comparing parameters from fits to the tetragonal and monoclinic space groups as well as comparing fits across length scales, we propose a model for the local structure as well as the short-range order length scale in $\text{BaCo}_{1-x}\text{Ni}_x\text{S}_2$. In [Figure 4.5](#), we find that regardless of the space group or fit range, we recover qualitatively similar average structure trends across the solid solution, showing a reduction in distortion with increasing x . Interestingly, low- x samples are more sensitive to the space group and fit-range used than high- x samples. This indicates that for Ni-rich samples, the local structure is relatively consistent across multiple length scales and is consistent with the average structure. For the Co-rich samples, bond lengths and distortion levels

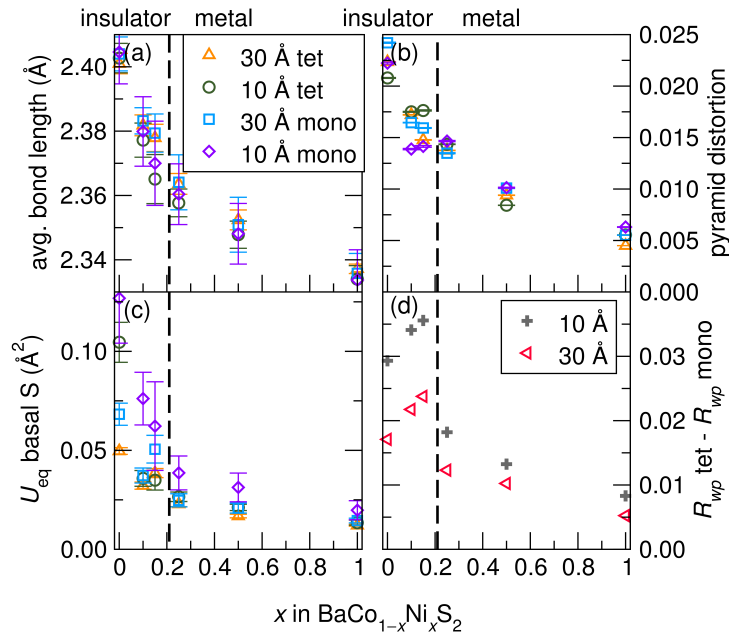


Figure 4.5: (a) Average bond length and (b) square pyramidal distortion across the $\text{BaCo}_{1-x}\text{Ni}_x\text{S}_2$ solid solution show a strong dependence on fit range and space group model for low- x compounds, but converge as x increases, indicating less local distortion in the Ni-rich samples. (c) Basal S ADPs diverge at low- x even when fitting with a monoclinic structure, indicating the basal S atoms are locally displacing from their ideal crystallographic sites. (d) The difference in the weighted- R parameter between the tetragonal and monoclinic structure shows the lower symmetry structure is required to accurately describe the local structure of the insulating samples. Additionally, the distortions are more prominent in the low- r fits, indicating the short-range order begins to disappear by 30 Å.

within a square pyramid, shown in [Figure 4.5\(a\)](#) and (b), are highly tied to the structural model and length-scale of fitting, indicating local square pyramidal distortions at various length scales.

One of the largest changes across the solid solution is the ADP for the basal S. From the fit of the average structure from the diffraction data, the magnitude of the basal S ADP decreases as x increases. In the PDF data, from [Figure 4.5\(c\)](#) we find not only this trend, but additionally that the basal S ADP is larger at lower r -ranges as well as when we allow the symmetry to reduce to monoclinic. This further suggests that the local distortions in $\text{BaCo}_{1-x}\text{Ni}_x\text{S}_2$ are dominated by displacements of the basal S from its crystallographic site.

Finally, the weighted R -parameter, a metric for the goodness-of-fit shown in [Figure 4.5\(d\)](#), indicates that the monoclinic structure always fits the PDF data better than the tetragonal structure, which is unsurprising considering the monoclinic structure has more parameters. However, the monoclinic structure improves the fit more substantially on the Co-rich side. Additionally, the effect is stronger in the 10 \AA fits than the 30 \AA fits, corroborating the observation that the distortions are local and correlations weaken with increasing r . Together, the diffraction and PDF data hint at significant local displacements in the low- x region of the solid solution, with the basal S likely to be the source of these displacements.

We next perform large-box reverse Monte Carlo (RMC) modeling implemented in RMCprofile, which simultaneously fits the average and the local structure data to examine the local displacements without symmetry constraints imposed by a particular structural model. RMCprofile is initialized with a supercell generated from the average structure which is evolved *via* random displacements towards an improvement of the fit of both the PDF and the diffraction data. By performing multiple repetitions of

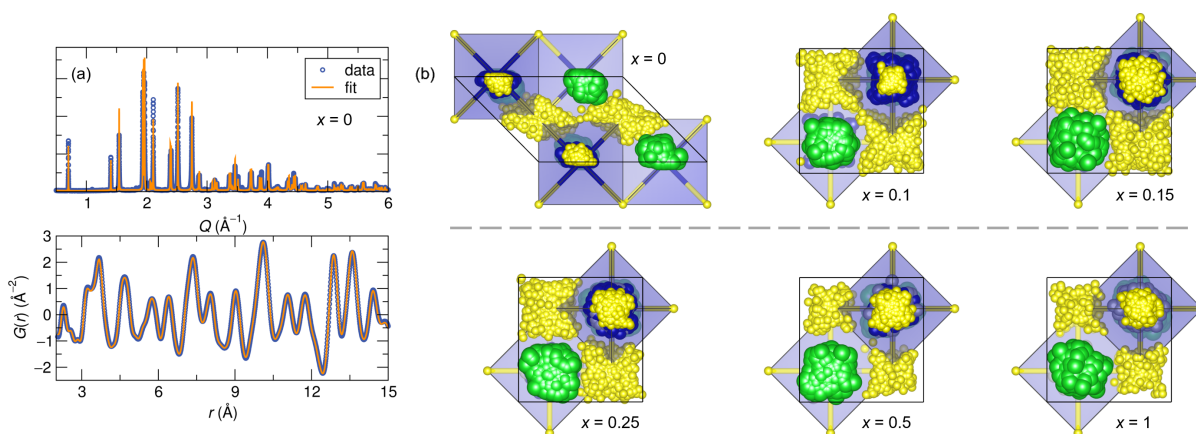


Figure 4.6: (a) Reverse Monte Carlo modeling is able to generate a structure that fits the diffraction and PDF data simultaneously, including the significant low- r distortions in the $x=0$ PDF data. (b) Collapsing the Monte Carlo supercells into the average structure unit cell shows the tendency of basal S atoms to locally displace along the edges of the square pyramids. This displacement allows for symmetry breaking in the plane of the square pyramid which is evident in the PDF data, and is more pronounced in the insulating compounds. The disordered nature of the displacements spatially averages over several unit cells, creating the higher symmetry diffraction patterns.

these calculations, we generate a set of displacements which reproducibly fit both the diffraction and PDF data. By initializing the calculation with a $10 \times 10 \times 10$ (8,000 atom) supercell and repeating the simulation 3 times with different arrangements of the Co and Ni atoms each time in the intermediate phases, we can capture the local structure evolution with Ni content.

Figure 4.6(a) shows a typical fit to the diffraction and PDF data for $x = 0$. The supercell reproduces the significant distortions in the local coordination environment of the M site (the shoulder in the first M -S peak) while also fitting the higher- r local structure and the diffraction data. The supercells collapsed back into their average structure unit cells are shown in Figure 4.6(b), providing a visualization of the difference between the average and local structure across the series. Consistent with ADP data from small box modeling, the most striking displacements occur on the basal S sites. The displacements occur within the plane of the square pyramid, with a prefer-

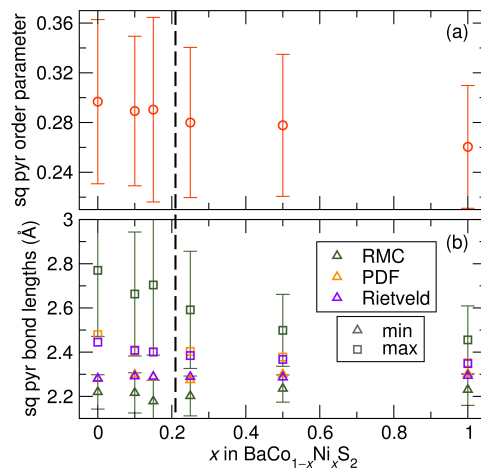


Figure 4.7: (a) The reverse Monte Carlo (RMC) fits show the square pyramidal distortion decreases as x increases, similar to the results of Rietveld refinement and small box modeling. The error bars for the RMC results represent the standard deviation of the pyramidal distortion across the supercell, indicating a large variance in the square pyramid distortions consistent with disorder on the basal S site. (b) Comparison of square pyramidal bond lengths in the Rietveld refinement, small box PDF, and RMC modeling. Although the trends are similar across all three techniques – a convergence of bond lengths towards an ideal square pyramid – the removal of symmetry constraints with RMC allows for a larger amount of distortion as well as variance in distortion. Error bars on Rietveld and small box PDF refinements are shown in earlier figures and omitted here for clarity.

ence for displacements along the edges of the square pyramids. These displacements break symmetry in the plane of the square pyramids and allow for the formation of longer M -S bond lengths, as seen in the low- r PDF data. Additionally, because the displacements lack long-range order, the average structure appears to be of higher symmetry, as seen in the diffraction data.

Analysis of the square pyramidal coordination environment for each supercell provides insight into how the symmetry of the M -site changes across the series. The square pyramidal distortion from RMC modeling, shown in [Figure 4.7\(a\)](#), decreases with increasing Ni, consistent with trends from Rietveld refinements and small box PDF modeling. The error bars indicate the standard deviation in distortion for the 6,000 coordination polyhedra across the supercells at each composition. The large magnitude of the error bars indicates that there is a wide variance in polyhedral distortion across the supercell. While some Co or Ni are located in relatively high symmetry coordination environments, others are located in extremely distorted sites. The X-ray scattering factors from Co and Ni are too similar to distinguish Ni-S and Co-S polyhedra, but additional studies could probe whether the Ni-S pyramids tend to be less distorted than the Co-S pyramids in the intermediate members. To compare the RMC results with Rietveld and small-box modeling, the maximum and minimum bond length in the square pyramid are plotted in [Figure 4.7\(b\)](#) with error bars for the RMC showing the standard deviation across the supercell, similar to [Figure 4.7\(a\)](#). Although the maximum and minimum bond lengths converge towards an ideal square pyramid as x increases in all 3 techniques, the RMC modeling stabilizes more significant distortions by allowing disorder and reducing the symmetry to $P1$.

In both the tetragonal and monoclinic structures, the Wyckoff site of the basal S anions lacks in-plane degrees of freedom, such that the local structure displacements ob-

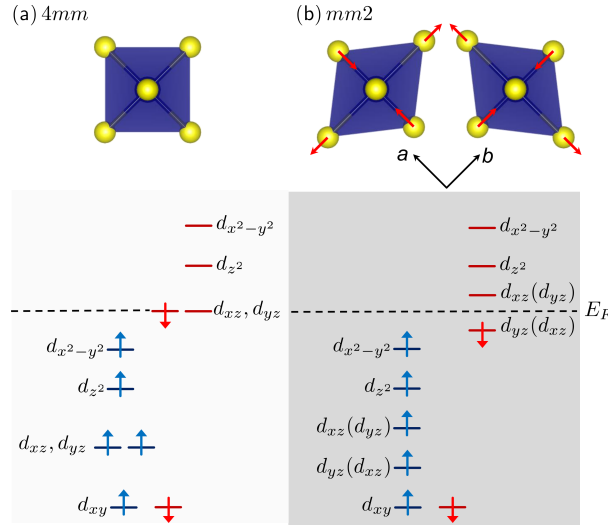


Figure 4.8: The first-order Jahn-Teller instability arising from (a) the degeneracy of the d_{xz} and d_{yz} spin down orbitals within the CoS_5 square pyramids can be relieved by (b) removal of the fourfold symmetry of the ideal polyhedron.

served from our reverse Monte Carlo simulations are incompatible with the space group of the average structure. Such symmetry-breaking in BaCoS_2 may originate from any combination of (i) orbital, (ii) defect-derived, or (iii) magnetic driving forces. First, we examine an electronic instability as the origin for the aforementioned displacements. Owing to the $S = 3/2$ Co^{2+} configuration, three electrons occupy two degenerate d_{xz} and d_{yz} orbitals [96], which leads to a first-order Jahn-Teller (FOJT) instability of the CoS_5 polyhedron that may be removed by symmetry breaking in the xy -plane (Figure 4.8). The edge-connectivity in the (001) plane restricts sulfide displacements directed along the Co–S bond; they cannot coherently occur without changing the bond network.

We ascertain the energy stabilizing displacements that both alleviate the first-order Jahn-Teller instability and are compatible with the square pyramidal connectivity by performing first-principles phonon calculations on the ideal tetragonal structure with $P4/nmm$ symmetry (Figure 4.9(a)). Although we find experimentally a monoclinic

$P2/c$ symmetry with an interaxial angle $\gamma \neq 90^\circ$, arising from a small shearing of the basal plane of the square pyramids, we remove this feature to isolate the degeneracy-lifting effect of the basal S displacements. We find a pair of degenerate modes with $\nu_{1,2} = 3.1i$ THz at the M -point ($k = (\frac{1}{2}, \frac{1}{2}, 0)$, [Figure 4.9\(a\)](#)). Each individual mode comprises displacements of basal sulfide anions along the pyramidal edges, shown in [Figure 4.9\(c\)](#), whereas their combination leads to basal S displacements along the Co-S bonds ([Figure 4.9\(d\)](#)). All displacement patterns transform as the two-dimensional irreducible representation M_4 , cause a $P4/nmm \rightarrow Pba2$ symmetry reduction, and lift the d_{xz} and d_{yz} orbital degeneracy. Although the $\nu_{1,2}$ distortion pattern is more typical of the FOJT in layered structures, [Figure 4.9\(b\)](#) shows that the sulfide displacements along the pyramidal edges (ν_1) are more energetically favorable than those along the Co-S bonds ($\nu_{1,2}$). This dependence is likely due to the reduced elastic energy cost of displacing the basal S diagonally to rather than along the Co-S bonds.

Next, we relaxed BaCoS_2 initialized in this $Pba2$ symmetry and find that it is derived from the tetragonal structure according to the distortion-mode $\eta = 0.98\xi(\nu_1) + 0.13\xi(\nu_2) + 0.15\xi(\Gamma_1^+)$. The dominance of the $\xi(\nu_1)$ coefficient indicates that the displacements ξ comprising η are almost entirely derived from the ν_1 mode with only minor contributions from ν_2 and the fully symmetric mode. The relaxed $Pba2$ structure exhibits basal S displacements along the pyramidal edges, in agreement with the experimentally observed local distortions, and is 8 meV/atom lower in energy than the the $P4/nmm$ structure, shown in [Figure 4.9\(b\)](#).

The effect of these energy lowering basal S displacements on the electronic structure is presented in [Figure 4.10](#). The metallic antiferromagnetic $P4/nmm$ phase transforms into a semiconducting $Pba2$ phase owing to the removal of the orbital degeneracy. [Figure 4.10\(a\)](#) shows d_{xz} and d_{yz} states crossing the Fermi level in the $P4/nmm$ struc-

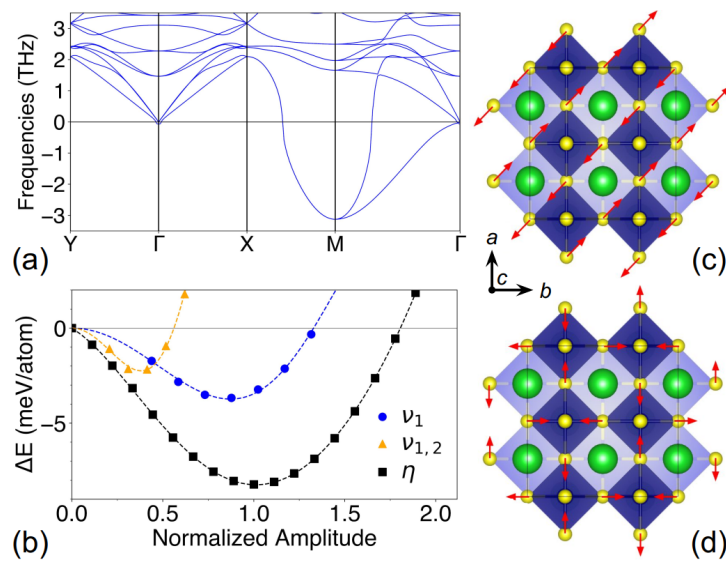


Figure 4.9: (a) The phonon dispersions in the $k_z = 0$ plane of the $P4/nmm$ BaCoS_2 structure reveal imaginary (negative) modes at the M point. (b) Energy calculations for structures as a function of the normalized distortion-mode amplitudes (see text), for ν_1 , $\nu_{1,2}$, and η , where $\eta = 0$ and $\eta = 1$ correspond to the relaxed $P4/nmm$ and $Pba2$ structures, respectively. Illustration of the basal sulfide displacements in the a - b plane corresponding to (c) the unstable phonon $\nu_1 = 3.1i$ THz and (d) the combination of the two degenerate modes $\nu_{1,2}$. Note that ν_2 is equivalent to ν_1 rotated by 90° .

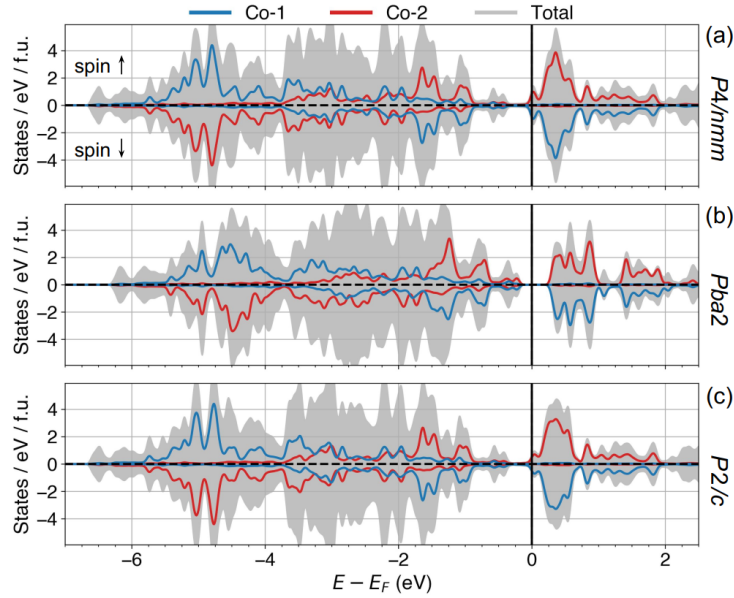


Figure 4.10: Projected DOS for the (a) $P4/nmm$, (b) $Pba2$, and (c) $P2/c$ structures. For (a) and (c), the minority-spin d_{xz} and d_{yz} states span $[-2.5, 0.5]$ eV whereas in the minority-spin channel for (b), the d_{xz} state spans $[-3.0 \text{ eV}, \text{VBM}]$ and the d_{yz} state spans $[\text{CBM}, 0.5 \text{ eV}]$. CBM refers to the conduction band minimum and VBM refers to the valence band maximum. Although $P2/c$ and $Pba2$ both remove the degeneracy of d_{xz} and d_{yz} , lowering the density of states at the Fermi level, the $Pba2$ symmetry breaking is more significant and opens a gap with $U_{eff} = 2 \text{ eV}$. Structures were generated *via* Rietveld refinements of the BaCoS_2 diffraction data taken at $T = 300 \text{ K}$ with the three different structural models. Total (gray) and projections onto majority spin-up (blue) and majority spin-down (red) cobalt species are shown. Electronic band structures near the Fermi level are shown in Supplemental Material Figure S1 [1].

ture whereas $Pba2$ features d_{xz} preferentially and fully occupied over the d_{yz} orbital (Figure 4.10(b)). Although the $P2/c$ monoclinic distortion, shown in Figure 4.10(c), similarly lifts the d_{xz} and d_{yz} orbital degeneracy, with $U_{\text{eff}} = 2$ eV the symmetry breaking is not enough to completely open a gap, leading to a zero-gap semiconducting state. Our identified interdependence of band gap on the basal S displacements suggests that the FOJT instability helps drive the insulator-to-metal transition in the $\text{BaCo}_{1-x}\text{Ni}_x\text{S}_2$ system. Upon electron doping with Ni in the solid solutions, the additional electron will occupy the d_{xz} and d_{yz} orbitals completely, removing the instability. Indeed for $x = 1$ BaNiS_2 , the atomic displacement parameters converge to reasonable values on all sites in the Rietveld refinement and PDF small box modeling, and both the tetragonal structure and monoclinic structure fit the PDF data equally well. From our RMC modeling on the BaNiS_2 end member, we find a convergence of bond lengths within the NiS_5 polyhedra to similar values, indicating less distortion, and in the collapsed supercell, we find smaller displacements from the ideal crystallographic sites.

Alternative symmetry-breaking of the average structure that may produce anomalous ADPs could be due to sulfur vacancies, which have been found in BaCoS_2 [81]. Sulfur vacancies of sufficient concentrations, however, would also trigger a temperature dependent insulator-to-metal transition in $\text{BaCo}_{0.9}\text{Ni}_{0.1}\text{S}_{2-y}$ for $0.05 \leq y \leq 0.20$ [20], which we do not observe in our data, ruling out the possibility of sulfur vacancies as the origin of the anomalous ADPs.

Another scenario could involve magnetism. In the monoclinic structure ($P2/c$), the AFM ordering produces the magnetic space group P_a2/c , no. 13.70, which lowers the basal S site symmetry from $2f(\frac{1}{2}, y, \frac{1}{4})$ to $8g(x, y, z)$, allowing in-plane displacements. However, since the local distortions persist in the paramagnetic phases of $\text{BaCo}_{1-x}\text{Ni}_x\text{S}_2$, the magnetic ordering cannot be the primary driving force for local

M_4 displacements; the additional degrees of freedom from the antiferromagnetic order likely play an auxiliary role in generating the displacements.

4.4 Conclusion

In the insulating members of the $\text{BaCo}_{1-x}\text{Ni}_x\text{S}_2$ solid solution, disorder on the basal S site leads to local symmetry breaking in the plane of the square pyramid. In the square pyramidal configuration, the high-spin Co^{2+} ion has doubly degenerate d_{xz} and d_{yz} orbitals which are partially filled by 3 electrons, leading to a Jahn-Teller instability. In the BaCoS_2 end member, the Jahn-Teller degeneracy appears to be relieved by two separate structural mechanisms – an average structure distortion to the monoclinic $P2/c$ and a local structure distortion of basal S atoms along the edges of the square pyramids. Because only the local structure distortions are observed at room temperature in the paramagnetic insulating compounds, it is possible that the formation of the $P2/c$ structure in BaCoS_2 is related to the antiferromagnetic order. Rietveld refinement, PDF small box modeling, and RMC modeling show that the local S displacements decrease as x increases, consistent with the additional electron in Ni filling the d_{xz} and d_{yz} orbitals completely and removing the instability.

While the average structure of $P2/c$ slightly breaks the in-plane symmetry in BaCoS_2 , we find that the basal S displacements along the pyramidal edges (as in a $Pba2$ structure) further lift this symmetry, widening the band gap between the Jahn-Teller active d_{xz} and d_{yz} states. We hypothesize that at room temperature, BaCoS_2 prefers a dynamically disordered version of the $Pba2$ or similar structure due to the small energy differences (<10 meV/atom) separating the M_4 -symmetry adapted S displacements, the $P2/c$ structure, and the $P4/nmm$ structure. From a combination of DFT-based

modeling and average and local structure analysis, we find the combination of local Jahn-Teller distortions associated with certain band fillings, in the presence of static electron correlation, drive the insulator-to-metal transition in the $\text{BaCo}_{1-x}\text{Ni}_x\text{S}_2$ system. This work strengthens the emerging understanding that following structural changes in great detail is essential for determining the physical underpinnings of insulator-to-metal transitions.

Chapter 5

Factors Driving Crystallization in the Trirutile Structure

The prediction of crystal structure from composition is a coveted goal in the field of inorganic materials. Because the properties of materials tend to be strongly correlated with their crystal structure, it is of interest to predict the crystal structure of a novel material in order to search for materials belonging to a specific structural family. Unlike organic synthetic chemistry in which reactions tend to follow specific rules, the prediction of crystal structure for even binary inorganic materials relies on a complex network of interactions, including ionicity, electron correlations, magnetism, and size considerations. In order to reduce the size of the problem, we focus on the $AB_2(O/F)_6$ composition space and more specifically the trirutile family, which is known for unusual 1D antiferromagnetic behavior. Through machine learning methods, we develop an understanding of how geometric and bonding constraints determine the crystallization of an $AB_2(O/F)_6$ material in the trirutile structure rather than another ternary structure

Ruining Zhang, William Zhang, and Ram Seshadri have contributed to the contents of this chapter

in this space. In combination with density functional theory (DFT) calculations, we predict 18 candidate novel trirutile oxides. We synthesize two of these and show they form in the disordered rutile structure, highlighting the importance of accounting for disorder in computational methods such as machine learning and DFT.

5.1 Introduction

Machine learning is an emerging method in materials science which has been used to predict properties of materials such as hardness [97], band gap [98], and drive the search for new materials with desirable properties such as high performing transparent conductors [99]. For these predictive applications, machine learning models can outperform *ab initio* methods such as density functional theory (DFT) because the low computational cost of running a machine learning algorithm allows for fast screening of hundreds of compounds. In this way, machine learning is a promising method for filtering an initial large pool of candidates into a sample size on which it is feasible to perform DFT or other computationally intensive simulations. Machine learning has also been used to build on fundamental understanding of well known materials; for example, determination of factors which drive crystallization in the Heusler vs the inverse Heusler and related structures [24].

In this work, we use machine learning and DFT to explore the underlying factors which determine whether an $AB_2(O/F)_6$ compound will crystallize in the trirutile structure as well as predict new trirutile oxides. The trirutile family of materials with formula $AB_2(O/F)_6$ are known for unusual low dimensional magnetism [100], typically in the form of 1D antiferromagnetic chains along the [110] direction [101–103], which is the closest metal-metal distance in the structure. The trirutile structure is an ordered

supercell of the rutile unit cell with A - B - B ordering in the c -direction. Because of the similarity to the rutile family, which hosts various canonical insulator-to-metal transition (IMT) materials such as VO_2 [10], we hypothesized that some trirutiles could have a similar structural instability to the one which leads to the IMT in rutile materials [9]. However, we found that even in the high symmetry ideal trirutile structure, without dimerization, all known oxide trirutiles synthesized were insulators, possibly due to the disruption of conduction pathways along the edge sharing octahedra from electron localization or charge disproportionation on A and B ions. Many trirutile compounds with unpaired d -electrons such as CuSb_2O_6 and NiTa_2O_6 have been shown to exhibit Mott or charge-transfer insulating properties [104]. Through machine learning methods we find that, consistent with factors determining crystallization in other structural families, geometric and bonding constraints are the most important features determining the formation of a trirutile structure. In particular, the trirutile structure is preferred over others when both the A and B atoms are relatively small, and less electronegative.

Starting from 461 novel $AB_2\text{O}_6$ compositions, we predict 53 new candidate trirutile materials *via* our machine learning model. From density functional theory (DFT) calculations, we find 18 of the 53 have a formation energy in the trirutile structure of less than 50 meV/atom above the formation energy of their constituent binary oxides. From these 18 compounds, we synthesize two novel $AB_2\text{O}_6$ compounds, TiTa_2O_6 and CrSb_2O_6 and find that they form in the disordered rutile $((A_{1/3}, B_{2/3})\text{O}_2)$ rather than the ordered trirutile structure. Due to the difficulty of predicting and understanding disorder, we did not account for disordered materials in the machine learning data or in density functional theory calculations, which could explain why these were not screened out computationally. For most predicted compounds, it was rare to find solid state synthesis conditions that both stabilized the correct oxidation states for the A

and B cations and optimized reactivity. This highlights the importance of accounting for synthesizability beyond simple DFT energy calculations in computational studies which predict new materials. However, none of the predicted AB_2O_6 compounds we attempted formed non-rutile ternary structure types, indicating the relative success of the machine learning model in predicting preferred local coordination environments based only on composition. This suggests the model has identified the most important chemical features which drive the selection of the trirutile crystal structure.

5.2 Methods

5.2.1 Computational Methods

Data on existing $AB_2(O/F)_6$ compounds was collected from the Inorganic Crystal Structure Database (ICSD) [105]. The data was filtered to remove disordered materials and duplicate entries. For polymorphic structures the stable room temperature structure was chosen, and in cases where multiple stable room temperature structures had been reported, the structure belonging to a known structure type was selected. The data was annotated with binary targets (1 = trirutile, 0 = other) in order to set up a classifier algorithm. The cleaned data contained 293 compounds of which 36 were trirutiles, so the dataset was imbalanced with only approximately 12% positives.

A brief summary is presented here, and full details of the model, hyperparameters, feature selection, and data scaling and cleaning can be found in Appendix 3, as well as comparison of our model with other models from the scikit-learn package. Featureization of the starting materials was performed in matminer [26] using composition based features such as atomic radius and electronegativity, as well as features based

on the guessed oxidation states from the chemical formula, such as the number of valence electrons. The featurized matrix was cleaned, removing features for which data was missing for more than 3% of samples, using the automatminer pipeline [106]. The features were downselected for the most important features in multiple steps. First, features which were correlated $>95\%$ were removed. Then features which sum to $<1\%$ importance by weight within a random forest algorithm were removed. This brought the initial >600 features down to 46. The starting matrix with 46 features was input into a genetic algorithm for further preprocessing and machine learning optimization, as an alternative to grid-based cross validation methods [106, 107]. Within the algorithm, half of the 46 features were removed with recursive feature elimination *via* an extra trees classifier. Tree-based feature reduction methods provide an advantage over principal component analysis (PCA) because they allow retention of the feature names which provide insight into the most important features for predicting within the machine learning model. Polynomial features up to order 2 were implemented, so a “feature” in the model could be a multiplication of two features or a single feature squared. We chose the f_1 score, a combination of recall and precision, as an optimization metric due to the imbalanced nature of the dataset. Additionally, we focused on the recall capabilities of the model because with more negatives than positives, it’s easy for a model to predict false negatives and still perform relatively well. The machine learning algorithm was trained on 75% of the data in a stratified manner to obtain a similar number of positives in the training and test set. Selection of the machine learning model and hyperparameters was performed in automatminer using nested cross validation to obtain the model with the best and most reproducible f_1 score. The best model was an extra trees classifier with a f_1 score on both training and test data of 82%, indicating the model was not over-fitting the data.

For the prediction of new oxide trirutile candidates, common valences of the elements (excluding rare earth elements) were tabulated and combinations of $A + 2 \times B$ which combined to $12 (= 6 \times 2)$ were input in a matrix. Compounds which existed already were removed and the model was implemented on 461 new AB_2O_6 formulas. 53 were predicted as possible trirutile candidates, similar to the ratio of positives in known materials.

For the 53 predicted candidates, density functional theory (DFT) calculations were used to calculate the energy of the ternary compounds in the trirutile structure compared with the energy of their reported binaries. All electronic structure calculations were performed using the Vienna Ab-Initio Simulation Package (VASP) [43] with projector-augmented-wave pseudopotentials [44, 45] within the Perdew–Burke–Ernzerhof generalized gradient approximation [46]. All calculations used an automatically generated Gamma-centered K-point grid with a density of 50 and an energy cutoff of 550 eV with a ferromagnetic initialization on non $d0$ transition metals. In binary compounds where the magnetism is known, the nearest collinear magnetic configuration was used to initialize the calculations. Structural relaxations with symmetry on were performed for all materials in a 3 step process in which the unit cell and ion positions were allowed to relax until convergence, then just the ion positions, and then a static energy calculation. Gaussian smearing with a sigma of 0.1 was used for the structural relaxations, and the Blöchl tetrahedron method was used for the final static energy calculations to obtain the most accurate total energy.

5.2.2 Experimental Methods

TiTa₂O₆ powder was obtained by solid state reaction of TiO and Ta₂O₅ powders, and CrSb₂O₆ was obtained by reaction of Cr₂O₃, Sb₂O₃, and Sb₂O₅. Stoichiometric

amounts totaling around 500 mg of the starting materials were ground with an agate mortar and pestle and pressed into a 6 mm pellet under 950 MPa of pressure. The pellets were placed in Al_2O_3 crucibles capped with Ta foil to prevent reaction with the fused silica tubes. The samples were sealed in silica ampoules under vacuum with a quarter of an atmosphere of Ar to suppress volatilization. Both samples were slowly ramped to 1100°C over 3 days, reacted for 5-7 days, and allowed to cool in the furnace. Laboratory Cu-K α X-ray diffraction (XRD) with an Empyrean diffractometer was performed and CuSb_2O_6 formed a phase pure disordered rutile structure, while TiTa_2O_6 formed the same but with a small Ta_2O_5 impurity. Slow cooling and re-annealing at lower temperatures was performed in an attempt to order the cations into a trirutile structure but a tripling of the unit cell was never observed within lab resolution. X-ray fluorescence measurements were performed on a Rigaku ZSF Primus IV spectrometer on pressed pellets of the powder material to confirm composition in TiTa_2O_6 .

5.3 Results

The composition space $AB_2(\text{O/F})_6$, with approximately 293 known compounds, is home to a variety of structure types. Figure 5.1 highlights some representative structure types in this space. While the trirutile family is the most common, with 36 members representing approximately 12% of $AB_2(\text{O/F})_6$ compounds, no one type is preferred within this composition region. There is varying coordination of the A and B cations although octahedra are a common motif. Two types that appear similar to the trirutile structure are the Na_2SiF_6 and the columbite structure, in which both A and B atoms are octahedrally coordinated in alternating fashion in 3 dimensions.

Starting from the 293 known $AB_2(\text{O/F})_6$ compounds from the ICSD, we trained a

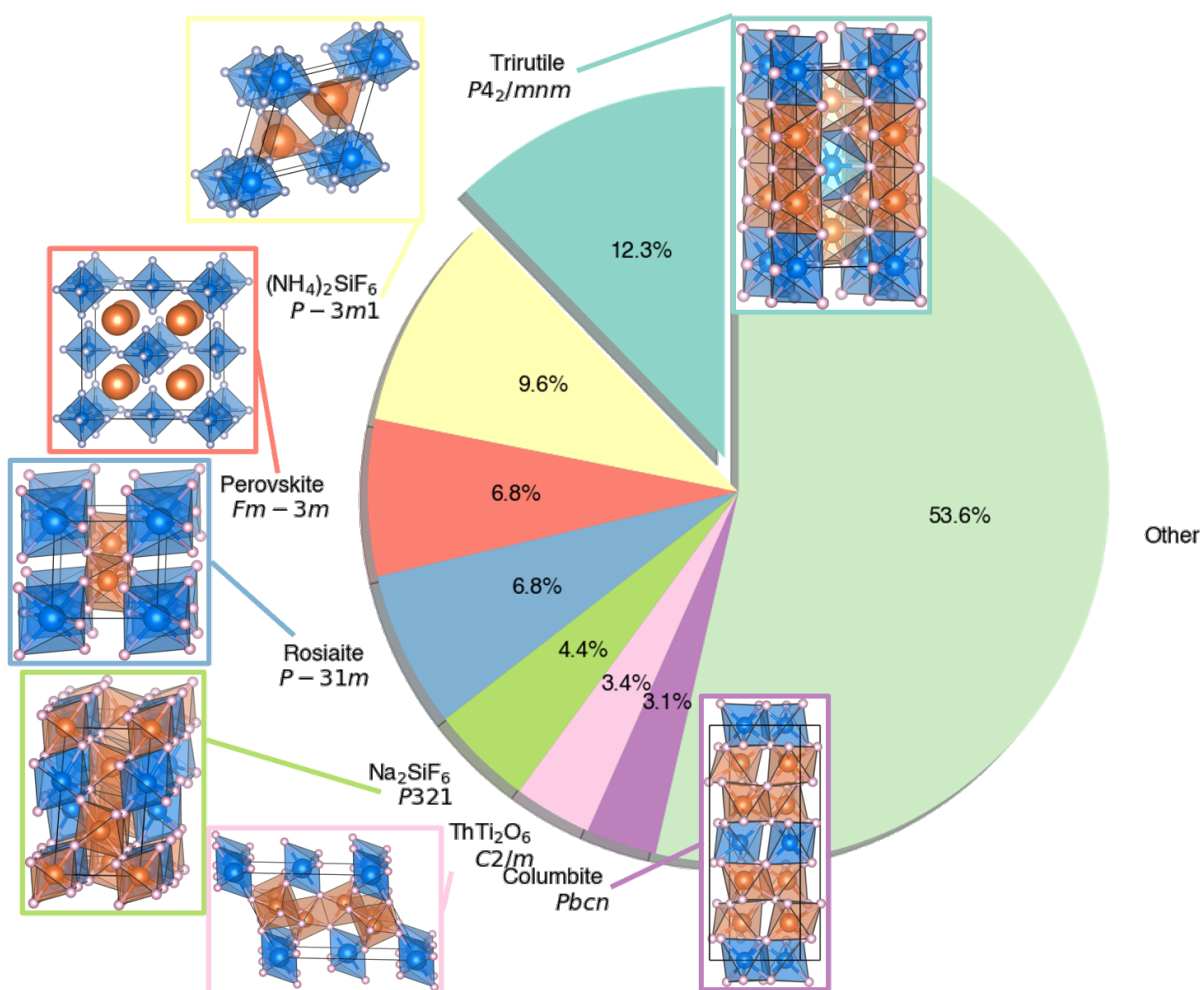


Figure 5.1: The most common structure types in $AB_2(\text{O}/\text{F})_6$ composition space. No one structure type dominates the landscape in this region. Most structures are characterized by octahedral coordination of the A or B sites, and layered compounds feature prominently both in the common structure types and in the “Other” section.

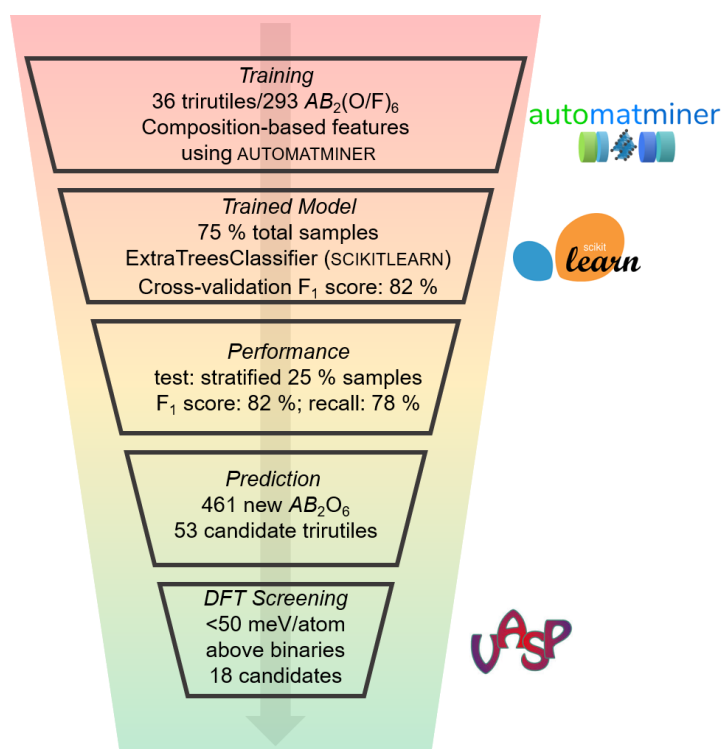


Figure 5.2: The process flow for predicting new trirutile materials. Using only composition-based features through automatminer, we trained a machine learning model to classify compounds into trirutile or not trirutile. The model was then used to classify 461 novel AB_2O_6 compositions and 53 were potential trirutile candidates. Density functional theory was used to calculate the energy of the ternary trirutile relative to the oxide binaries as a proxy for “synthesizability” and 18 compounds emerged as promising new trirutile oxides.

machine learning model to classify the compounds into trirutile or not trirutile. Our process flow is shown in Figure 5.2. Details of the machine learning process and model can be found in the methods and the SI. The best performing model was an extra trees classifier, a form of decision tree, with a cross validation f1 score on the training data of 82% and on the test data of 82%. The f1 score, a combination of precision and recall, is a good metric for unbalanced datasets where negatives outweigh positives (in our data only 12% are positives). The model was used to classify 461 unknown AB_2O_6 materials and predicted 53 should be trirutiles, similar to the percentage of trirutiles in known compounds. Because the machine learning model has no thermodynamic information, we used DFT to evaluate whether the trirutile candidates could feasibly be synthesized. A basic proxy for stability is the formation energy of the product relative to the starting materials. For all 53 candidates, the energy of the reactant binary oxides were compared to the energy of the product trirutile using density functional theory (DFT) calculations, and a conservative threshold of 50 meV/atom above the binary energy was set as the limit of possible stability. When these compounds were additionally screened for dangerous starting materials (such as OsO_4), 18 materials emerged as promising novel trirutile candidates.

In addition to using the model to predict new trirutile materials, we aim to understand the chemistry that governs crystallization in the $AB_2(O/F)_6$ composition space. A common method for clustering structure types in ternary composition space is to plot the ionic radii of the A and B atoms. In Figure 5.3, we plot the ionic radius of the B -site against the ionic radius of the A -site for all common structure types in the $AB_2(O/F)_6$ space. This performs reasonably well at clustering structural families, but there is still significant overlap, notably between the trirutiles and the columbite and rosielite families, indicating more complex features are necessary to understand crystallization in

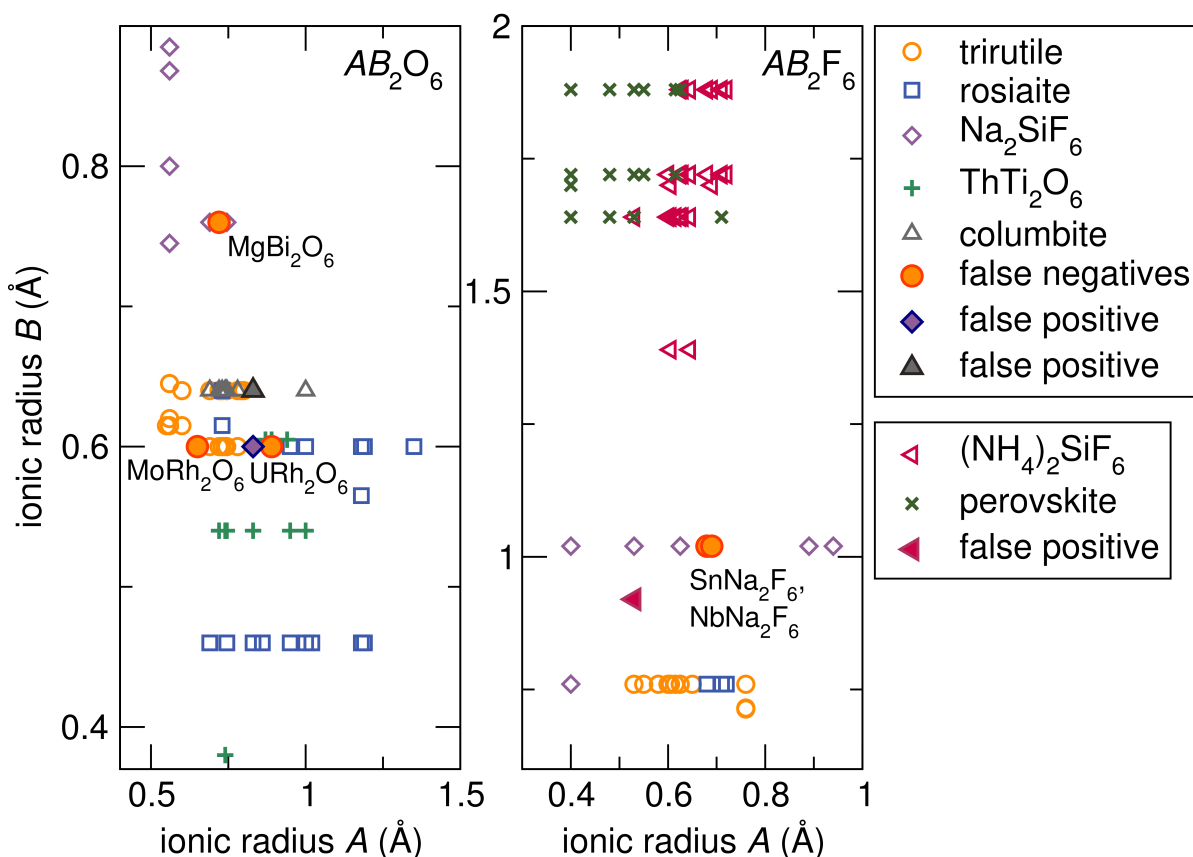


Figure 5.3: Plotting the ionic radius of the B -site vs the atomic radius of the A -site performs reasonably well at clustering families in both the AB_2O_6 and AB_2F_6 space. The machine learning model is able to correctly predict even overlapping compositions on these axes, indicating it includes more complex factors. From the model, both Na-containing fluoride trirutiles are predicted as false negatives, likely due to the scarcity of Na trirutiles. In the oxide trirutiles, one outlying Bi compound and two Rh-containing trirutiles are false negatives.

these materials. However, the machine learning model is able to correctly predict overlapping compounds in this view, indicating chemical features used by the model are able to differentiate trirutile compositions from others with similar ionic radii. The clearest flaw in the machine learning model is its inability to predict Na-containing fluoride trirutiles. This is likely because only two Na trirutiles have been reported while there are several ANa_2F_6 compounds not in the trirutile structure. The only false positive in the fluorides is $MnLi_2F_6$ which is chemically similar to known trirutiles $CrLi_2F_6$ and VLi_2F_6 . In the oxides, two Rh-containing trirutiles are predicted incorrectly, likely because there are only two Rh-containing oxides reported in the training data. Interestingly, both oxides falsely predicted to be trirutiles, $MnTa_2O_6$ and $MnSb_2O_6$, have reported metastable trirutile phases [108, 109].

From the model, we extract the 10 most important features, denoted by their weights in the model, that are used to decide whether the composition is a trirutile, as shown in Figure 5.4(a). The most important feature (feature 1) includes both geometric and bonding factors – the maximum atomic radius present in the composition and the band center, which is related to the mean electronegativity of the elements of the compound. In order to determine the most relevant features for further study, a correlation matrix was generated for the top 10 features, shown in Appendix 3. The most important feature is strongly correlated with 7 others of the top 10. This indicates that a combination of geometry and bonding is by far the most important determinant of whether the trirutile structure will form. Feature 7, which is not as correlated with the others, is the square of the band center, again showing the importance of bonding. Feature 9, which is the other unique feature, is a combination of the average deviation of the electronegativity of the atoms and the average deviation of the number of valence electrons. Figure 5.4(b) shows feature 9 plotted versus feature 1. The trirutiles

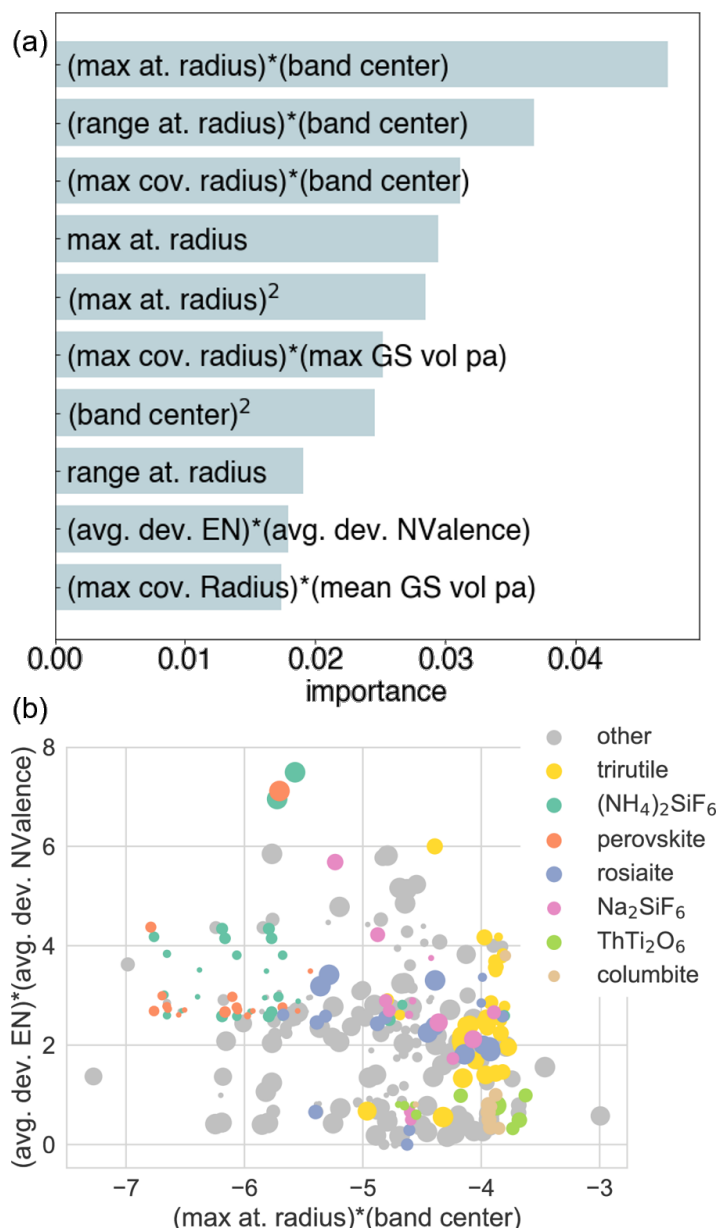


Figure 5.4: (a) The 10 most important features for classification of a trirutile composition in this model. (b) A plot of feature 9 vs feature 1 shows how these two features start to cluster the trirutiles. The size of the points is proportional to feature 7, which also helps to distinguish the trirutiles from neighboring compounds. Interestingly, these features appear to cluster other structure types such as vacancy-ordered double perovskites and the $(\text{NH}_4)_2\text{SiF}_6$ compounds. This indicates that similar features may govern crystal structure formation across many families.

cluster at the less negative end of the x -axis and the medium-to-high end of the y -axis. The x -axis trend indicates that the trirutile structure is formed preferentially when the band center is less negative (closer to 0, indicating the A and B atoms have lower electronegativity) and when the maximum atomic radius in the compound is relatively small. The y -axis trend shows that once these criteria are met, A and B atoms with a larger difference in valence electrons or a larger difference in electronegativity are preferred. Interestingly, these features also seem to cluster the perovskites, $(\text{NH}_4)_2\text{SiF}_6$ compounds, and columbites, indicating similar features may govern crystal structure formation across this composition space.

By evaluating trends in the values of the most important features, it is possible to generate a simplified human-readable decision tree to determine whether a given composition will form in the trirutile structure, shown in Figure 5.5. While this does not capture the full complexity of the family, these features describe most of the known trirutiles and exclude most other $AB_2(\text{O}/\text{F})_6$ compounds. The first factor favoring trirutile formation is a maximum atomic radius in the compound of < 150 pm. This excludes most of the alkali and alkaline earth elements, as well as rare earths, and lead or bismuth compounds. Most compounds with very large atoms in this composition seem to prefer the perovskite and $(\text{NH}_4)_2\text{SiF}_6$ structure types. The preference for a low maximum atomic radius can be explained by the compact nature of the trirutile structure, which is characterized by alternating edge-sharing octahedra. There are no sites like the B site in the double perovskite which can be occupied by a larger atom. Once the geometry has been satisfied, a band center near 0 is desirable (this is related to a low mean electronegativity of the elements). This bonding restriction excludes sulfates, and all compounds where the A or B site is a halogen or chalcogen, as well as discourages late $4d$ and $5d$ elements. The last conditions are more flexible and less

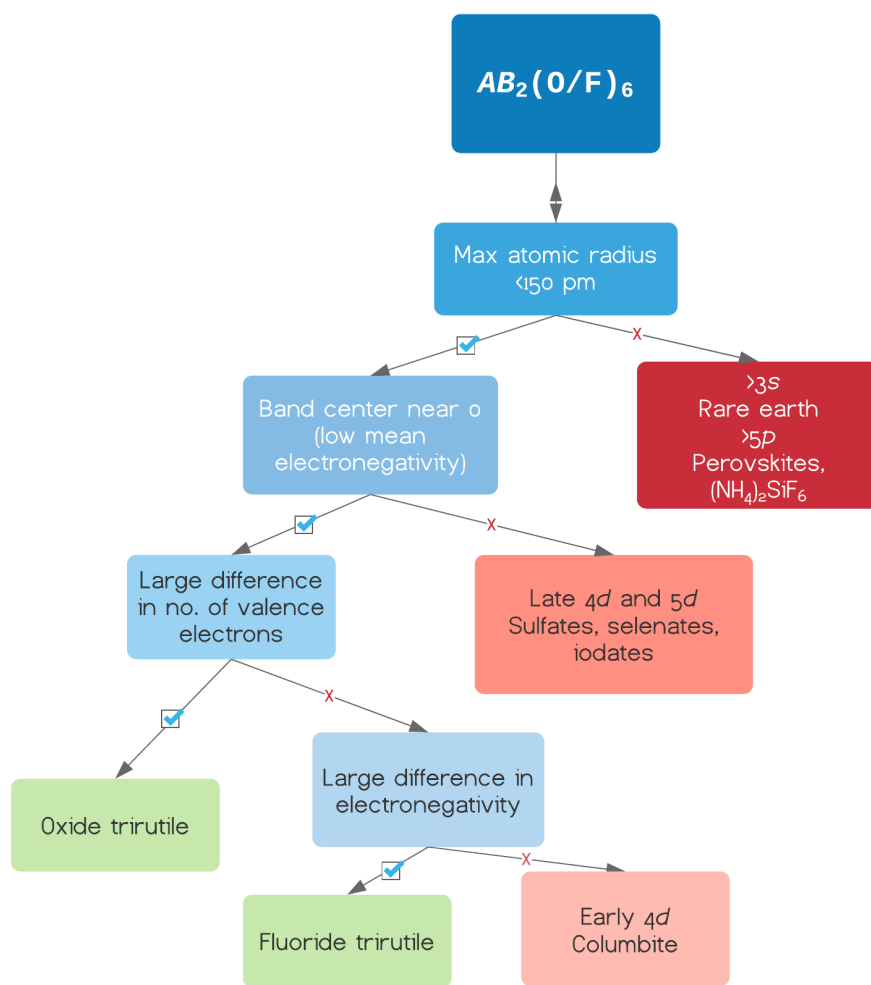


Figure 5.5: A simplified decision tree for the formation of the trirutile structure. The trirutile structure prefers small A and B -site atoms, likely due to the compact edge-sharing octahedral network. Additionally, low electronegativity A and B atoms are preferred relative to other compositions in the region (such as sulfates with the formula $A(\text{SO}_3)_2$). Finally, the trirutile structure is preferred in oxides when the number of valence electrons of the A and B atoms are very different (*i.e.* $3d$ and $5d$ or $5p$) and in fluorides when the bonding is very ionic.

Composition	ΔE (meV/atom)	Composition	ΔE (meV/atom)
PtV ₂ O ₆	-6.92	MnPt ₂ O ₆	25.37
TiTa ₂ O ₆	-5.28	GeSn ₂ O ₆	25.41
ReMn ₂ O ₆	-3.14	GeMn ₂ O ₆	26.82
IrCr ₂ O ₆	0.05	WAl ₂ O ₆	30.27
CrSb ₂ O ₆	1.88	RuRe ₂ O ₆	31.45
IrV ₂ O ₆	2.24	ReFe ₂ O ₆	41.09
IrMn ₂ O ₆	16.92	TiIr ₂ O ₆	46.02
BeSb ₂ O ₆	17.95	MnSn ₂ O ₆	48.36
ReV ₂ O ₆	24.54	WNb ₂ O ₆	50.00

Table 5.1: DFT-based stability calculations for predicted trirutiles. ΔE refers to the energy of the trirutile relative to its constituent binary oxides.

immediately intuitive. For oxide trirutiles a large difference in the number of valence electrons across the composition, as denoted by the average deviation of the NValence feature from the Magpie database, is preferred. This criterion is related to the way that the NValence feature is calculated. For $5d$ atoms, the f electrons are counted in the valence electrons. Therefore, the preference for a large deviation in NValence for oxide trirutiles highlights the predisposition for $3d$ (or $3s$) and $5d$ or $5p$ combinations over $3d$ and $4d$ combinations, which are common in the columbites. For fluoride trirutiles, a large deviation of electronegativity across the composition is preferred. Most fluoride trirutiles are characterized by extremely ionic bonding and include small alkali metals like Li and Na. An understanding of the most important features allows us to gain insight into the mechanisms governing crystal structure formation in the trirutiles as well as other structure types within the region.

Now that we have established some guidelines related to trirutile formation, we turn to the results of DFT calculations on predicted novel trirutile oxides. The energies of the most stable candidates relative to their constituent binary oxides are shown in Table 5.1. Among the top candidates, we find many in which the AO_2 or BO_2 binaries are known to form in the rutile structure. For example, the most stable predicted

candidate relative to the starting materials is PtV_2O_6 , and its binaries, PtO_2 and VO_2 , are both rutiles. Additionally, we find many compounds which are chemically similar to the known trirutiles. TiTa_2O_6 is similar to many of the known tantalate trirutiles such as FeTa_2O_6 or MgTa_2O_6 . ReMn_2O_6 is similar to ReCr_2O_6 , and CrSb_2O_6 is similar to CrTa_2O_6 . The similarity of predicted compounds to known compounds suggests that the model is picking up on underlying chemical trends in the trirutiles.

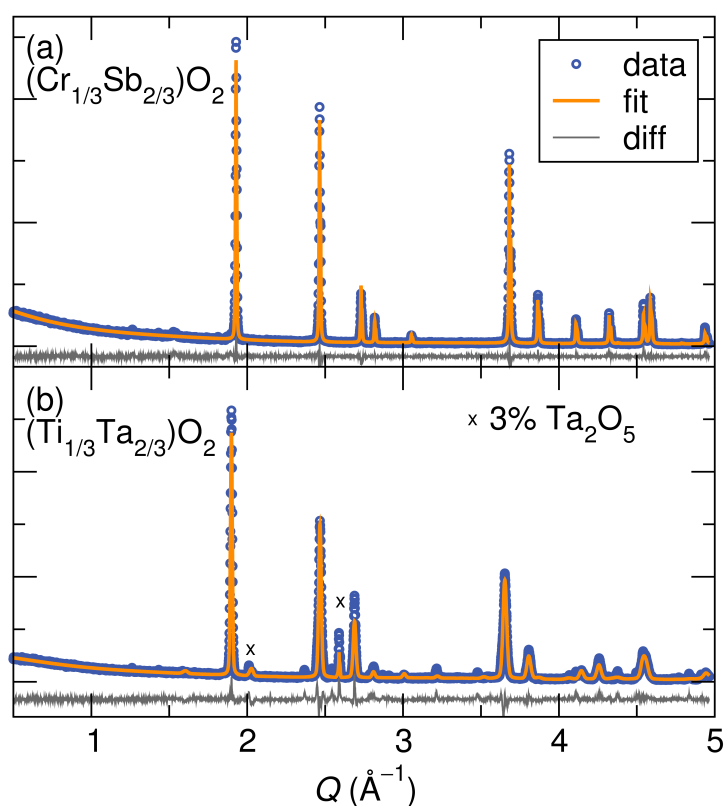


Figure 5.6: Laboratory Cu-K α diffraction patterns on (a) CrSb_2O_6 and (b) TiTa_2O_6 show that the structure corresponds to a disordered $(A_{1/3}, B_{2/3})\text{O}_2$ rutile structure. There is a slight Ta_2O_5 impurity in $(\text{Ti}_{1/3}, \text{Ta}_{2/3})\text{O}_2$ and it also appears to be less ordered than the $(\text{Cr}_{1/3}, \text{Sb}_{2/3})\text{O}_2$ compound, indicated by the broadening of peaks at high- Q .

With a candidate list of new trirutiles, we attempted synthesis *via* traditional solid state methods. We found that compounds with noble metals (Pt and Ir) were difficult to react because the low stability of the 4+ valence state limited the synthesis con-

ditions to low temperatures (typically $< 700^\circ\text{C}$), where reactions proceeded slowly or not at all. Due to the cost of Re precursors, we did not attempt any of the Re-based candidates. However, CrSb_2O_6 and TiTa_2O_6 did react at high temperatures (1100°C) to form ternary compounds. From lab X-ray diffraction, shown in Figure 5.6, we show fits to each pattern for an $(A_{1/3}, B_{2/3})\text{O}_2$ rutile model. While we were unable to refine occupancies on the transition metal site reliably due to limits of the data resolution, X-ray fluorescence measurements on $(\text{Ti}_{1/3}, \text{Ta}_{2/3})\text{O}_2$ indicate the product composition (32.8% Ti, 67.2% Ta) is close to the nominal composition. Unfortunately, we could not find an annealing scheme that would order the A and B cations to form the trirutile structure. It is puzzling that CrSb_2O_6 fails to globally order while CrTa_2O_6 forms the trirutile structure [110]. It's possible that the smaller Sb cannot accommodate the desired Jahn-Teller distortion of Cr^{2+} , leading to frustration. The erroneous prediction of a stable ordered trirutile phase for these compositions is likely due to the failure to account for disorder in either the machine learning model or the DFT. Because of the difficulty of modeling and understanding disordered materials, any disordered materials were thrown out in our original data cleaning process for the machine learning training data, and disordered supercells were not calculated in the DFT screening. Despite the disorder, the formation of a ternary rutile phase indicates the model has a consistent ability to predict the local coordination environment in this composition space.

5.4 Conclusion

Machine learning is a powerful tool for making connections in complex systems with many variables. While the $AB_2(\text{O}/\text{F})_6$ composition space is small compared to many databases used in machine learning, it has a multitude of competing crystal structures.

The most common crystal structure in this region, the trirutile family, makes up only 12% of the members, competing with vacancy-ordered double perovskites, layered compounds, columbites, and many others. Understanding the factors which underpin crystallization in the trirutiles not only helps us understand the chemistry in this family, but also gives insight into crystallization more generally. We find that the trirutile structure is preferred overall when A and B atoms are small and less electronegative, and that the oxide trirutiles are typically a combination of a $3d$ or $3s$ atom with a $5d$ or $5p$ atom. The fluoride trirutiles are typically Li with a $3d$ atom or Na with a $4d$ atom. We discover that similar geometric and bonding features that are important for the trirutiles appear also to be important for other families, such as the perovskites. In combination with DFT screening for stability, we predict 18 novel trirutile oxides. Of those, we are able to synthesize ternary oxides of 2 and show that they form in a disordered rutile structure. We did not form any non-rutile ternary materials, highlighting the success of the model in predicting local coordination environments. However, the energetics governing disorder are challenging to understand and predict and require special consideration. Additionally, the goal of accounting for synthesizability in inorganic materials, for example by including Ellingham diagrams or other solid state chemistry benchmarks in a machine learning model, is crucial to accelerate the timeline for the design and realization of novel functional materials.

Chapter 6

Summary and Outlook

In this dissertation we demonstrate how subtle changes in crystal structure can have large changes on magnetic and electronic properties. In the lacunar spinels, we find that small changes in the symmetry of a tetrahedral cluster can change the moment as well as the magnetic phase diagram. More particularly, in GaMo_4Se_8 , we find small changes in magnetocrystalline anisotropy due to a slight distortion from $R\bar{3}m$ to $Imm2$ which is only visible with high resolution synchrotron diffraction changes the magnetic phase diagram from a complex mix of cycloids and skyrmions to a uniaxial ferromagnet. This two space group phase transition may also be occurring in GaMo_4S_8 , which has similar diffraction data reported in the literature. A more thorough study of GaMo_4S_8 could be instrumental in relating its crystal structure to its observed unusual magnetic behavior [61]. In a more general sense, the importance of magnetocrystalline anisotropy to the formation of canted spin phases as well as its sensitivity to small symmetry changes informs modeling efforts to predict novel materials which can host chiral spin textures. Any modeling effort aimed at predicting new chiral magnetic materials must carefully account for magnetocrystalline anisotropy, and ensure that

it does not dominate the energy landscape and suppress the formation of any spiral magnetic phases.

In $\text{BaCo}_{1-x}\text{Ni}_x\text{S}_2$, we show that local sulfur displacements along the edges of square pyramids are a result of dynamic Jahn-Teller distortions and are correlated with the insulating phase. Electron correlation effects and the subsequent electron localization in Co-rich members can be tied to the distorted square pyramidal coordination environment in these materials. This highlights the importance of not only carefully studying the average structure but also looking at the local structure, especially when features in the diffraction results (such as anomalously large sulfur ADPs) hint at local structure distortions.

Finally, in the $AB_2(\text{O/F})_6$ composition space, we show through machine learning that atomic radii, electronegativity, and valence electrons can help explain why some materials form in the trirutile structure type rather than others, like columbites or vacancy-ordered double perovskites. In our predictive work using both machine learning and DFT, we find that accounting for disorder, as well as synthesizability, is crucial in order to avoid a synthetic bottleneck and experimentally realize predicted materials. In all of these systems, a combination of crystallography, modeling, and properties characterization is necessary to tease out the complex interactions that explain functionality.

6.1 Explaining the behavior of the Ta- and Nb-containing lacunar spinels

While the V- and Mo-containing lacunar spinels behave similarly, with a low temperature $R\bar{3}m$ crystal structure and largely ferromagnetic interactions, the Ta- and Nb-containing lacunar spinels have quite different behavior. The Ta- and Nb-containing compounds undergo a more subtle structure transition into a reported tetragonal $P\bar{4}2_1m$ structure (although GaNb_4Se_8 has been recently reported in the $P2_12_12_1$ orthorhombic space group at low temperature [111]) which appears to be coupled with a decrease in magnetization. This is in contrast to the V and Mo compounds, where the structural and magnetic transitions are separated by about 20 K. Furthermore, the Ta and Nb containing compounds have a reported superconducting transition under pressure [13] which has not been observed in the V or Mo compounds.

The Ta and Nb containing lacunar spinels are much less studied than their V and Mo analogues, both in their crystal structure evolution as well as magnetic characterization. Due to the extremely small splitting of peaks in the structural transition – the lattice parameter deviation from cubic in GaTa_4Se_8 is reported to be 0.16% [111] – temperature dependent synchrotron diffraction is necessary to fully understand the structural evolution of these materials. This is especially necessary in GaNb_4Se_8 , where weak supercell reflections have been reported from powder diffraction as an intermediate cubic phase between the high temperature $F\bar{4}3m$ and low temperature orthorhombic structure [111]. Preliminary single crystal diffuse scattering data we have collected on GaNb_4Se_8 confirms the presence of supercell peaks and multiple structural phase transitions, but there is also diffuse scattering suggesting contributions of local structure fluctuations in the $F\bar{4}3m$ phase. The suppression of magnetic moment at the phase

transition in GaTa_4Se_8 and GaNb_4Se_8 has been reported to be the formation of a spin singlet state in which spins on neighboring clusters pair in the formation of a valence bond solid [14, 111]. However, due to the very small change in inter-cluster distance at the phase transition, more theoretical and experimental work needs to be done to explain the origin of this behavior. Because of the small magnetic moment of $1 \mu_B/M_4$ cluster, as well as the strong effects of spin-orbit coupling, the magnetism is difficult to probe with neutron scattering techniques.

We have performed inelastic neutron scattering at low temperature on powder samples of GaNb_4Se_8 and GaTa_4Se_8 to both look for signatures of the spin singlet state and understand the structural phonon modes. While no magnetic signal is immediately apparent, possibly a consequence of the low moment, the phonon spectra of both materials have signatures of cluster compounds. The bands are very flat, indicating highly localized distortion modes, likely on the order of a single cluster. Computational modeling and data analysis efforts are ongoing.

6.2 Extending study of the BaMS_2 system to other M -site atoms

Within the $\text{BaCo}_{1-x}\text{Ni}_x\text{S}_2$ solid solution, a temperature dependent synchrotron diffraction and pair distribution function study would help elucidate the competition between the tetragonal state, the $P2/c$ distortion, and the local sulfur displacements, and how they are related to the magnetic ordering as well as the insulator-metal transition. A probe of structure evolution through the magnetic transitions could clarify interactions which stabilize the average structure distortion in $P2/c$ and which are related to the

local S displacements. Additionally, single crystal studies would provide opportunities for optical measurements such as second harmonic generation and raman scattering to further probe structural instabilities and compare with the results of modeling. Computationally, more detailed studies to look for orbital ordering and magnetostructural coupling could prove fruitful.

While the Co–Ni solid solution is the most studied within the BaMS_2 system, there is an open research area in substituting other transition metals on the M -site. Moving beyond the Co–Ni solid solution, there are opportunities to tune the transition metal in order to understand how chemical substitution affects the structural and electronic properties of the material. We have begun preliminary synthesis efforts in substituting Cu for Ni in BaNiS_2 and early magnetization measurements reveal interesting magnetic behavior. Further synthetic efforts to make a series of compositions in this series could pave the way for a similar study to that from Chapter 4. Literature reports on this solid solution have been inconclusive with regard to resistivity behavior across the series, so understanding whether the substitution of Cu drives BaNiS_2 into an insulating state could be exciting. Furthermore, synchrotron diffraction and pair distribution function studies could reveal how the substitution of Cu affects the square pyramidal coordination environment in this structure.

6.3 Characterization of predicted trirutile materials

In the synthesized CrSb_2O_6 and TiTa_2O_6 materials for which lab XRD shows a disordered rutile structure, XRF measurements would be a first step in showing that the product composition is similar to the nominal composition. Pair distribution function measurements could show whether there is a tendency for the metal cations to lo-

cally order. Based on the large size differences between Cr and Sb and Ti and Ta, we would expect to see some sign of local ordering. Additionally, in other Cr-containing trirutiles, significant Jahn-Teller distortions of the octahedral environment have been reported. It would be interesting to see whether these distortions occur locally in CrSb_2O_6 . Despite the disorder, temperature-dependent magnetization and resistivity measurements would be useful tools for characterizing the functional properties of CrSb_2O_6 and TiTa_2O_6 .

Extending machine learning methods to other crystal systems could generalize our model in order to develop an understanding of crystallization in other ternary families, and help refine the predictive abilities of our computational models to generate candidate materials with selected crystal structures.

Appendix A

Crystal Structure Evolution and Notable Thermal Expansion in Hybrid Perovskites Formamidinium Tin Iodide and Formamidinium Lead Bromide

The temperature-dependent structure evolution of the hybrid halide perovskite compounds, formamidinium tin iodide (FASnI₃, FA⁺ = CH[NH₂]₂⁺) and formamidinium lead bromide (FAPbBr₃) has been monitored using high-resolution synchrotron X-ray powder diffraction between 300 K and 100 K. The data are consistent with a transition from cubic $Pm\bar{3}m$ (#221) to tetragonal $P4/mbm$ (#127) for both materials upon cooling; this occurs for FAPbBr₃ between 275 K and 250 K, and for FASnI₃ between 250 K

The contents of this chapter have substantially appeared in Reference [112]. Reproduced with permission from: E. C. Schueller, G. Laurit, D. H. Fabini, C. C. Stoumpos, M. G. Kanatzidis, and R. Seshadri, Crystal Structure Evolution and Notable Thermal Expansion in Hybrid Perovskites Formamidinium Tin Iodide and Formamidinium Lead Bromide *Inorg. Chem.* 57, 2 (2017) 695–701. Copyright 2019 American Chemical Society

and 225 K. Upon further cooling, between 150 K and 125 K, both materials undergo a transition to an orthorhombic $Pnma$ (#62) structure. The transitions are confirmed by calorimetry and dielectric measurements. In the tetragonal regime, the coefficients of volumetric thermal expansion of FASnI₃ and FAPbBr₃ are among the highest recorded for any extended inorganic crystalline solid, reaching 219 ppm K⁻¹ for FASnI₃ at 225 K. Atomic displacement parameters of all atoms for both materials suggest dynamic motion is occurring in the inorganic sublattice due to the flexibility of the inorganic network and dynamic lone pair stereochemical activity on the B -site. Unusual pseudo-cubic behavior is displayed in the tetragonal phase of the FAPbBr₃, similar to that previously observed in FAPbI₃.

A.1 Introduction

Hybrid halide perovskites (formula ABX_3 , where A is an organic cation, B is a divalent metal such as Sn or Pb, and X is a halide anion) have been the subject of renewed scientific interest since the first hybrid perovskite-based photovoltaic (PV) device in 2009. [113] This interest is due to their useful optoelectronic properties such as strong photoluminescence and long carrier lifetimes [114, 115] and potential as high performance, low cost PV absorbers. Formamidinium lead iodide (FAPbI₃) is a component of the highest performing perovskite solar cells with power conversion efficiencies above 20% [116, 117]. While there has been much research focused on improving device performance, less is known about the structure evolution of these materials. Detailed understanding of the crystal structure could provide strong insight into the observed properties such as low recombination rates [118, 119] and high defect tolerance [120, 121] that lead to high photovoltaic performance in the hybrid halide

perovskites.

Diffraction studies on the halide perovskites indicate that the materials usually distort from cubic to tetragonal to orthorhombic (and occasionally further to rhombohedral or monoclinic) upon cooling, following simple perovskite tilt systems [122]. CsSnI_3 transitions from $Pm\bar{3}m$ to $P4/mbm$ to $Pnma$ upon cooling from 500 K to 300 K [123], while MAPbI_3 ($\text{MA} = \text{CH}_3\text{NH}_3$) transitions from $Pm\bar{3}m$ to $I4/mcm$ to $Pnma$ upon cooling from 350 K to 100 K [124]. Materials with more flexibility in the inorganic lattice and enhanced lone pair activity such as MAPbCl_3 can undergo more complex phase transitions; for example, the low temperature ordered phase of MAPbCl_3 is $Pnma$ but with highly distorted octahedra, not the simple tilt phase that would be expected for a more traditional perovskite [125]. A recent structural study on FAPbI_3 discovered that the material has one of the largest coefficients of volumetric thermal expansion (α_v) of any extended crystalline solid, 203 ppm K^{-1} at 274 K. [126] FAPbI_3 also displays unusual reentrant behavior of a pseudo-cubic phase at low temperature; the phase transitions upon cooling go from $Pm\bar{3}m$ to $P4/mbm$ to pseudo-cubic $P4/mbm$, indicating complex interactions in this regime [126]. Locally, total scattering analysis using the pair distribution function technique on hybrid perovskites has revealed a highly flexible inorganic network with large local distortions among the $B - X$ octahedra in addition to dynamic lone pair stereochemical activity at high temperatures [23, 127–130].

We study herein the related compounds formamidinium tin iodide (FASnI_3) and formamidinium lead bromide (FAPbBr_3) in order to provide a more complete picture of the hybrid halide perovskite family and uncover trends that could lead to a deeper understanding of the class as a whole and possibly to a more rational design of high performance photovoltaic and optoelectronic materials. We build on what has already

been reported in the literature [131] with the use of high resolution synchrotron data to elucidate subtle structural changes that may have a large impact on the observed properties. We have determined the first phase transition upon cooling from room temperature to be cubic $Pm\bar{3}m$ to tetragonal $P4/mbm$ between 225 K and 250 K for FASnI_3 and between 250 K and 275 K for FAPbBr_3 . A further phase transformation to orthorhombic $Pnma$ occurs between 125 K and 150 K for both materials. We have corroborated these phase transitions with calorimetry and dielectric measurements. FASnI_3 has an even higher value of α_v in the tetragonal phase than FAPbI_3 of 219 ppm K^{-1} at 225 K compared to 203 ppm K^{-1} at 274 K for FAPbI_3 [126]. This presents an important engineering consideration for the incorporation of these materials in photovoltaic devices operating at various temperatures as relatively large volume changes are likely to occur over the operating temperature range of the device (at 300 K, α_v for FASnI_3 is still high at 174 ppm K^{-1}).

A.2 Experimental Methods

Formamidinium tin iodide (FASnI_3) and formamidinium lead bromide (FAPbBr_3) were prepared by a modification of previously reported procedures [131] which has been described in detail in Laurita *et al.* [23]. High resolution synchrotron powder X-ray diffraction (XRD) data were collected at 25 K intervals from 90 K to 300 K using beamline 11-BM at the Advanced Photon Source (APS), Argonne National Laboratory with a wavelength of 0.4592 \AA . 20 mg of ground sample was packed and sealed into a 0.5 mm OD Kapton capillary. Le Bail and Rietveld analyses were performed using the GSAS software suite [132] with the EXPGUI interface [133]. Crystal structures were visualized using the VESTA software suite [42]. Differential scanning calorimetry

(DSC) was performed on approximately 5 mg samples under a nitrogen atmosphere from 100 K to 300 K on a TA Instruments DSC Q2000 at rates of 5 and 10 degrees per minute. Dielectric measurements were performed in a Quantum Design PPMS DynaCool from 300 K to 1.8 K with an Andeen-Hagerling AH 2700A capacitance bridge for capacitance and loss measurements. Dielectric permittivity values were calculated from a flat plate capacitor model. Pellets for dielectric measurements were prepared by grinding a sample of material and pressing to 4 tons in a 6 mm cylindrical die (around 0.3 GPa) to obtain around 1.5 mm thick pellets. Electrodes were applied via low temperature indium soldering.

A.3 Results and Discussion

The structural evolution of FASnI_3 and FAPbBr_3 with temperature was analyzed from approximately 300 K to 100 K using X-ray diffraction data, and relevant structural parameters are tabulated in Tables A.1 and A.2. Phase transitions were determined by analysis of Bragg peak splitting and emergence. This work focuses on the inorganic sublattice, as dynamic disorder on the *A*-site and the smaller electron count of the organic cation add uncertainty when trying to assign *A*-site orientations from X-ray diffraction. Space groups were assigned by examining the “simple” octahedral tilt systems from the $Pm\bar{3}m$ cubic perovskite as enumerated by Howard and Stokes, [122] and all patterns were indexed well by one of these space groups. For data near phase transitions where the space group was somewhat ambiguous, fits to both space groups were performed and the fit with the lowest R-value was chosen. In order to determine whether the structure was actually lower symmetry but with a pseudo-symmetric unit cell, as has been suggested for these types of materials [131], Bragg peak width

analysis was performed on low-angle peaks and compared to peak widths of a known high symmetry structure, cubic FAPbI₃ with the space group $Pm\bar{3}m$, in which the only sources of broadening are instrumental resolution and sample size/strain, not overlapping peaks. In all cases, the peak widths were equal on the order of the resolution of the instrument. Because there was no detectable peak broadening or splitting, the higher symmetry space groups were retained.

The room temperature crystal structure of both materials is best fit by the cubic $Pm\bar{3}m$ perovskite structure, in agreement with findings from the original work on FASnI₃ [134] and single crystal work from Dang *et al.* [135] for FASnI₃ and several reports [136, 137] for FAPbBr₃. The FAPbBr₃ transitions between 275 K and 250 K to a phase described by tetragonal $P4/mbm$ with FASnI₃ following between 250 K and 225 K. Upon further cooling, both materials distort to an orthorhombic $Pnma$ phase between 150 K and 125 K. Some groups have reported a space group of pseudo-cubic $Amm2$ for FASnI₃ at 300 K [131, 138, 139], which has the same Bragg peak positions as $Pm\bar{3}m$ but with the ability to orient the asymmetric FA cations. However, $Amm2$ would have multiple overlapping peaks at each Bragg position, which was not evident upon visual inspection. In order to quantitatively compare the two structure determinations, we performed a fit to this space group which resulted in an R_{wp} of 14.59% at 300 K versus 10.27% for $Pm\bar{3}m$ from high resolution synchrotron powder diffraction. Because of the lower symmetry, the $Amm2$ phase has more refinable parameters than $Pm\bar{3}m$. Therefore, a significantly worse R_{wp} value for $Amm2$ than the $Pm\bar{3}m$ phase is probably due to difficulty assigning electron density to overlapping peaks. This, in combination with previously described peak width analysis of the (100) peak, indicates that the best fit to our data at room temperature is a $Pm\bar{3}m$ phase, although it is possible that other techniques that are better suited to looking at the formamidinium

orientations could improve on this assignment. Additionally, at low temperatures and applied electric fields DFT calculations suggest ordering of the *A*-site cation could occur, [140] but these conditions were not probed by our experiments. The locations of the phase transitions are examined by DSC, shown in Figure A.1(a) and (b). The high temperature phase transitions in both materials appear to be second order, while the low temperature transitions are accompanied by multiple peaks in the DSC, suggesting a complex cascade of phase transitions. Interestingly, the transition from tetragonal to orthorhombic in FASnI_3 appears more pronounced upon heating than upon cooling, shown in Figure A.1(a). This suggests that there may be multiple pathways for forming the low temperature orthorhombic state but there is a more deterministic transition back to the tetragonal phase. The phase transitions can be seen in the X-ray diffraction data as emergence of new peaks upon cooling as shown in Figure A.1(c) and (d), reflecting a lowering of the symmetry, with peaks appearing in the same temperature ranges as the expected phase transitions. However, we were able to resolve and refine only one low temperature phase transition from the XRD data.

Rietveld refinement fits to the XRD data are shown in Figure A.2. The fits were performed modeling the FA as a spherical atom with the same X-ray scattering power (Mn) for simplicity. This assumption is reasonable considering that in both compounds the FA has only around 10% of the total electrons, which means it has minimal scattering power, as the scattering power scales with the square of the electron density. However, because of this and dynamic disorder, the refined atomic displacement parameters (ADPs) on the cation *A*-site are large.

Crystal structures throughout the phase evolution are shown in Figure A.3 with ADPs shown at 50% probability ellipsoids. The halide ADPs are highly anisotropic, with motion occurring orthogonal to the *B* – *X* bond, and decrease in size upon cooling.

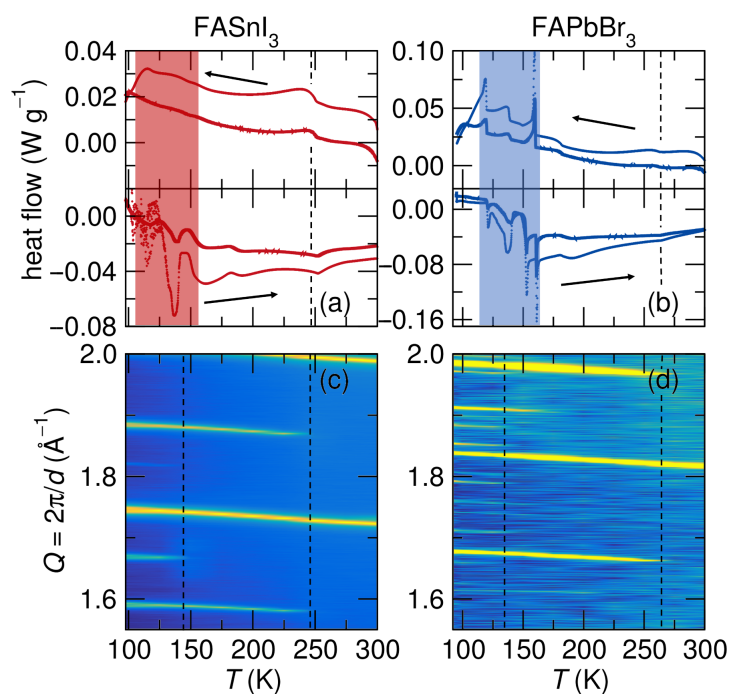


Figure A.1: DSC from 100 K to 300 K confirms the presence of phase transitions for (a) FASnI_3 and (b) FAPbBr_3 . The arrows indicate cooling and heating ramps. XRD data performed in the same temperature range for (c) FASnI_3 and (d) FAPbBr_3 . Phase transitions upon cooling are signaled by the development of new peaks in the pattern, indicating a lowering of symmetry in the crystal structure. XRD patterns were taken at 25 K intervals and interpolated in between. Dashed lines are shown at the emergence of new XRD peaks to compare phase transition temperatures from DSC and XRD. Due to the complexity of the low temperature transition(s) in DSC, the regions of interest are shaded.

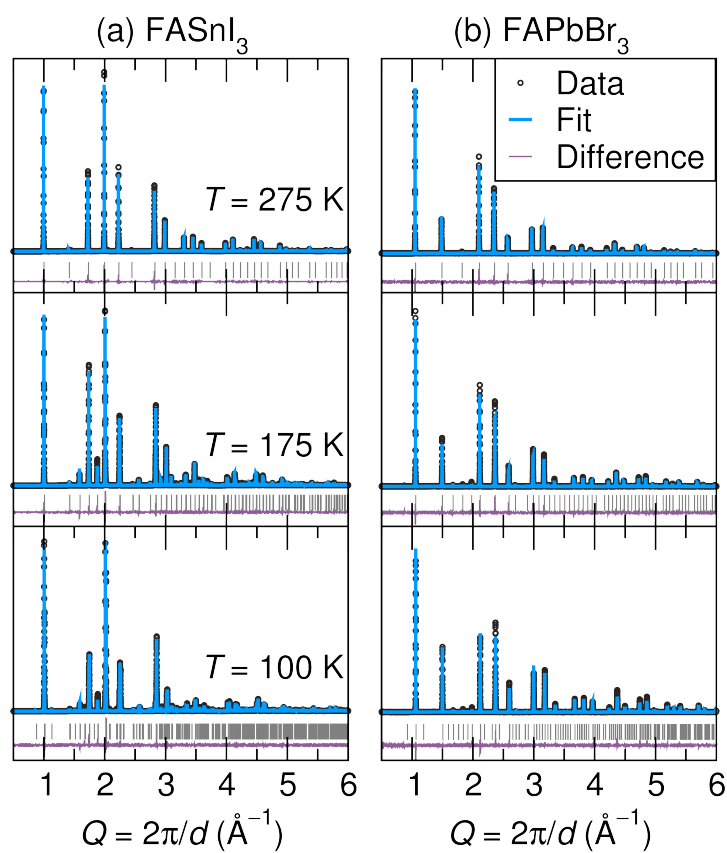


Figure A.2: Rietveld fits to synchrotron XRD data for (a) FASnI_3 and (b) FAPbBr_3 . The data at 275 K is best fit to a cubic $Pm\bar{3}m$ phase, the 175 K data to a tetragonal $P4/mbm$ phase, and the 100 K data to an orthorhombic $Pnma$ phase for both samples.

Table A.1: Crystallographic Data for FASnI_3

Empirical Formula Formula Weight (g mol^{-1})	$\text{CH}(\text{NH}_2)_2\text{SnI}_3$ 544.49		
Source	11-BM Synchrotron		
Wavelength (\AA)	0.4592		
Temperature (K)	100	175	275
Crystal System	Orthorhombic	Tetragonal	Cubic
Space Group (No.)	$Pnma$ (62)	$P4/mbm$ (127)	$Pm\bar{3}m$ (221)
a (\AA)	8.81749(8)	8.86227(2)	6.30961(1)
b (\AA)	12.41641(7)	/	/
c (\AA)	8.8578(1)	6.24892(2)	/
V (\AA^3)	969.773(9)	490.789(3)	251.1930(6)
Z	4	2	1
d -space range (\AA^{-1})	0.888 – 7.211	0.891 – 6.267	0.892 – 6.310
χ^2	9.869	3.672	4.005
R_p (%)	11.85	7.69	7.83
R_{wp} (%)	17.73	10.67	11.03

Table A.2: Crystallographic Data for FAPbBr_3

Empirical Formula Formula Weight (g mol^{-1})	$\text{CH}(\text{NH}_2)_2\text{PbBr}_3$ 491.98		
Source	11-BM Synchrotron		
Wavelength (\AA)	0.4592		
Temperature (K)	100	175	275
Crystal System	Orthorhombic	Tetragonal	Cubic
Space Group (No.)	$Pnma$ (62)	$P4/mbm$ (127)	$Pm\bar{3}m$ (221)
a (\AA)	8.37433(9)	8.41525(5)	5.98618(2)
b (\AA)	11.8609(1)	/	/
c (\AA)	8.38073(9)	5.94735(8)	/
V (\AA^3)	832.436(9)	421.170(3)	214.511(3)
Z	4	2	1
d -space range (\AA^{-1})	0.888 – 6.844	0.892 – 5.950	0.892 – 5.986
χ^2	1.958	1.400	1.397
R_p (%)	13.27	11.42	11.37
R_{wp} (%)	17.40	14.13	14.09

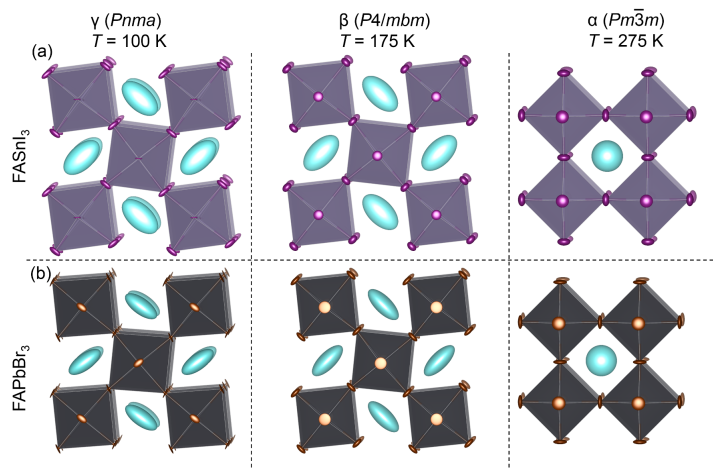


Figure A.3: Structural evolution of (a) FASnI_3 and (b) FAPbBr_3 with temperature. Atomic displacement parameters shown at 50% probability ellipsoids. The halides have highly anisotropic atomic displacement parameters, with motion orthogonal to the $B - X$ bond as observed in the literature [23, 129] reflecting dynamic octahedral tilting as well as possible intra-octahedral distortions.

These remain anisotropic for both FASnI_3 and FAPbBr_3 at low temperatures, indicating dynamic local disorder and distortions of the octahedra, as seen in the literature [23, 127–130].

The ADPs on the B -site (Sn and Pb) are also large, further hinting at the presence of local disorder in the materials. The Sn ADP is consistently larger than that of the Pb, as seen in Figure A.4(a). This trend aligns with the expected effects of lone pair stereochemical activity, which is predicted to be stronger for Sn^{2+} than Pb^{2+} due to deeper ns^2 levels in lead [23, 128, 141]. While the effects of lone pair stereochemical activity at elevated temperatures in these materials, labeled *emphanisis* in the chalcogenide literature [142–144], are not correlated enough to induce an ordered distortion visible in the average structure diffraction pattern, the combination of anisotropic halide ADPs and elevated B -site ADPs in the high temperature phase hint at local dynamic distortions, which have been observed previously in tin and lead perovskites [126, 128, 145, 146]. In addition to thermally activated lone pair activity, halide perovskites are known to

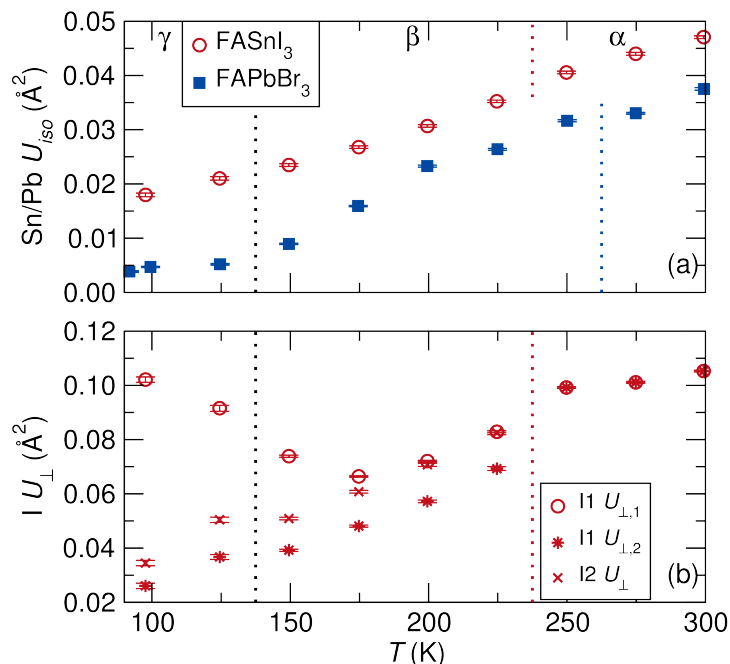


Figure A.4: (a) Isotropic atomic displacement parameters (ADPs) for the B ion in the perovskites. The value for Sn is consistently larger than for Pb due to enhanced dynamic lone pair stereochemical activity. (b) Anisotropic halide ADP terms perpendicular to the $B - X$ bonds show expected behavior upon cooling for the iodide aside from one component which increases upon cooling in the orthorhombic phase, an indication of static disorder along that direction. However, no clear trend appears in the bromide (bromide ADPs not shown for clarity).

have high flexibility within the inorganic octahedral network [128, 129, 145], allowing for local octahedral tilting and contributing to the anisotropy in halide ADPs and elevated ADPs in all species. The monotonic decrease in size for all ADPs upon cooling suggests that the disorder is dynamic and thermally activated, rather than static.

FASnI_3 and FAPbBr_3 have remarkably high coefficients of volumetric thermal expansion for crystalline solids. It was recently found that FAPbI_3 has a high α_v of 203 ppm K^{-1} at 274 K [126], but FASnI_3 has an even higher value of 219 ppm K^{-1} at 225 K as seen in Figure A.5(a). While this must be taken into consideration for solar device performance, as this manifests in volume changes in the material over the normal operating temperature range, the novelty of one of the highest values of α_v yet

seen in a crystalline solid is exciting.

Another odd feature in the structural evolution of these perovskites is seen in the particulars of the lattice parameters upon cooling. FASnI₃ exhibits expected trends in lattice parameters, but in FAPbBr₃ unusual behavior is displayed in the tetragonal phase, as seen in Figure A.5(c). The ratio of $\tilde{a} = a/\sqrt{2}$ to $\tilde{c} = c$ is curiously close to 1 throughout the tetragonal phase, only increasing again at the orthorhombic phase transition. The normalized lattice parameters never deviate more than 0.005 Å from each other in the tetragonal phase, indicating the crystal maintains a nearly cubic unit cell, while in FASnI₃ the deviations reach over 0.02 Å in the tetragonal phase. Similar pseudo-cubic behavior was observed in FAPbI₃[126]; however, in FAPbI₃ it is reentrant in the tetragonal γ -phase, and no transition was fully completed to an orthorhombic structure by 100 K, whereas FAPbBr₃ does undergo a tetragonal to orthorhombic transition after further cooling. This unusual behavior happens in both formamidinium lead halide perovskites studied so far but not in the tin analogue, so it could be that the lead is somehow contributing to complex disorder in the tetragonal phase. At first glance, this would appear to be a size effect because Pb²⁺ is larger than Sn²⁺, but FASnI₃ has larger lattice parameters than FAPbBr₃. This suggests the presence of a more subtle effect, such as ionicity of $B - X$ bonds impacting interactions with the formamidinium.

Figure A.4(b) shows the anisotropic ADP components for the halides in the direction perpendicular to the bond. The size of most iodine ADP components consistently decrease with temperature as expected. The bromine ADPs, on the other hand, show no clear trends with temperature, another indicator of disorder in the material that is not fully captured by a crystallographic model.

Dielectric measurements were performed on FAPbBr₃ to obtain information about molecular cation motion in the material as shown in Figure A.6. Due to the semicon-

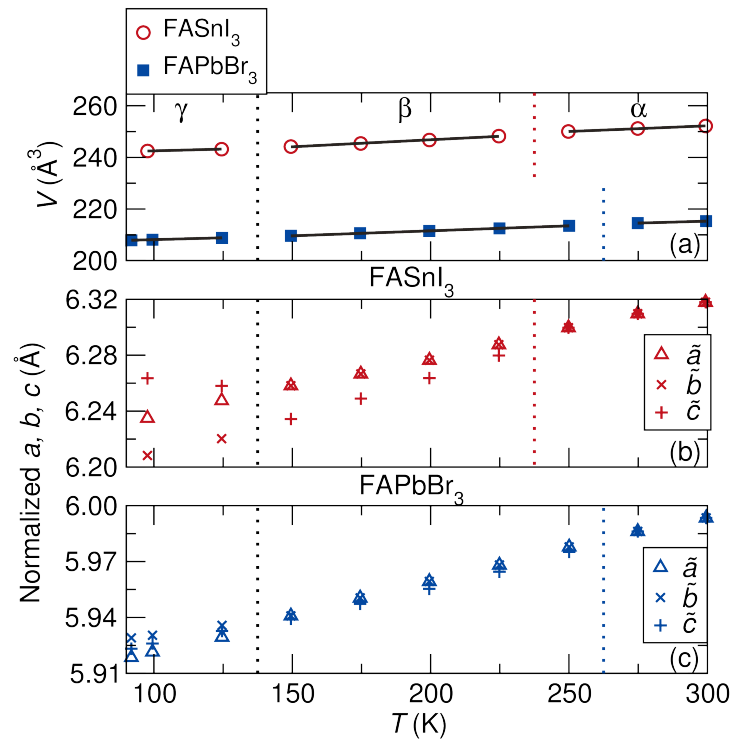


Figure A.5: (a) Volumetric expansion in the materials shows that FASnI_3 has an extremely high α_v of 219 ppm K^{-1} at 225 K. Normalized (pseudo-cubic) lattice parameters as a function of temperature in FASnI_3 (b) and FAPbBr_3 (c) show unusual behavior in the tetragonal phase of FAPbBr_3 . Error bars are smaller than the markers and are omitted for clarity.

ducting nature of the sample, electronic conduction is too great above 200 K to extract meaningful dielectric information about the cubic to tetragonal phase transition. The smaller band gap of FASnI₃ precluded the acquisition of dielectric properties using the capacitance method. Compared to similar materials such as MAPbI₃ and FAPbI₃ [147], FAPbBr₃ does not have an abrupt freezing of dipole rotation, indicated by a sudden drop in the real portion of the dielectric permittivity. While the magnitude of the real part of the permittivity is similar to that of MAPbBr₃ at low temperatures, the shape of the graph is far different, missing both the sudden drop as mentioned before and the upturn upon cooling at temperatures higher than the drop. [148] It appears as though FAPbBr₃ undergoes a more continuous slowing of molecular reorientation, possibly due to the smaller lattice parameters of FAPbBr₃, which could limit the motion of the formamidinium cation even at high temperatures, although it is possible that characteristic features could appear at temperatures above 200 K. The feature associated with the tetragonal to orthorhombic phase transition occurs in the same temperature region as phase transition signatures from DSC and XRD, further confirming the location of the phase transition.

We have utilized synchrotron XRD data to analyze the structure evolution of FASnI₃ and FAPbBr₃ with temperature from 300 K to 100 K. We observe that both materials undergo phase transformations from cubic $Pm\bar{3}m$ to $P4/mbm$ to $Pnma$ upon cooling and corroborate these transitions by calorimetry. A high value for α_v is observed in both materials, particularly in FASnI₃, giving it possibly the highest value of any extended crystalline solid near ambient temperatures. Large ADPs on the *B*-site cations along with highly anisotropic halide ADPs provide more evidence for local distortions and support observed *emphanisis* in tin and lead perovskites. Despite the impressive photovoltaic performance of hybrid halide perovksites, the large coefficient of volumetric

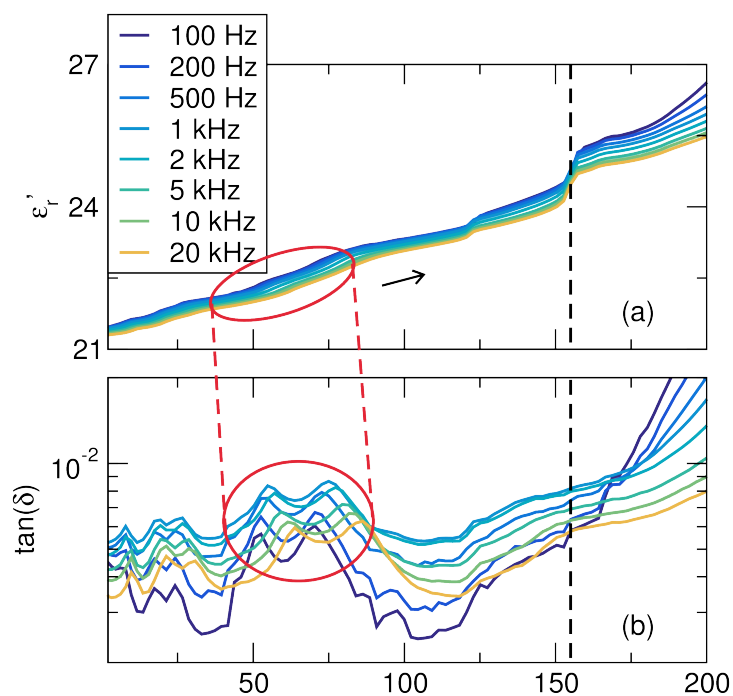


Figure A.6: (a) The real part of the relative permittivity, ϵ_r' , upon heating for FAPbBr_3 at various frequencies. (b) The loss tangent for FAPbBr_3 upon heating. The frequency disperse (spread over temperature) peaks in the loss tangent, indicated by a red ellipse, show the glassy freeze-out of the molecule, characterized by resonance between the dielectric relaxation process and the probe frequency. The absence of a sharp drop in the dielectric constant indicates dipole reorientation of the formamidinium is relatively hindered throughout the temperature range sampled. The dashed line shows the feature associated with the tetragonal to orthorhombic phase transitions and aligns with the temperature range from XRD and DSC.

thermal expansion presents a significant engineering challenge that must be taken into consideration when utilizing these materials in devices.

Appendix B

**Structural evolution and skyrmionic
phase diagram of the lacunar spinel**

GaMo₄Se₈

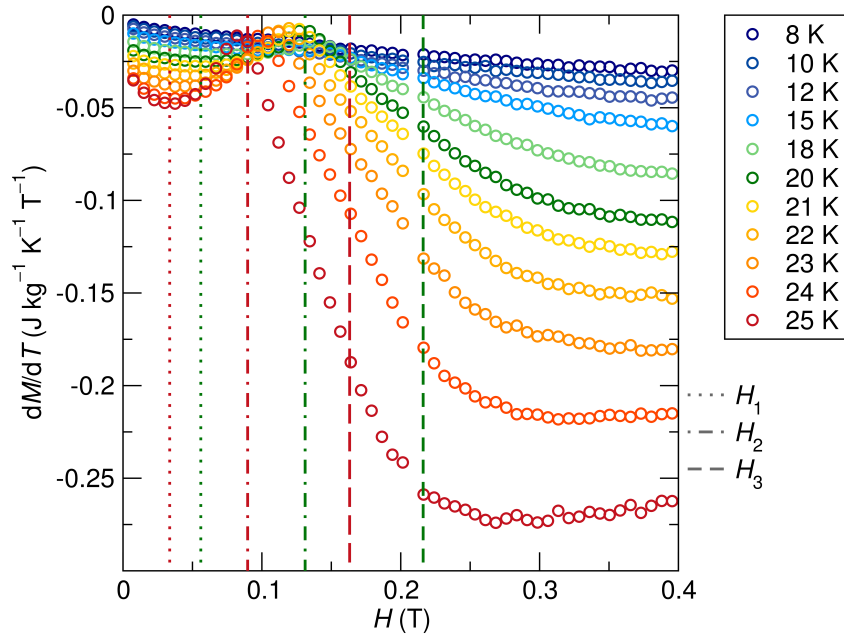


Figure B.1: dM/dT vs field data at various temperatures. Some characteristic locations of the three magnetic transitions with field are shown over the data.

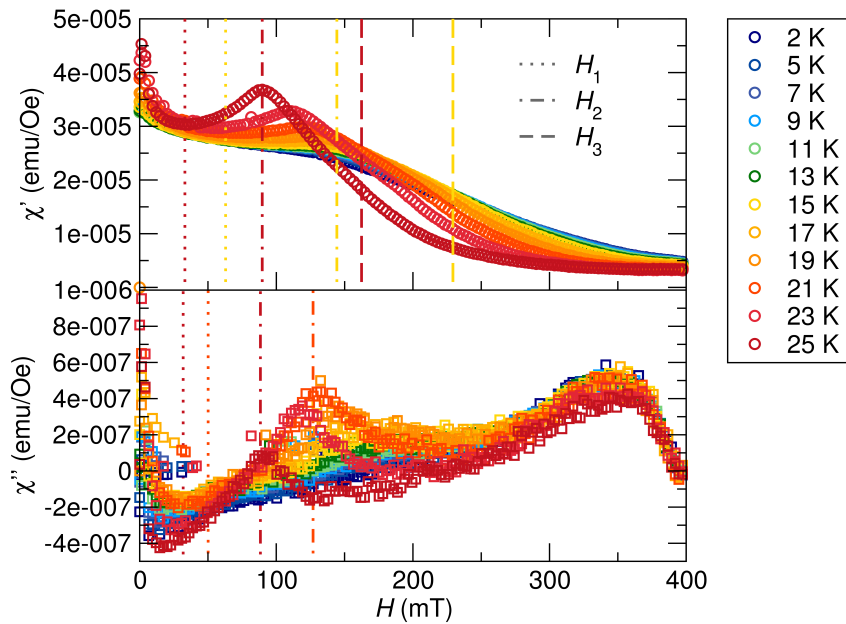


Figure B.2: AC χ' and χ'' data at various temperatures. Some characteristic locations of the three magnetic transitions with field are shown over the data. Only the first two transitions can be elucidated from the χ'' data.

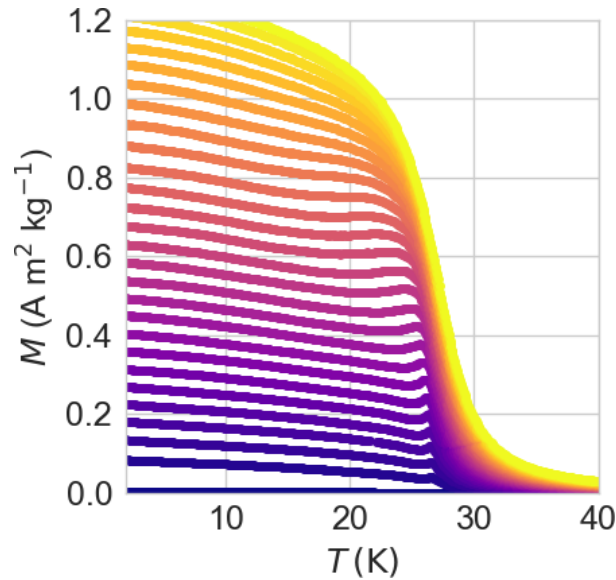


Figure B.3: Magnetization vs temperature data at various applied fields. This data was used to generate the magnetoentropic map by taking the derivative of magnetization with respect to temperature.

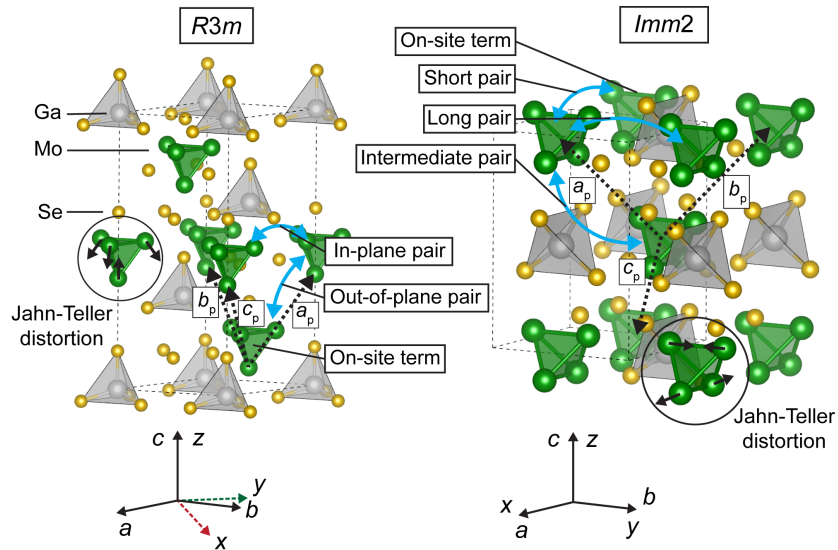


Figure B.4: Structure of the $R3m$ and $Imm2$ phases of GaMo_4Se_8 in their conventional unit cells, along with the primitive cell axes (a_p , b_p , c_p). The cartesian coordinate system for each phase further defines the axes used to define the magnetic Hamiltonian. Finally, the symmetrically distinct on-site and pair interactions appearing in the magnetic Hamiltonian of each phase are shown.

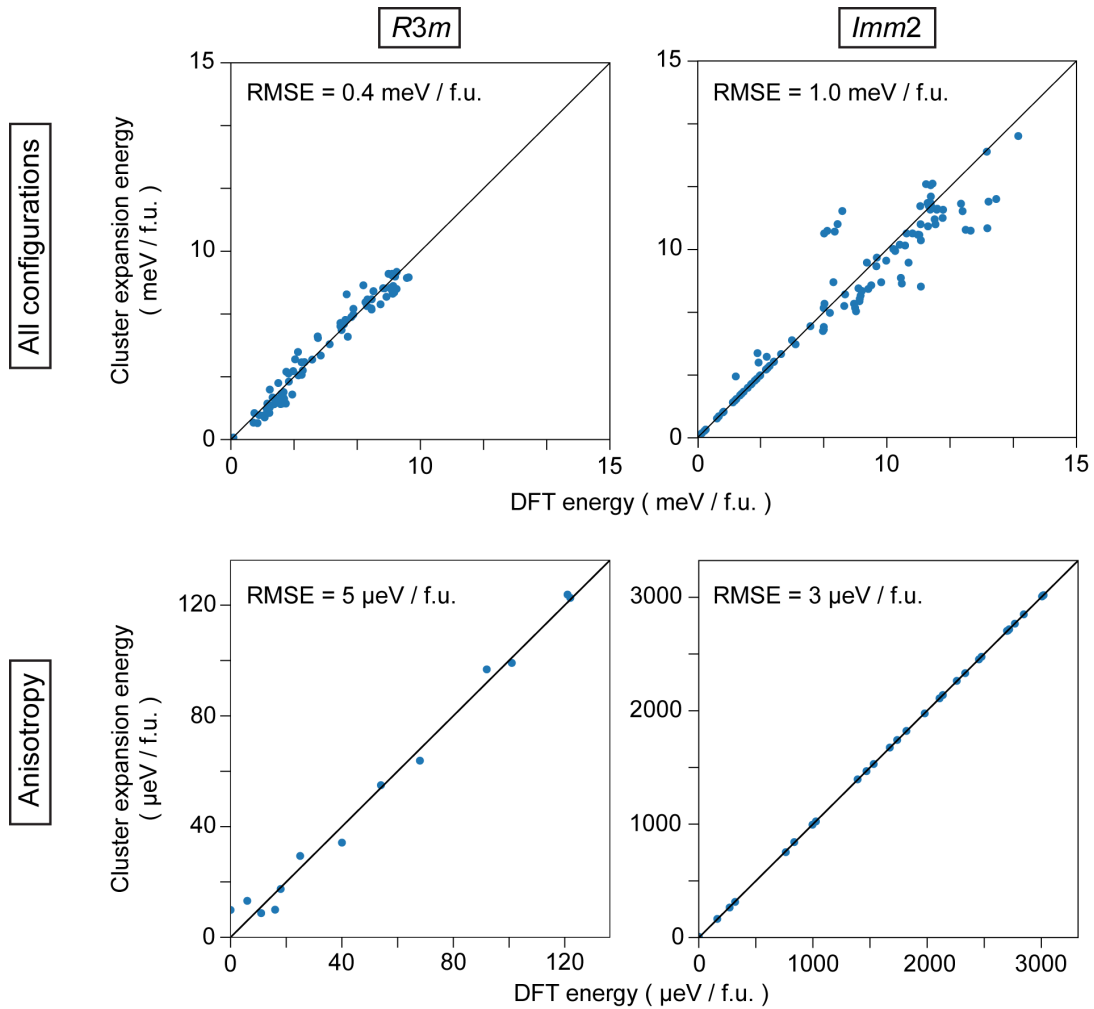


Figure B.5: Magnetic cluster expansion fitting error for the $R3m$ and $Imm2$ phases of GaMo_4Se_8 . Each point denotes the energy of a symmetrically distinct spin configuration, as computed using DFT and the fitted cluster expansion Hamiltonian. The magnetocrystalline anisotropy terms are fitted independently to account for the difference in energy scale between these terms and spin-spin interactions, as described in the main text.

Cluster type		Basis function	$J(\text{meV})$
On-site	ϕ_1^A	$\sqrt{2} 2, 0\rangle$	0.027(1)
$r = (0, 0, 0)$	ϕ_2^A	$-i(4, -3\rangle + 4, 3\rangle)$	-0.008(1)
(1 equiv.)	ϕ_3^A	$\sqrt{2} 4, 0\rangle$	-0.006(1)
Out-of-plane	ϕ_7^E	$\frac{\sqrt{2}}{3} 1, 1; 0, 0\rangle$	1.38(6)
$r_1 = (0, 0, 0)$	ϕ_8^D	$\frac{i}{3}(1, 1; 1, 1\rangle - 1, 1; 1, -1\rangle)$	-0.06(9)
$r_2 = (-1, 0, 0)$	ϕ_9^A	$-\frac{i}{3}(1, 1; 2, 1\rangle + 1, 1; 2, -1\rangle)$	0.1(2)
(3 equiv.)	ϕ_{10}^A	$\frac{\sqrt{2}}{3} 1, 1; 2, 0\rangle$	0
	ϕ_{11}^A	$\frac{1}{3}(1, 1; 2, 2\rangle + 1, 1; 2, -2\rangle)$	0.6(3)
In-plane	ϕ_{12}^E	$\frac{\sqrt{2}}{3} 1, 1; 0, 0\rangle$	1.06(6)
$r_1 = (0, 0, 0)$	ϕ_{13}^D	$(\frac{1}{6} + \frac{i}{\sqrt{12}}) 1, 1; 1, 1\rangle +$	0.3(1)
$r_2 = (-1, 0, 1)$		$(\frac{1}{6} - \frac{i}{\sqrt{12}}) 1, 1; 1, -1\rangle$	
(3 equiv.)	ϕ_{14}^D	$\frac{-i\sqrt{2}}{3} 1, 1; 1, 0\rangle$	0
	ϕ_{15}^A	$\frac{\sqrt{2}}{3} 1, 1; 2, 0\rangle$	0
	ϕ_{16}^A	$(\frac{1}{\sqrt{12}} - \frac{i}{6}) 1, 1; 2, 1\rangle -$	0
		$(\frac{1}{\sqrt{12}} + \frac{i}{6}) 1, 1; 2, -1\rangle$	
	ϕ_{17}^A	$(\frac{1}{6} - \frac{i}{\sqrt{12}}) 1, 1; 2, 2\rangle +$	0
		$(\frac{1}{6} + \frac{i}{\sqrt{12}}) 1, 1; 2, -2\rangle$	

Table B.1: Magnetic Hamiltonian for the $R3m$ phase of GaMo₄Se₈, consisting of basis functions ϕ and parametrized interaction strengths J . Cluster site coordinates and basis functions are given for the reference cluster, in lattice coordinates with respect to the primitive lattice vectors (a_p, b_p, c_p) given in Supplementary Figure 3. The number of equivalents for each cluster refers to the number of symmetrically-equivalent clusters of this type per primitive cell. Basis functions are defined in terms of spherical harmonics $|l, m\rangle = \sqrt{4\pi}Y_m^l(\phi, \theta)$ for the on-site terms and Clebsch–Gordan functions $|l_1, l_2; L, M\rangle = 4\pi \sum_{m_1, m_2} c_{m_1, m_2, M}^{l_1, l_2, L} Y_{m_1}^{l_1}(\phi_1, \theta_1) Y_{m_2}^{l_2}(\phi_2, \theta_2)$ for pair clusters (r_1, r_2). Spin angles (ϕ, θ) are given in spherical coordinates with respect to the global coordinate system defined in Supplementary Figure 4. Basis function superscripts denote whether the interaction corresponds to exchange (E), DMI (D), or anisotropy (A). Parenthesis in the J vector components denote uncertainty in the last digit.

Cluster type		Basis function	$J(\text{meV})$
On-site $r = (0, 0, 0)$ (1 equiv.)	ϕ_1^A	$\sqrt{2} 2, 0\rangle$	0.313(1)
	ϕ_2^A	$ 2, 2\rangle + 2, -2\rangle$	0.551(1)
	ϕ_3^A	$ 4, 4\rangle + 4, -4\rangle$	-0.003(1)
	ϕ_4^A	$ 4, 2\rangle + 4, -2\rangle$	-0.002(1)
	ϕ_5^A	$\sqrt{2} 4, 0\rangle$	0
Short $r_1 = (0, 0, 0)$ $r_2 = (0, -1, -1)$ (1 equiv.)	ϕ_{10}^E	$\sqrt{2} 1, 1; 0, 0\rangle$	0.93(7)
	ϕ_{11}^D	$ 1, 1; 1, 1\rangle + 1, 1; 1, -1\rangle$	-0.18(9)
	ϕ_{12}^A	$ 1, 1; 2, -2\rangle + 1, 1; 2, -2\rangle$	-0.2(2)
	ϕ_{13}^A	$\sqrt{2} 1, 1; 2, 0\rangle$	-0.2(1)
Intermediate $r_1 = (1, 0, 0)$ $r_2 = (0, -1, -1)$ (4 equiv.)	ϕ_{14}^E	$\frac{\sqrt{2}}{4} 1, 1; 0, 0\rangle$	0.2(1)
	ϕ_{15}^D	$\frac{1}{4}(1, 1; 1, 1\rangle + 1, 1; 1, -1\rangle)$	0.3(2)
	ϕ_{16}^D	$\frac{i}{4}(1, 1; 1, 1\rangle - 1, 1; 1, -1\rangle)$	-0.1(1)
	ϕ_{17}^D	$\frac{-i\sqrt{2}}{4} 1, 1; 1, 0\rangle$	-0.3(2)
	ϕ_{18}^A	$\frac{1}{4}(1, 1; 2, 2\rangle + 1, 1; 2, -2\rangle)$	0.2(3)
	ϕ_{19}^A	$\frac{i}{4}(1, 1; 2, 2\rangle - 1, 1; 2, -2\rangle)$	-0.1(4)
	ϕ_{20}^A	$\frac{-1}{4}(1, 1; 2, 1\rangle - 1, 1; 2, -1\rangle)$	0.4(5)
	ϕ_{21}^A	$\frac{-i}{4}(1, 1; 2, 1\rangle + 1, 1; 2, -1\rangle)$	0.5(5)
	ϕ_{22}^A	$\frac{\sqrt{2}}{4} 1, 1; 2, 0\rangle$	0.1(1)
Long $r_1 = (1, 0, 0)$ $r_2 = (0, 0, -1)$ (1 equiv.)	ϕ_{23}^E	$\sqrt{2} 1, 1; 0, 0\rangle$	0.76(8)
	ϕ_{24}^D	$i(1, 1; 1, -1\rangle - 1, 1; 1, 1\rangle)$	0.24(9)
	ϕ_{25}^A	$ 1, 1; 2, 2\rangle + 1, 1; 2, -2\rangle$	-0.1(1)
	ϕ_{26}^A	$\sqrt{2} 1, 1; 2, 0\rangle$	0.1(1)

Table B.2: Magnetic Hamiltonian for the *Imm2* phase of GaMo₄Se₈, following the format given in the caption of Supplementary Table 1.

Appendix C

Factors Driving Crystallization in the Trirutile Structure

The machine learning model relied heavily on automatminer pipeline attributes. Here is specific information about every step of the pipeline.

Featurizing the matrix:

```
"autofeaturizer": AutoFeaturizer(preset="all")
```

```
List of feature libraries: cf.AtomicOrbitals(), cf.ElementProperty.from_preset("matminer")
("pymatgen"), cf.ElementProperty.from_preset("magpie"), cf.ElementProperty.from_preset("deml"),
cf.ElementFraction(), cf.Stoichiometry(), cf.TMetalFraction(), cf.BandCenter(), cf.ValenceOrbital(),
cf.YangSolidSolution(), cf.CationProperty.from_preset(preset_name='deml'), cf.OxidationStates.from
cf.ElectronAffinity(), cf.ElectronegativityDiff(), cf.IonProperty(), cf.Miedema()
```

```
pymatgen stats: ["minimum", "maximum", "range", "mean", "std_dev"]
```

```
magpie stats: ["minimum", "maximum", "range", "mean", "avg_dev", "mode"]
```

```
deml stats: ["minimum", "maximum", "range", "mean", "std_dev"]
```

Cleaning the data: "cleaner": DataCleaner()

If feature value missing (na) for over 3% of samples (or <3% of features available for sample), remove, remove duplicates

"reducer": FeatureReducer(reducers=('corr', 'tree'), tree_importance_percentile=0.99)

If features > 95% correlated, remove

Use a random forest to remove features that together sum to <1% of importance by weight

Reduction of 629 initial features to 46

Machine learning genetic algorithm parameters:

"learner": TPOTAdaptor(max_time_mins=720, max_eval_time_mins=20, scoring="f1"),

Then comes genetic algorithm: continues feature selection, chooses RFE to remove half of the features with ETC and gini importance, down to 23

'rfe', RFE(estimator=ExtraTreesClassifier(bootstrap=False, class_weight=None, criterion='gini', max_depth=None, max_features=0.35000000000000003, max_leaf_nodes=None, min_impurity_decrease=0.0, min_impurity_split=None, min_samples_leaf=1, min_samples_split=2, min_weight_fraction_leaf=0.0, n_estimators=100, n_jobs=None, oob_score=False, random_state=None, verbose=0, warm_start=False), n_features_to_select=None, step=0.3500000000, verbose=0)),

These are the RFE hyperparameters the genetic algorithm iterated over:

'sklearn.feature_selection.RFE': ('step': np.arange(0.05, 1.01, 0.05), 'estimator': ('sklearn.ensemble.ExtraTreesClassifier': ('n_estimators': [100], 'criterion': ['gini', 'entropy'], 'max_features': tree_max_features)

Then comes preprocessing - should we scale, normalize etc. The genetic algorithm

finds polynomial features to order 2 is best.

```
('polynomialfeatures', PolynomialFeatures(degree=2, include_bias=False, interaction_only=False)),
```

Finally we have the model, TPOT chooses between models like random forest, gradient boosting classifier, linear SVC, etc.

```
('extratreesclassifier', ExtraTreesClassifier(bootstrap=False, class_weight=None, criterion='entropy', max_depth=None, max_features=0.9500000000000002, max_leaf_nodes=None, min_impurity_decrease=0.0, min_impurity_split=None, min_samples_leaf=7, min_samples_split=1, min_weight_fraction_leaf=0.0, n_estimators=100, n_jobs=None, oob_score=False, random_state=None, verbose=0, warm_start=False))
```

These are the hyperparameters it iterates over and the acceptable ranges in the nested CV:

```
tree_estimators = [20, 100, 200, 500, 1000]
tree_max_features = np.arange(0.05, 1.01, 0.1)
tree_learning_rates = [1e-2, 1e-1, 0.5, 1.]
tree_max_depths = range(1, 11, 2)
tree_min_samples_split = range(2, 21, 3)
tree_min_samples_leaf = range(1, 21, 3)
tree_ensemble_subsample = np.arange(0.05, 1.01, 0.1)
```

We fit the same features and train/test split to other models using a grid search cross validation with a 5-fold stratified split to benchmark our model. Other models included a random forest, neural net, and support vector classifier (for the last two the features were scaled), but the original extra trees classifier had the best f_1 score on

both cross validation and test.

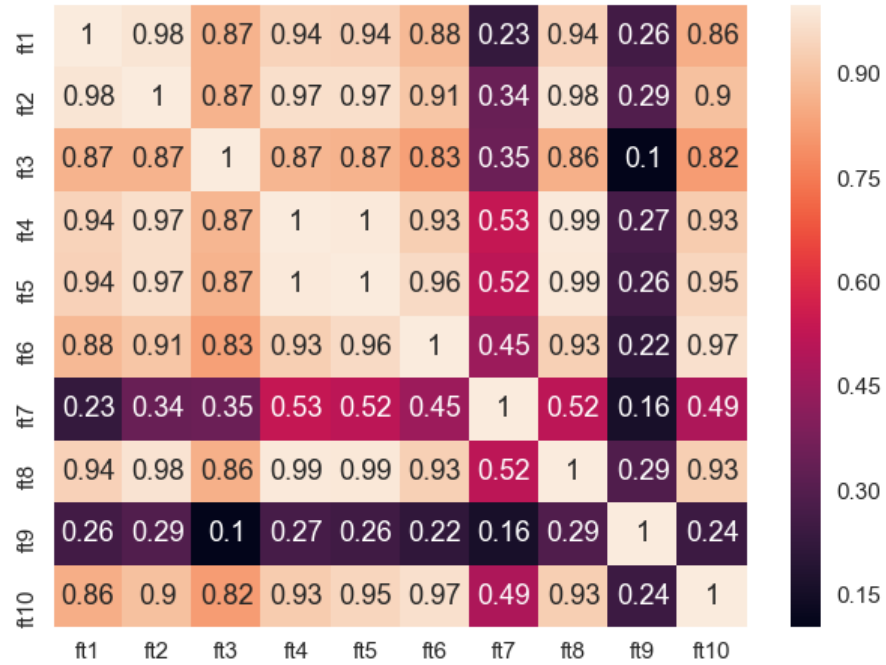


Figure C.1: A correlation matrix for the 10 most important features of the extra trees classifier shows that 7 of the top 10 features are highly correlated with the most important feature. This indicates a combination of geometry and bonding is the most important factor in understanding which compositions form in the trirutile structure.

Bibliography

- [1] See Supplemental Material at [URL will be inserted by publisher] for the structures used for DFT calculations in this work, as well as calculated band diagrams. .
- [2] R. Tomasello, E. Martinez, R. Zivieri, L. Torres, M. Carpentieri, and G. Finocchio. A Strategy for the Design of Skyrmion Racetrack Memories. *Sci. Rep.* **4** (2015) 6784. doi:[10.1038/srep06784](https://doi.org/10.1038/srep06784)
- [3] J. D. Bocarsly, R. F. Need, R. Seshadri, and S. D. Wilson. Magnetoentropic Signatures of Skyrmionic Phase Behavior in FeGe. *Phys. Rev. B* **97** (2018) 100404(R). doi:[10.1103/PhysRevB.97.100404](https://doi.org/10.1103/PhysRevB.97.100404)
- [4] D. A. Kitchaev, I. J. Beyerlein, and A. Van der Ven. Phenomenology of Chiral Dzyaloshinskii-Moriya Interactions in Strained Materials. *Phys. Rev. B* **98** (2018) 214414. doi:[10.1103/PhysRevB.98.214414](https://doi.org/10.1103/PhysRevB.98.214414)
- [5] M. Imada, A. Fujimori, and Y. Tokura. Metal–Insulator Transitions. *Rev. Mod. Phys.* **70** (1998) 1039–1263. doi:[10.1103/RevModPhys.70.1039](https://doi.org/10.1103/RevModPhys.70.1039)
- [6] A. Kapitulnik, S. A. Kivelson, and B. Spivak. Anomalous Metals: Failed Superconductors. *Rev. Mod. Phys.* **91** (2019) 011002. doi:[10.1103/RevModPhys.91.011002](https://doi.org/10.1103/RevModPhys.91.011002)
- [7] J. L. García-Muñoz, M. Suaaidi, J. Fontcuberta, and J. Rodríguez-Carvajal. Reduction of the Jahn-Teller Distortion at the Insulator-to-Metal Transition in Mixed Valence Manganites. *Phys. Rev. B* **55** (1997) 34. doi:[10.1103/PhysRevB.55.34](https://doi.org/10.1103/PhysRevB.55.34)
- [8] O. Toulemonde, F. Millange, F. Studer, B. Raveau, J.-H. Park, and C.-T. Chen. Changes in the Jahn-Teller Distortion at the Metal–Insulator Transition in CMR Manganites $(\text{Pr,Nd})_{0.7}(\text{Sr,Ca})_{0.3}\text{MnO}_3$. *J. Phys.: Condens. Matter* **11** (1999) 109. doi:[10.1088/0953-8984/11/1/009](https://doi.org/10.1088/0953-8984/11/1/009)
- [9] Z. Hiroi. Structural Instability of the Rutile Compounds and its Relevance to the Metal–Insulator Transition of VO_2 . *Progr. Solid State Chem.* **43** (2015) 47–69. doi:[10.1016/j.progsolidstchem.2015.02.001](https://doi.org/10.1016/j.progsolidstchem.2015.02.001)

- [10] J. P. Pouget, H. Launois, J. P. D’Haenens, P. Merenda, and T. M. Rice. Electron Localization Induced by Uniaxial Stress in Pure VO₂. *Phys. Rev. Lett.* **35** (1975) 873. doi:[10.1103/PhysRevLett.35.873](https://doi.org/10.1103/PhysRevLett.35.873)
- [11] L. K. Lamontagne, G. Laurita, M. Knight, H. Yusu, J. Hu, R. Seshadri, and K. Page. The Role of Structural and Compositional Heterogeneities in the Insulator-to-Metal Transition in Hole-Doped APd₃O₄ (A = Ca, Sr). *Inorg. Chem.* **56** (2017) 5158–5164. doi:[10.1021/acs.inorgchem.7b00307](https://doi.org/10.1021/acs.inorgchem.7b00307)
- [12] M. Shatnawi, E. S. Bozin, J. F. Mitchell, and S. J. L. Billinge. Nonpercolative Nature of the Metal-Insulator Transition and Persistence of Local Jahn-Teller Distortions in the Rhombohedral Regime of La_{1-x}Ca_xMnO₃. *Phys. Rev. B* **93** (2016) 165138. doi:[10.1103/PhysRevB.93.165138](https://doi.org/10.1103/PhysRevB.93.165138)
- [13] R. Pocha, D. Johrendt, B. Ni, and M. M. Abd-Elmeguid. Crystal Structures, Electronic Properties, and Pressure-Induced Superconductivity of the Tetrahedral Cluster Compounds GaNb₄S₈, GaNb₄Se₈, and GaTa₄Se₈. *J. Am. Chem. Soc.* **127** (2005) 8732–8740. doi:[10.1021/ja050243x](https://doi.org/10.1021/ja050243x)
- [14] S. Kawamoto, T. Higo, T. Tomita, S. Suzuki, Z. M. Tian, K. Mochizuki, A. Matsuo, K. Kindo, and S. Nakatsuji. Frustrated Magnetism in a Mott Insulator Based on a Transition Metal Chalcogenide. *J. Phys.: Conf. Ser.* **683** (2016) 012025. doi:[10.1088/1742-6596/683/1/012025](https://doi.org/10.1088/1742-6596/683/1/012025)
- [15] S. Bordacs, A. Butykai, B. G. Szigeti, J. S. White, R. Cubitt, A. O. Leonov, S. Widmann, D. Ehlers, H.-A. K. von Nidda, V. Tsurkan, A. Loidl, and I. Kezsmarki. Equilibrium Skyrmion Lattice Ground State in a Polar Easy-plane Magnet. *Sci. Rep.* **7** (2017) 7584. doi:<https://doi.org/10.1038/s41598-017-07996-x>
- [16] Y. Fujima, N. Abe, Y. Tokunaga, and T. Arima. Thermodynamically Stable Skyrmion Lattice at Low Temperatures in a Bulk Crystal of Lacunar Spinel GaV₄Se₈. *Phys. Rev. B* **95** (2017) 180410(R). doi:[10.1103/PhysRevB.95.180410](https://doi.org/10.1103/PhysRevB.95.180410)
- [17] K. Jodama, S. Shamoto, H. Harashina, J. Takeda, M. Sato, K. Kakurai, and M. Nishi. Electronic Structure of the Quasi Two-Dimensional Mott System BaCo_{1-x}Ni_xS₂. *J. Phys. Soc. Jpn.* **65** (1996) 1782–1786. doi:[10.1143/JPSJ.65.1782](https://doi.org/10.1143/JPSJ.65.1782)
- [18] D. Santos-Cottin, Y. Klein, P. Werner, T. Miyake, L. de’Medici, A. Gauzzi, R. P. S. M. Lobo, and M. Casula. Linear Behavior of the Optical Conductivity and Incoherent Charge Transport in BaCoS₂. *Phys. Rev. Materials* **2** (2018) 105001. doi:[10.1103/PhysRevMaterials.2.105001](https://doi.org/10.1103/PhysRevMaterials.2.105001)
- [19] Y. Klein, M. Casula, D. Santos-Cottin, A. Audouard, D. Vignolles, G. Fève, V. Freulon, B. Plaçais, M. Verseils, H. Yang, L. Paulatto, and A. Gauzzi.

- Importance of Nonlocal Electron Correlation in the BaNiS₂ Semimetal from Quantum Oscillations Studies. *Phys. Rev. B* **97** (2018) 075140. doi:[10.1103/PhysRevB.97.075140](https://doi.org/10.1103/PhysRevB.97.075140)
- [20] L. S. Martinson, J. W. Schweitzer, and N. C. Baenziger. Metal-Insulator Transitions in BaCo_{1-x}Ni_xS_{2-y}. *Phys. Rev. Lett.* **71** (1993) 125–128. doi:[10.1103/physrevlett.71.125](https://doi.org/10.1103/physrevlett.71.125)
- [21] R. L. Mozzi and B. E. Warren. The Structure of Vitreous Silica. *J. Appl. Cryst* **2** (1969) 164–172. doi:[10.1107/S0021889869006868](https://doi.org/10.1107/S0021889869006868)
- [22] S. J. L. Billinge. The Rise of the X-ray Atomic Pair Distribution Function Method: A Series of Fortunate Events. *Phil. Trans. R. Soc. A* **377** (2019) 20180413. doi:[10.1098/rsta.2018.0413](https://doi.org/10.1098/rsta.2018.0413)
- [23] G. Laurita, D. H. Fabini, C. C. Stoumpos, M. Kanatzidis, and R. Seshadri. Chemical Tuning of Dynamic Cation Off-Centering in the Cubic Phases of Hybrid Tin and Lead Halide Perovskites. *Chem. Sci.* **8** (2017) 5628–5635. doi:[10.1039/C7SC01429E](https://doi.org/10.1039/C7SC01429E)
- [24] A. O. Oliynyk, E. Antono, T. D. Sparks, L. Ghadbeigi, M. W. Gaultois, B. Meredig, and A. Mar. High-Throughput Machine-Learning-Driven Synthesis of Full-Heusler Compounds. *Chem. Mater.* **28** (2016) 7324–7331. doi:[10.1021/acs.chemmater.6b02724](https://doi.org/10.1021/acs.chemmater.6b02724)
- [25] G. Hautier, C. C. Fischer, A. Jain, T. Mueller, and G. Ceder. Finding Nature’s Missing Ternary Oxide Compounds Using Machine Learning and Density Functional Theory. *Chem. Mater.* **22** (2010) 3762–3767. doi:[10.1021/cm100795d](https://doi.org/10.1021/cm100795d)
- [26] L. Ward, A. Dunn, A. Faghaninia, N. E. R. Zimmermann, S. Bajaj, Q. Wang, J. H. Montoya, J. Chen, K. Bystrom, M. Dylla, K. Chard, M. Asta, K. Persson, G. J. Snyder, I. Foster, and A. Jain. Matminer: An Open Source Toolkit for Materials Data Mining. *Comput. Mater. Sci.* **152** (2018) 60–69. doi:[10.1016/j.commatsci.2018.05.018](https://doi.org/10.1016/j.commatsci.2018.05.018)
- [27] S. P. Ong, W. D. Richards, A. Jain, G. Hautier, M. Kocher, S. Cholia, D. Gunter, V. L. Chevrier, K. A. Persson, and G. Ceder. Python Materials Genomics (pymatgen): A Robust, Open-Source Python Library for Materials Analysis. *Comput. Mater. Sci.* **68** (2013) 314–319. doi:<https://doi.org/10.1016/j.commatsci.2012.10.028>
- [28] A. Y.-T. Wang, R. J. Murdock, S. K. Kauwe, A. O. Oliynyk, A. Gurlo, J. Bragoch, K. A. Persson, and T. Sparks. Machine Learning for Materials Scientists: An Introductory Guide toward Best Practices. *Chem. Mater.* (2020). doi:[10.1021/acs.chemmater.0c01907](https://doi.org/10.1021/acs.chemmater.0c01907)

- [29] E. C. Schueller, J. L. Zuo, J. D. Bocarsly, D. A. Kitchaev, S. D. Wilson, and R. Seshadri. Modeling the Structural Distortion and Magnetic Ground State of the Polar Lacunar Spinel GaV_4Se_8 . *Phys. Rev. B* **100** (2019) 045131. doi:[10.1103/PhysRevB.100.045131](https://doi.org/10.1103/PhysRevB.100.045131)
- [30] E. Ruff, A. Butykai, K. Geirhos, S. Widmann, V. Tsurkan, E. Stefanet, I. Kezsmarki, A. Loidl, and P. Lunkenheimer. Polar and Magnetic Order in GaV_4Se_8 . *Phys. Rev. B* **96** (2017) 165119. doi:[10.1103/PhysRevB.96.165119](https://doi.org/10.1103/PhysRevB.96.165119)
- [31] D. Bichler. *Magnetismus und strukturelle Phasenumwandlungen von Verbindungen mit tetraedrischen Metallclustern*. Ph.D. thesis, Ludwig-Maximilians-Universität München (2010).
- [32] D. Bichler and D. Johrendt. Interplay of Magnetism and Bonding in $\text{GaV}_{4-x}\text{Cr}_x\text{Se}_8$. *Chem. Mater.* **23** (2011) 3014–3019. doi:[10.1021/cm200776v](https://doi.org/10.1021/cm200776v)
- [33] Y. Sahoo and A. K. Rastogi. Evidence of Hopping Conduction in the V_4 -Cluster Compound GaV_4S_8 . *J. Phys.: Condens. Matter* **5** (1993) 5953–5962. doi:[10.1088/0953-8984/5/32/023](https://doi.org/10.1088/0953-8984/5/32/023)
- [34] A. Camjayi, C. Acha, R. Weht, M. G. Rodríguez, B. Corraze, E. Janod, L. Cario, and M. J. Rozenberg. First-Order Insulator-to-Metal Mott Transition in the Paramagnetic 3D System GaTa_4Se_8 . *Phys. Rev. Lett.* **113** (2014) 086404. doi:[10.1103/PhysRevLett.113.086404](https://doi.org/10.1103/PhysRevLett.113.086404)
- [35] R. Pocha, D. Johrendt, and R. Pottgen. Electronic and Structural Instabilities in GaV_4S_8 and GaMo_4S_8 . *Chem. Mater.* **12** (2000) 2882–2887. doi:[10.1021/cm001099b](https://doi.org/10.1021/cm001099b)
- [36] A. I. Liechtenstein, V. I. Anisimov, and J. Zaanen. Density-Functional Theory and Strong Interactions: Orbital Ordering in Mott-Hubbard Insulators. *Phys. Rev. B* **52** (1995) R5467–R5470. doi:[10.1103/PhysRevB.52.R5467](https://doi.org/10.1103/PhysRevB.52.R5467)
- [37] S. L. Dudarev, G. A. Botton, S. Y. Savrasov, C. J. Humphreys, and A. P. Sutton. Electron-Energy-Loss Spectra and the Structural Stability of Nickel Oxide: An LSDA+U Study. *Phys. Rev. B* **57** (1998) 1505–1509. doi:[10.1103/PhysRevB.57.1505](https://doi.org/10.1103/PhysRevB.57.1505)
- [38] J. Harl and G. Kresse. Accurate Bulk Properties from Approximate Many-Body Techniques. *Phys. Rev. Lett.* **103** (2009) 056401. doi:[10.1103/PhysRevLett.103.056401](https://doi.org/10.1103/PhysRevLett.103.056401)
- [39] H. Peng and S. Lany. Polymorphic Energy Ordering of MgO , ZnO , GaN , and MnO Within the Random Phase Approximation. *Phys. Rev. B* **87** (2013) 174113. doi:[10.1103/PhysRevB.87.174113](https://doi.org/10.1103/PhysRevB.87.174113)

- [40] L. Schimka, R. Gaudoin, J. Klimes, M. Marsman, and G. Kresse. Lattice Constants and Cohesive Energies of Alkali, Alkaline-Earth, and Transition Metals: Random Phase Approximation and Density Functional Theory Results. *Phys. Rev. B* **87** (2013) 214102. doi:[10.1103/PhysRevB.87.214102](https://doi.org/10.1103/PhysRevB.87.214102)
- [41] V. Petricek, M. Dusek, and L. Palatinus. Crystallographic Computing System JANA2006: General Features. *Z. Kristallogr. Cryst. Mater.* **229** (2014) 345–352. doi:[10.1515/zkri-2014-1737](https://doi.org/10.1515/zkri-2014-1737)
- [42] K. Momma and F. Izumi. VESTA3 for Three-Dimensional Visualization of Crystal, Volumetric and Morphology Data. *J. Appl. Crystallogr.* **44** (2011) 1272–1276. doi:[10.1107/S0021889811038970](https://doi.org/10.1107/S0021889811038970)
- [43] G. Kresse and J. Furthmüller. Efficient Iterative Schemes for Ab Initio Total-Energy Calculations Using a Plane-Wave Basis Set. *Phys. Rev. B* **54** (1996) 11169–11186. doi:[10.1103/PhysRevB.54.11169](https://doi.org/10.1103/PhysRevB.54.11169)
- [44] P. E. Blochl. Projector Augmented-Wave Method. *Phys. Rev. B* **50** (1994) 17953–17979. doi:[10.1103/PhysRevB.50.17953](https://doi.org/10.1103/PhysRevB.50.17953)
- [45] G. Kresse and D. Joubert. From Ultrasoft Pseudopotentials to the Projector Augmented-Wave Method. *Phys. Rev. B* **59** (1999) 1758–1775. doi:[10.1103/PhysRevB.59.1758](https://doi.org/10.1103/PhysRevB.59.1758)
- [46] J. P. Perdew, K. Burke, and M. Ernzerhof. Generalized Gradient Approximation Made Simple. *Phys. Rev. Lett.* **77** (1996) 3865–3868. doi:[10.1103/PhysRevLett.77.3865](https://doi.org/10.1103/PhysRevLett.77.3865)
- [47] B. J. Campbell, H. T. Stokes, D. E. Tanner, and D. M. Hatch. ISODISPLACE: a web-based tool for exploring structural distortions. *J. Appl. Cryst.* **39** (2006) 607–614. doi:[10.1107/S0021889806014075](https://doi.org/10.1107/S0021889806014075)
- [48] A. M. Ganose, A. J. Jackson, and D. O. Scanlon. sumo: Command-Line Tools for Plotting and Analysis of Periodic *ab initio* Calculations. *J. Open Source Softw.* **3** (2018) 717. doi:<https://doi.org/10.21105/joss.00717>
- [49] T. Proffen, R. G. DiFrancesco, S. J. L. Billinge, E. L. Brosha, and H. G. Kwei. Measurement of the Local Jahn-Teller Distortion in $\text{LaMnO}_{3.006}$. *Phys. Rev. B* **60** (1999) 9973–9977. doi:[10.1103/PhysRevB.60.9973](https://doi.org/10.1103/PhysRevB.60.9973)
- [50] D. P. Shoemaker, J. Li, and R. Seshadri. Unraveling Atomic Positions in an Oxide Spinel with Two Jahn–Teller Ions: Local Structure Investigation of CuMn_2O_4 . *J. Am. Chem. Soc.* **131** (2009) 11450–11457. doi:[10.1021/ja902096h](https://doi.org/10.1021/ja902096h)
- [51] S. V. Streltsov and D. I. Khomskii. Covalent Bonds Against Magnetism in Transition Metal Compounds. *Proc. Natl. Acad. Sci.* **113** (2016) 10491–10496. doi:[10.1073/pnas.1606367113](https://doi.org/10.1073/pnas.1606367113)

- [52] E. C. Schueller, D. A. Kitchaev, J. L. Zuo, J. D. Bocarsly, J. A. Cooley, A. V. der Ven, S. D. Wilson, and R. Seshadri. Structural Evolution and Skyrmionic Phase Diagram of the Lacunar Spinel GaMo_4Se_8 . *Phys. Rev. Materials* **4** (2020) 064402. doi:[10.1103/PhysRevMaterials.4.064402](https://doi.org/10.1103/PhysRevMaterials.4.064402)
- [53] I. I. Mazin, H. O. Jeschke, K. Foyevtsova, R. Valenti, and D. I. Khomskii. Na_2IrO_3 as a Molecular Orbital Crystal. *Phys. Rev. Lett.* **109** (2012) 197201. doi:[10.1103/PhysRevLett.109.197201](https://doi.org/10.1103/PhysRevLett.109.197201)
- [54] H.-S. Kim, J. Im, M. J. Han, and H. Jin. Spin-Orbital Entangled Molecular j_{eff} States in Lacunar Spinel Compounds. *Nat. Commun.* **5** (2014) 3988. doi:[10.1038/ncomms4988](https://doi.org/10.1038/ncomms4988)
- [55] M. Francois, O. V. Alexandrov, K. Yvon, H. B. Yaich-Aerrache, P. Gougeon, M. Potel, and M. Sergent. Structural Phase Transition in GaMo_4Se_8 and AlMo_4S_8 by X-ray Powder Diffraction. *Z. Kristallogr. Cryst. Mater.* **200** (1992) 47–55. doi:[10.1524/zkri.1992.200.1-2.47](https://doi.org/10.1524/zkri.1992.200.1-2.47)
- [56] M. Francois, W. Lengauer, and K. Yvon. Structural Phase Transition in GaMo_4S_8 by X-ray Powder Diffraction. *Z. Kristallogr. Cryst. Mater.* **196** (1990) 111–128. doi:[10.1524/zkri.1991.196.14.111](https://doi.org/10.1524/zkri.1991.196.14.111)
- [57] A. K. Rastogi, A. Berton, J. Chaussy, R. Tournier, M. Potel, R. Chevrel, and M. Sergent. Itinerant Electron Magnetism in the Mo_4 Tetrahedral Cluster Compounds GaMo_4S_8 , GaMo_4Se_8 , and $\text{GaMo}_4\text{Se}_4\text{Te}_4$. *J. Low Temp. Phys.* **52** (1983) 539–577. doi:[10.1007/BF00682130](https://doi.org/10.1007/BF00682130)
- [58] A. K. Rastogi and E. P. Wohlfarth. Magnetic Field-Induced Transitions in the Mo_4 Cluster Compounds GaMo_4S_8 and GaMo_4Se_8 Showing Heavy Fermion Behaviour. *Phys. Stat. Sol. (b)* **142** (1987) 569–573. doi:[10.1002/pssb.2221420226](https://doi.org/10.1002/pssb.2221420226)
- [59] D. A. Kitchaev, E. C. Schueller, and A. Van der Ven. Mapping Skyrmion Stability in Uniaxial Lacunar Spinel Magnets from First-Principles. *Phys. Rev. B* **101** (2020) 054409. doi:[10.1103/PhysRevB.101.054409](https://doi.org/10.1103/PhysRevB.101.054409)
- [60] M. Y. Jeong, S. H. Chang, B. H. Kim, J.-H. Sim, A. Said, D. Casa, T. Gog, E. Janod, L. Cario, S. Yunoki, M. J. Han, and J. Kim. Direct Experimental Observation of the Molecular $J_{eff} = 3/2$ Ground State in the Lacunar Spinel GaTa_4Se_8 . *Nat. Commun.* **8** (2017) 782. doi:[10.1038/s41467-017-00841-9](https://doi.org/10.1038/s41467-017-00841-9)
- [61] A. Butykai, D. Szaller, L. F. Kiss, L. Balogh, M. Garst, L. DeBeer-Schmitt, T. Waki, Y. Tabata, H. Nakamura, I. Kezsmarki, and S. Bordacs. Squeezing Magnetic Modulations by Enhanced Spin-Orbit Coupling of $4d$ Electrons in the Polar Semiconductor GaMo_4S_8 . *arXiv* (2019). doi:[1910.11523](https://doi.org/10.1101/11523)

- [62] R. Drautz and M. Fähnle. Spin-Cluster Expansion: Parametrization of the General Adiabatic Magnetic Energy Surface with ab initio Accuracy. *Phys. Rev. B* **69** (2004) 104404. doi:[10.1103/PhysRevB.69.104404](https://doi.org/10.1103/PhysRevB.69.104404)
- [63] J. C. Thomas and A. Van der Ven. The Exploration of Nonlinear Elasticity and its Efficient Parameterization for Crystalline Materials. *J. Mech. Phys. Solids* **107** (2017) 76–95. doi:[10.1016/j.jmps.2017.06.009](https://doi.org/10.1016/j.jmps.2017.06.009)
- [64] A. Van der Ven, J. C. Thomas, B. Puchala, and A. R. Natarajan. First-Principles Statistical Mechanics of Multicomponent Crystals. *Annu. Rev. Mater. Res.* **48** (2018) 27–55. doi:[10.1146/annurev-matsci-070317-124443](https://doi.org/10.1146/annurev-matsci-070317-124443)
- [65] *Appendix B contains AC and dM/dT magnetic data, as well as details of the magnetic cluster expansion and magnetic Hamiltonians used in this work. .*
- [66] A. Van de Walle and G. Ceder. Automating First-Principles Phase Diagram Calculations. *J. Phase Equilib.* **23** (2002) 348. doi:[10.1361/105497102770331596](https://doi.org/10.1361/105497102770331596)
- [67] S. Jakob. *Strukturen, Magnetismus und Phasenumwandlungen der Mott-Isolatoren $Ga(M_{4-x}M'_x)Q_8$ und $(M_{4-x}M'_x)Q_4I_4$ ($M, M' = Mo, Nb, Ta; Q = S, Se; x = 0-4$)*. Ph.D. thesis, Ludwig-Maximilians-Universität München (2010).
- [68] A. A. Coelho. TOPAS and TOPAS-Academic: An Optimization Program Integrating Computer Algebra and Crystallographic Objects Written in C++. *J. Appl. Crystallogr.* **51** (2018) 210–218. doi:[10.1107/S1600576718000183](https://doi.org/10.1107/S1600576718000183)
- [69] S. R. Kline. Reduction and Analysis of SANS and USANS Data Using IGOR Pro. *J. Appl. Cryst.* **39** (2006) 895–900. doi:[10.1107/S0021889806035059](https://doi.org/10.1107/S0021889806035059)
- [70] M. C. Kemei, P. T. Barton, S. L. Moffitt, M. W. Gaultois, J. A. Kurzman, R. Seshadri, M. R. Suchomel, and Y.-I. Kim. Crystal Structures of Spin-Jahn-Teller-Ordered $MgCr_2O_4$ and $ZnCr_2O_4$. *J. Phys.: Condens. Matter* **25** (2013) 326001. doi:[10.1088/0953-8984/25/32/326001](https://doi.org/10.1088/0953-8984/25/32/326001)
- [71] J. D. Bocarsly, C. Heikes, C. M. Brown, S. D. Wilson, and R. Seshadri. Deciphering Structural and Magnetic Disorder in the Chiral Skyrmion Host Materials $Co_xZn_yMn_z$ ($x + y + z = 20$). *Phys. Rev. Materials* **3** (2019) 014402. doi:[10.1103/PhysRevMaterials.3.014402](https://doi.org/10.1103/PhysRevMaterials.3.014402)
- [72] L. Kautzsch, J. D. Bocarsly, C. Felser, S. D. Wilson, and R. Seshadri. Controlling Dzyaloshinskii-Moriya Interactions in the Skyrmion Host Candidates $FePd_{1-x}Pt_xMo_3N$. *Phys. Rev. Materials* **4** (2020) 024412. doi:[10.1103/PhysRevMaterials.4.024412](https://doi.org/10.1103/PhysRevMaterials.4.024412)

- [73] R. Takagi, D. Morikawa, K. Karube, N. Kanazawa, K. Shibata, G. Tatara, Y. Tokunaga, T. Arima, Y. Taguchi, Y. Tokura, and S. Seki. Spin-Wave Spectroscopy of the Dzyaloshinskii-Moriya Interaction in Room-Temperature Chiral Magnets Hosting Skyrmions. *Phys. Rev. B* **95** (2017) 220406(R). doi:[10.1103/PhysRevB.95.220406](https://doi.org/10.1103/PhysRevB.95.220406)
- [74] C. Abert. Micromagnetics and Spintronics: Models and Numerical Methods. *Eur. Phys. J. B* **92** (2019) 120. doi:[10.1140/epjb/e2019-90599-6](https://doi.org/10.1140/epjb/e2019-90599-6)
- [75] D. Bichler, V. Zinth, D. Johrendt, O. Heyer, M. K. Forthaus, T. Lorenz, and M. M. Abd-Elmeguid. Structural and Magnetic Phase Transitions of the V_4 -cluster compound GeV_4S_8 . *Phys. Rev. B* **77** (2008) 212102. doi:[10.1103/PhysRevB.77.212102](https://doi.org/10.1103/PhysRevB.77.212102)
- [76] A. Bogdanov and A. Hubert. Thermodynamically Stable Magnetic Vortex States in Magnetic Crystals. *J. Magn. Magn. Mater.* **138** (1994) 255–269. doi:[10.1016/0304-8853\(94\)90046-9](https://doi.org/10.1016/0304-8853(94)90046-9)
- [77] U. Güngördü, R. Nepal, O. A. Tretiakov, K. Belashchenko, and A. A. Kovalev. Stability of Skyrmion Lattices and Symmetries of Quasi-Two-Dimensional Chiral Magnets. *Phys. Rev. B* **93** (2016) 064428. doi:[10.1103/PhysRevB.93.064428](https://doi.org/10.1103/PhysRevB.93.064428)
- [78] J. Rowland, S. Banerjee, and M. Randeria. Skyrmions in Chiral Magnets with Rashba and Dresselhaus Spin-Orbit Coupling. *Phys. Rev. B* **93** (2016) 020404(R). doi:[10.1103/PhysRevB.93.020404](https://doi.org/10.1103/PhysRevB.93.020404)
- [79] J. Takeda, Y. Kobayashi, K. Kodama, H. Harashina, and M. Sato. Transport, Magnetic and Thermal Properties of $BaCo_{1-x}Ni_xS_2$. *J. Phys. Soc. Jpn.* **64** (1995) 2550–2557. doi:[10.1143/JPSJ.64.2550](https://doi.org/10.1143/JPSJ.64.2550)
- [80] M. Sato, H. Sasaki, H. Harashina, Y. Yasui, J. Takeda, K. Kodama, S. Shamoto, K. Kakurai, and M. Nishi. Metal–Insulator Transition of $BaCo_{1-x}Ni_xS_2$ Induced by Pressure and Carrier Number Control. *Rev. High Pressure Sci. Technol.* **7** (1998) 447–452. doi:[10.4131/jshpreview.7.447](https://doi.org/10.4131/jshpreview.7.447)
- [81] L. S. Martinson, J. W. Schweitzer, and N. C. Baenziger. Properties of the Layered $BaCo_{1-x}Ni_xS_2$ Alloy System. *Phys. Rev. B* **54** (1996) 11265. doi:[10.1103/PhysRevB.54.11265](https://doi.org/10.1103/PhysRevB.54.11265)
- [82] D. Mandrus, J. L. Sarrao, B. C. Chakoumakos, J. A. Fernandez-Baca, S. E. Nagler, and B. C. Sales. Magnetism in $BaCoS_2$. *J. Appl. Phys.* **81** (1997) 4620–4622. doi:[10.1063/1.365182](https://doi.org/10.1063/1.365182)
- [83] K. Takenaka, S. Kashima, A. Osuka, S. Sugai, Y. Yasui, S. Shamoto, and M. Sato. Anisotropic Optical Spectra of $BaCo_{1-x}Ni_xS_2$: Effect of Ni Substitution on the

- Electronic Structure of the $\text{Co}_{1-x}\text{Ni}_x\text{S}$ Plane. *Phys. Rev. B* **63** (2001) 115113. doi:[10.1103/PhysRevB.63.115113](https://doi.org/10.1103/PhysRevB.63.115113)
- [84] J. B. Goodenough. Direct Cation–Cation Interactions in Several Oxides. *Phys. Rev.* **117** (1960) 1442–1451. doi:[10.1103/PhysRev.117.1442](https://doi.org/10.1103/PhysRev.117.1442)
- [85] S. A. Corr, D. P. Shoemaker, B. C. Melot, and R. Seshadri. Real-Space Investigation of Structural Changes at the Metal-Insulator Transition in VO_2 . *Phys. Rev. Lett.* **105** (2010) 056404. doi:[10.1103/PhysRevLett.105.056404](https://doi.org/10.1103/PhysRevLett.105.056404)
- [86] Z. Guguchia, B. A. Frandsen, D. Santos-Cottin, S. C. Cheung, Z. Gong, Q. Sheng, K. Yamakawa, A. M. Hallas, M. N. Wilson, Y. Cai, J. Beare, R. Khasanov, R. D. Renzi, G. M. Luke, S. Shamoto, A. Gauzzi, Y. Klein, and Y. J. Uemura. Probing the Quantum Phase Transition in Mott Insulator BaCoS_2 Tuned by Pressure and Ni Substitution. *Phys. Rev. Materials* **3** (2019) 045001. doi:[10.1103/PhysRevMaterials.3.045001](https://doi.org/10.1103/PhysRevMaterials.3.045001)
- [87] T. Sato, H. Kumigashira, D. Ionel, T. Takahashi, I. Hase, H. Ding, J. C. Camuzano, and S. Shamoto. Evolution of Metallic States from the Hubbard Band in the Two-Dimensional Mott System $\text{BaCo}_{1-x}\text{Ni}_x\text{S}_2$. *Phys. Rev. B* **64** (2001) 075103. doi:[10.1103/PhysRevB.64.075103](https://doi.org/10.1103/PhysRevB.64.075103)
- [88] N. C. Baenziger, L. Grout, L. S. Martinson, and J. W. Schweitzer. BaCoS_2 . *Acta Cryst. C* **50** (1994) 1375–1377. doi:[10.1107/S0108270194003707](https://doi.org/10.1107/S0108270194003707)
- [89] J. P. Perdew, A. Ruzsinszky, G. I. Csonka, O. A. Vydrov, G. E. Scuseria, L. A. Constantin, X. Zhou, and K. Burke. Restoring the Density-Gradient Expansion for Exchange in Solids and Surfaces. *Phys. Rev. Lett.* **100** (2008) 136406. doi:[10.1103/PhysRevLett.100.136406](https://doi.org/10.1103/PhysRevLett.100.136406)
- [90] V. M. Zainullina and M. A. Korotin. Ground state of BaCoS_2 as a Set of Energy-Degenerate Orbital-Ordered Configurations of Co^{2+} Ions. *Phys. Solid State* **53** (2011) 978–984. doi:[10.1134/S1063783411050325](https://doi.org/10.1134/S1063783411050325)
- [91] A. Togo and I. Tanaka. First Principles Phonon Calculations in Materials Science. *Scr. Mater.* **108** (2015) 1–5. doi:[10.1016/j.scriptamat.2015.07.021](https://doi.org/10.1016/j.scriptamat.2015.07.021)
- [92] A. P. Hammersley, S. O. Svensson, M. Hanfland, A. N. Fitch, and D. Hausermann. Two-Dimensional Detector Software: From Real Detector to Idealised Image or Two-theta Scan. *High Pressure Res.* **14** (1996) 235–248. doi:[10.1080/08957959608201408](https://doi.org/10.1080/08957959608201408)
- [93] X. Qiu, J. W. Thompson, and S. J. L. Billinge. *PDFgetX2*: a GUI-driven Program to Obtain the Pair Distribution Function from X-ray Powder Diffraction Data. *J. Appl. Cryst.* **37** (2004) 678. doi:[10.1107/S0021889804011744](https://doi.org/10.1107/S0021889804011744)

- [94] C. L. Farrow, P. Juhas, J. W. Liu, D. Bryndin, E. S. B. zin, J. Bloch, T. Proffen, and S. J. L. Billinge. PDFfit2 and PDFgui: Computer Programs for Studying Nanostructure in Crystals. *J. Phys.: Condens. Matter* **19** (2007) 335219. doi:[10.1088/0953-8984/19/33/335219](https://doi.org/10.1088/0953-8984/19/33/335219)
- [95] M. G. Tucker, D. A. Keen, M. T. Dove, A. L. Goodwin, and Q. Hui. RMCProfile: Reverse Monte Carlo for Polycrystalline Materials. *J. Phys.: Condens. Matter* **19** (2007) 335218. doi:[10.1088/0953-8984/19/33/335218](https://doi.org/10.1088/0953-8984/19/33/335218)
- [96] T. Jurca, A. Farghal, P.-H. Lin, I. Korobkov, M. Murugesu, and D. S. Richeson. Single-Molecule Magnet Behavior with a Single Metal Center Enhanced through Peripheral Ligand Modifications. *J. Am. Chem. Soc.* **133** (2011) 15814–15817. doi:[10.1021/ja204562m](https://doi.org/10.1021/ja204562m)
- [97] A. M. Tehrani, A. O. Oliynyk, M. Parry, Z. Rizvi, S. Couper, F. Lin, L. Miyagi, T. D. Sparks, and J. Brgoch. Machine Learning Directed Search for Ultraincompressible, Superhard Materials. *J. Am. Chem. Soc.* **140** (2018) 9844–9853. doi:[10.1021/jacs.8b02717](https://doi.org/10.1021/jacs.8b02717)
- [98] J. Lee, A. Seko, K. Shitara, K. Nakayama, and I. Tanaka. Prediction Model of Band Gap for Inorganic Compounds by Combination of Density Functional Theory Calculations and Machine Learning Techniques. *Phys. Rev. B* **93** (2016) 115104. doi:[10.1103/PhysRevB.93.115104](https://doi.org/10.1103/PhysRevB.93.115104)
- [99] R. Woods-Robinson, D. Broberg, A. Faghaninia, A. Jain, S. S. Dwaraknath, and K. A. Persson. Assessing High-Throughput Descriptors for Prediction of Transparent Conductors. *Chem. Mater.* **30** (2018) 8375–8389. doi:[10.1021/acs.chemmater.8b03529](https://doi.org/10.1021/acs.chemmater.8b03529)
- [100] W. Kunnmann, S. L. Placa, L. M. Corliss, J. M. Hastings, and E. Banks. Magnetic Structures of the Ordered Trirutiles Cr_2WO_6 , Cr_2TeO_6 and Fe_2TeO_6 . *J. Phys. Chem. Solids* **29** (1968) 1359–1364. doi:[10.1016/0022-3697\(68\)90187-X](https://doi.org/10.1016/0022-3697(68)90187-X)
- [101] J. M. Law, H.-J. Koo, M.-H. Whangbo, E. Brücher, V. Pomjakushin, and R. K. Kremer. Strongly Correlated One-Dimensional Magnetic Behavior of NiTa_2O_6 . *Phys. Rev. B* **89** (2014) 014423. doi:[10.1103/PhysRevB.89.014423](https://doi.org/10.1103/PhysRevB.89.014423)
- [102] M. Kato, A. Hatazaki, K. Yoshimura, and K. Kosuge. One-Dimensional Magnetic Behavior of CuSb_2O_6 . *Physica B Condens. Matter* **281–282** (2000) 663–664. doi:[10.1016/S0921-4526\(99\)00944-8](https://doi.org/10.1016/S0921-4526(99)00944-8)
- [103] H. Ehrenberg, G. Wltschek, J. Rodriguez-Carvajal, and T. Vogt. Magnetic Structures of the Tri-Rutiles NiTa_2O_6 and NiSb_2O_6 . *J. Magn. Magn. Mater.* **184** (1998) 111–115. doi:[10.1016/S0304-8853\(97\)01122-0](https://doi.org/10.1016/S0304-8853(97)01122-0)

- [104] D. Kasinathan, K. Koepf, and H. Rosner. Quasi-One-Dimensional Magnetism Driven by Unusual Orbital Ordering in CuSb_2O_6 . *Phys. Rev. Lett.* **100** (2008) 237202. doi:[10.1103/PhysRevLett.100.237202](https://doi.org/10.1103/PhysRevLett.100.237202)
- [105] F. H. Allen, G. Bergerhoff, and I. D. Brown. *Crystallographic Databases*. International Union of Crystallography (1987).
- [106] A. Dunn, Q. Wang, A. Ganose, D. Dopp, and A. Jain. Benchmarking Materials Property Prediction Methods: The Matbench Test Set and Automaterminer Reference Algorithm. *arXiv* (2020). doi:[arXiv:2005.00707](https://doi.org/10.26434/chemrxiv-2020-00707)
- [107] T. T. Le, W. Fu, and J. H. Moore. Scaling Tree-Based Automated Machine Learning to Biomedical Big Data with a Feature Set Selector. *J. Bioinform.* **36** (2020) 250–256. doi:[10.1007/978-3-319-31204-0_9](https://doi.org/10.1007/978-3-319-31204-0_9)
- [108] S. Esmailzadeh and J. Grins. Meta-stable Phases in the Mn–Ta–O System. *Solid State Sci.* **4** (2002) 117–123. doi:[10.1016/S1293-2558\(01\)01216-X](https://doi.org/10.1016/S1293-2558(01)01216-X)
- [109] F. Sala and F. Trifiró. Relationship Between Structure and Activity of Antimony Mixed Oxides in 1-Butene Oxidation. *J. Catal.* **41** (1976) 1–13. doi:[10.1016/0021-9517\(76\)90194-9](https://doi.org/10.1016/0021-9517(76)90194-9)
- [110] M. Saes, N. P. Raju, and J. E. Greedan. Structure and Magnetism in CrTa_2O_6 : A Trirutile Oxide Based on Cr^{2+} . *J. Solid State Chem.* **140** (1998) 7–13. doi:[10.1006/jssc.1998.7674](https://doi.org/10.1006/jssc.1998.7674)
- [111] H. Ishikawa, T. Yajima, A. Matsuo, Y. Ihara, and K. Kindo. Nonmagnetic Ground States and a Possible Quadrupolar Phase in $4d$ and $5d$ Lacunar Spinel Selenides GaM_4Se_8 ($M = \text{Nb}, \text{Ta}$). *Phys. Rev. Lett.* **124** (2020) 227202. doi:[10.1103/PhysRevLett.124.227202](https://doi.org/10.1103/PhysRevLett.124.227202)
- [112] E. C. Schueller, G. Laurita, D. H. Fabini, C. C. Stoumpos, M. G. Kanatzidis, and R. Seshadri. Crystal Structure Evolution and Notable Thermal Expansion in Hybrid Perovskites Formamidinium Tin Iodide and Formamidinium Lead Bromide. *Inorg. Chem.* **57** (2017) 695–701. doi:[10.1021/acs.inorgchem.7b02576](https://doi.org/10.1021/acs.inorgchem.7b02576)
- [113] A. Kojima, K. Teshima, Y. Shirai, and T. Miyasaka. Organometal Halide Perovskites as Visible-Light Sensitizers for Photovoltaic Cells. *J. Am. Chem. Soc.* **131** (2009) 6050–6051. doi:[10.1021/ja809598r](https://doi.org/10.1021/ja809598r)
- [114] F. Deschler, M. Price, S. Pathak, L. E. Klintberg, D.-D. Jarausch, R. Hügler, S. Hüttnert, T. Leijtens, S. D. Stranks, H. J. Snaith, M. Atatürk, R. T. Phillips, and R. H. Friend. High Photoluminescence Efficiency and Optically Pumped Lasing in Solution-Processed Mixed Halide Perovskite Semiconductors. *J. Phys. Chem. Lett.* **5** (2014) 1421–1426. doi:[10.1021/jz5005285](https://doi.org/10.1021/jz5005285)

- [115] Z.-K. Tan, R. S. Moghaddam, M. L. Lai, P. Docampo, R. Higler, F. Deschler, M. Price, A. Sadhanala, L. M. Pazos, D. Credgington, F. Hanusch, T. Bein, H. J. Snaith, and R. H. Friend. Bright Light-Emitting Diodes Based on Organometal Halide Perovskite. *Nat. Nanotechnol.* **9** (2014) 687–692. doi:[10.1038/nnano.2014.149](https://doi.org/10.1038/nnano.2014.149)
- [116] M. Saliba, T. Matsui, J.-Y. Seo, K. Domanski, J.-P. Correa-Baena, M. K. Nazeeruddin, S. M. Zakeeruddin, W. Tress, A. Abate, A. Hagfeldt, and M. Grätzel. Cesium-Containing Triple Cation Perovskite Solar Cells: Improved Stability, Reproducibility and High Efficiency. *Energy Environ. Sci.* **9** (2016) 1989–1997. doi:[10.1039/C5EE03874J](https://doi.org/10.1039/C5EE03874J)
- [117] D. Bi, W. Tress, M. I. Dar, P. Gao, J. Luo, C. Renevier, K. Schenk, A. Abate, F. Giordano, J.-P. C. Baena, J.-D. Decoppet, S. M. Zakeeruddin, M. K. Nazeeruddin, M. Grätzel, and A. Hagfeldt. Efficient Luminescent Solar Cells Based on Tailored Mixed-Cation Perovskites. *Sci. Adv.* **2** (2016) e1501170. doi:[10.1126/sciadv.1501170](https://doi.org/10.1126/sciadv.1501170)
- [118] C. Wehrenfennig, G. E. Eperon, M. B. Johnston, H. J. Snaith, and L. M. Herz. High Charge Carrier Mobilities and Lifetimes in Organolead Trihalide Perovskites. *Adv. Mater.* **26** (2014) 1584–1589. doi:[10.1002/adma.201305172](https://doi.org/10.1002/adma.201305172)
- [119] H. Oga, A. Saeki, Y. Ogomi, S. Hayase, and S. Seki. Improved Understanding of the Electronic and Energetic Landscapes of Perovskite Solar Cells: High Local Charge Carrier Mobility, Reduced Recombination, and Extremely Shallow Traps. *J. Am. Chem. Soc.* **136** (2014) 13818–13825. doi:[10.1021/ja506936f](https://doi.org/10.1021/ja506936f)
- [120] X. Wu, M. T. Trinh, D. Niesner, H. Zhu, Z. Norman, J. S. Owen, O. Yaffe, B. J. Kudisch, and X.-Y. Zhu. Trap States in Lead Iodide Perovskites. *J. Am. Chem. Soc.* **137** (2015) 2089–2096. doi:[10.1021/ja512833n](https://doi.org/10.1021/ja512833n)
- [121] G.-J. A. H. Wetzelaer, M. Scheepers, A. M. Sempere, C. Momblona, J. Ávila, and H. J. Bolink. Trap-Assisted Non-Radiative Recombination in Organic–Inorganic Perovskite Solar Cells. *Adv. Mater.* **27** (2015) 1837–1841. doi:[10.1002/adma.201405372](https://doi.org/10.1002/adma.201405372)
- [122] C. J. Howard and H. T. Stokes. Group-Theoretical Analysis of Octahedral Tilting in Perovskites. *Acta Crystallogr. Sect. B* **54** (1998) 782–789. doi:[10.1107/S0108768198004200](https://doi.org/10.1107/S0108768198004200)
- [123] I. Chung, J.-H. Song, J. Im, J. Androulakis, C. D. Malliakas, H. Li, A. J. Freeman, J. T. Kenney, and M. G. Kanatzidis. CsSnI₃: Semiconductor or Metal? High Electrical Conductivity and Strong Near-Infrared Photoluminescence from a Single Material. High Hole Mobility and Phase-Transitions. *J. Am. Chem. Soc.* **134** (2012) 8579–8587. doi:[10.1021/ja301539s](https://doi.org/10.1021/ja301539s)

- [124] T. Baikie, Y. Fang, J. M. Kadro, M. Schreyer, F. Wei, S. G. Mhaisalkar, M. Graetzel, and T. J. White. Synthesis and Crystal Chemistry of the Hybrid Perovskite $(\text{CH}_3\text{NH}_3)\text{PbI}_3$ for Solid-State Sensitised Solar Cell Applications. *J. Mater. Chem. A* **1** (2013) 5628–5641. doi:[10.1039/C3TA10518K](https://doi.org/10.1039/C3TA10518K)
- [125] L. Chi, I. Swainson, L. Cranswick, J.-H. Her, P. Stephens, and O. Knop. The Ordered Phase of Methylammonium Lead Chloride $\text{CH}_3\text{ND}_3\text{PbCl}_3$. *J. Solid State Chem.* **178** (2005) 1376–1385. doi:<https://doi.org/10.1016/j.jssc.2004.12.037>
- [126] D. H. Fabini, C. C. Stoumpos, G. Laurita, A. Kaltzoglou, A. G. Kontos, P. Falaras, M. G. Kanatzidis, and R. Seshadri. Reentrant Structural and Optical Properties and Large Positive Thermal Expansion in Perovskite Formamidinium Lead Iodide. *Angew. Chem. Int. Ed.* **55** (2016) 15392–15396. doi:[10.1002/anie.201609538](https://doi.org/10.1002/anie.201609538)
- [127] R. J. Worhatch, H. Kim, I. P. Swainson, A. L. Yonkeu, and S. J. L. Billinge. Study of Local Structure in Selected Organic–Inorganic Perovskites in the $Pm\bar{3}m$ Phase. *Chem. Mater.* **20** (2008) 1272–1277. doi:[10.1021/cm702668d](https://doi.org/10.1021/cm702668d)
- [128] D. H. Fabini, G. Laurita, J. S. Bechtel, C. C. Stoumpos, H. A. Evans, A. G. Kontos, Y. S. Raptis, P. Falaras, A. V. der Ven, M. G. Kanatzidis, and R. Seshadri. Dynamic Stereochemical Activity of the Sn^{2+} Lone Pair in Perovskite CsSnBr_3 . *J. Am. Chem. Soc.* **138** (2016) 11820–11832. doi:[10.1021/jacs.6b06287](https://doi.org/10.1021/jacs.6b06287)
- [129] A. N. Beecher, O. E. Semonin, J. M. Skelton, J. M. Frost, M. W. Terban, H. Zhai, A. Alatas, J. S. Owen, A. Walsh, and S. J. L. Billinge. Direct Observation of Dynamic Symmetry Breaking above Room Temperature in Methylammonium Lead Iodide Perovskite. *ACS Energy Lett.* **1** (2016) 880–887. doi:[10.1021/acseenergylett.6b00381](https://doi.org/10.1021/acseenergylett.6b00381)
- [130] X. Wu, L. Z. Tan, X. Shen, T. Hu, K. Miyata, M. T. Trinh, R. Li, R. Coffee, S. Liu, D. A. Egger, I. Makasyuk, Q. Zheng, A. Fry, J. S. Robinson, M. D. Smith, B. Guzelturk, H. I. Karunadasa, X. Wang, X. Zhu, L. Kronik, A. M. Rappe, and A. M. Lindenberg. Light-Induced Picosecond Rotational Disorder of the Inorganic Sublattice in Hybrid Perovskites. *Sci. Adv.* **3** (2017) e1602388. doi:[10.1126/sciadv.1602388](https://doi.org/10.1126/sciadv.1602388)
- [131] C. C. Stoumpos, C. D. Malliakas, and M. G. Kanatzidis. Semiconducting Tin and Lead Iodide Perovskites with Organic Cations: Phase Transitions, High Mobilities, and Near-Infrared Photoluminescent Properties. *Inorg. Chem.* **52** (2013) 9019–9038. doi:[10.1021/ic401215x](https://doi.org/10.1021/ic401215x)
- [132] A. C. Larson and R. V. Dreele. *General Structure Analysis System (GSAS)*. Los Alamos National Laboratory Report LAUR 86–748 (2004).

- [133] B. H. Toby. *EXPGUI*, a Graphical User Interface for *GSAS*. *J. Appl. Crystallogr.* **34** (2001) 210–213. doi:[10.1107/S0021889801002242](https://doi.org/10.1107/S0021889801002242)
- [134] D. Mitzi and K. Liang. Synthesis, Resistivity, and Thermal Properties of the Cubic Perovskite $\text{NH}_2\text{CH}=\text{NH}_2\text{SnI}_3$ and Related Systems. *J. Solid State Chem.* **134** (1997) 376–381. doi:<https://doi.org/10.1006/jssc.1997.7593>
- [135] Y. Dang, Y. Zhou, X. Liu, D. Ju, S. Xia, H. Xia, and X. Tao. Formation of Hybrid Perovskite Tin Iodide Single Crystals by Top-Seeded Solution Growth. *Angew. Chem. Int. Ed.* **55** (2016) 3447–3450. doi:[10.1002/anie.201511792](https://doi.org/10.1002/anie.201511792)
- [136] F. C. Hanusch, E. Wiesenmayer, E. Mankel, A. Binek, P. Angloher, C. Fraunhofer, N. Giesbrecht, J. M. Feckl, W. Jaegermann, D. Johrendt, T. Bein, and P. Docampo. Efficient Planar Heterojunction Perovskite Solar Cells Based on Formamidinium Lead Bromide. *J. Phys. Chem. Lett.* **5** (2014) 2791–2795. doi:[10.1021/jz501237m](https://doi.org/10.1021/jz501237m)
- [137] A. A. Zhumekenov, M. I. Saidaminov, M. A. Haque, E. Alarousu, S. P. Sarmah, B. Murali, I. Dursun, X.-H. Miao, A. L. Abdelhady, T. Wu, O. F. Mohammed, and O. M. Bakr. Formamidinium Lead Halide Perovskite Crystals with Unprecedented Long Carrier Dynamics and Diffusion Length. *ACS Energy Lett.* **1** (2016) 32–37. doi:[10.1021/acsenergylett.6b00002](https://doi.org/10.1021/acsenergylett.6b00002)
- [138] T. M. Koh, T. Krishnamoorthy, N. Yantara, C. Shi, W. L. Leong, P. P. Boix, A. C. Grimsdale, S. G. Mhaisalkar, and N. Mathews. Formamidinium Tin-Based Perovskite with Low E_g for Photovoltaic Applications. *J. Mater. Chem. A* **3** (2015) 14996–15000. doi:[10.1039/C5TA00190K](https://doi.org/10.1039/C5TA00190K)
- [139] S. J. Lee, S. S. Shin, Y. C. Kim, D. Kim, T. K. Ahn, J. H. Noh, J. Seo, and S. I. Seok. Fabrication of Efficient Formamidinium Tin Iodide Perovskite Solar Cells through SnF_2 –Pyrazine Complex. *J. Am. Chem. Soc.* **138** (2016) 3974–3977. doi:[10.1021/jacs.6b00142](https://doi.org/10.1021/jacs.6b00142)
- [140] A. Stroppa, D. D. Sante, P. Barone, M. Bokdam, G. Kresse, C. Franchini, M.-H. Whangbo, and S. Picozzi. Tunable Ferroelectric Polarization and its Interplay with Spin-Orbit Coupling in Tin Iodide Perovskites. *Nat. Commun.* **5** (2014) 5900. doi:[10.1038/ncomms6900](https://doi.org/10.1038/ncomms6900)
- [141] U. V. Waghmare, N. A. Spaldin, H. C. Kandpal, and R. Seshadri. First-Principles Indicators of Metallicity and Cation Off-Centricity in the IV-VI Rock-salt Chalcogenides of Divalent Ge, Sn, and Pb. *Phys. Rev. B* **67** (2003) 125111. doi:[10.1103/PhysRevB.67.125111](https://doi.org/10.1103/PhysRevB.67.125111)
- [142] E. S. Božin, C. D. Malliakas, P. Souvatzis, T. Proffen, N. A. Spaldin, M. G. Kanatzidis, and S. J. L. Billinge. Entropically Stabilized Local

- Dipole Formation in Lead Chalcogenides. *Science* **330** (2010) 1660–1663. doi:[10.1126/science.1192759](https://doi.org/10.1126/science.1192759)
- [143] K. M. O. Jensen, E. S. Božin, C. D. Malliakas, M. B. Stone, M. D. Lumsden, M. G. Kanatzidis, S. M. Shapiro, and S. J. L. Billinge. Lattice Dynamics Reveals a Local Symmetry Breaking in the Emergent Dipole Phase of PbTe. *Phys. Rev. B* **86** (2012) 085313. doi:[10.1103/PhysRevB.86.085313](https://doi.org/10.1103/PhysRevB.86.085313)
- [144] K. R. Knox, E. S. Božin, C. D. Malliakas, M. G. Kanatzidis, and S. J. L. Billinge. Local Off-Centering Symmetry Breaking in the High-Temperature Regime of SnTe. *Phys. Rev. B* **89** (2014) 014102. doi:[10.1103/PhysRevB.89.014102](https://doi.org/10.1103/PhysRevB.89.014102)
- [145] O. Yaffe, Y. Guo, L. Z. Tan, D. A. Egger, T. Hull, C. C. Stoumpos, F. Zheng, T. F. Heinz, L. Kronik, M. G. Kanatzidis, J. S. Owen, A. M. Rappe, M. A. Pimenta, and L. E. Brus. Local Polar Fluctuations in Lead Halide Perovskite Crystals. *Phys. Rev. Lett.* **118** (2017) 136001. doi:[10.1103/PhysRevLett.118.136001](https://doi.org/10.1103/PhysRevLett.118.136001)
- [146] M. D. Smith, A. Jaffe, E. R. Dohner, A. M. Lindenberg, and H. I. Karunadasa. Structural Origins of Broadband Emission from Layered Pb-Br Hybrid Perovskites. *Chem. Sci.* **8** (2017) 4497–4504. doi:[10.1039/C7SC01590A](https://doi.org/10.1039/C7SC01590A)
- [147] D. H. Fabini, T. Hogan, H. A. Evans, C. C. Stoumpos, M. G. Kanatzidis, and R. Seshadri. Dielectric and Thermodynamic Signatures of Low-Temperature Glassy Dynamics in the Hybrid Perovskites CH₃NH₃PbI₃ and HC(NH₂)₂PbI₃. *J. Phys. Chem. Lett.* **7** (2016) 376–381. doi:[10.1021/acs.jpcllett.5b02821](https://doi.org/10.1021/acs.jpcllett.5b02821)
- [148] N. Onoda-Yamamuro, T. Matsuo, and H. Suga. Dielectric Study of CH₃NH₃PbX₃ (X = Cl, Br, I). *J. Phys. Chem. Solids* **53** (1992) 935–939. doi:[https://doi.org/10.1016/0022-3697\(92\)90121-S](https://doi.org/10.1016/0022-3697(92)90121-S)